Quantitative Evaluation of the Interfaces in III/V Semiconductors with Scanning Transmission Electron Microscopy

Dissertation

zur
Erlangung des Doktorgrades
der Naturwissenschaften
(Dr. rer. nat.)

dem

Fachbereich Physik
der Philipps-Universität Marburg

vorgelegt von

Han Han

aus

Runan, China

Marburg/Lahn, 2017

Vom Fachbereich Physik der Philipps-Universität Marburg
als Dissertation angenommen am: 24.10.2017
Erstgutachter: Prof. Dr. Kerstin Volz
Zweitgutachter: Prof. Dr. Martin Koch
Tag der mündlichen Prüfung: 29.11.2017
Hochschulkennziffer 1180

Contents

1 Introduction 1

2 Physical Background 5
- 2.1 Crystal . . . 5
  - 2.1.1 Crystal structure . . . 5
  - 2.1.2 Reciprocal space . . . 7
  - 2.1.3 Laue condition and Bragg interpretation . . . 8
- 2.2 Basic theories about scanning transmission electron microscopy . . . 9
  - 2.2.1 Electron-specimen interaction . . . 9
  - 2.2.2 Kinematical/dynamical scattering, channelling, and beam broadening 12
  - 2.2.3 Coherent and incoherent imaging . . . 14
  - 2.2.4 The resolution and lens aberrations . . . 16
- 2.3 The investigated III-V semiconductor compounds . . . 19
  - 2.3.1 (GaIn)As/GaAs . . . 21
  - 2.3.2 (GaIn)P/GaAs . . . 21

3 Experimental and Numerical Methods 23
- 3.1 Metal organic vapor phase epitaxy . . . 23
- 3.2 High resolution X-ray diffraction . . . 24
- 3.3 Atomic force microscopy . . . 26
- 3.4 (S)TEM sample preparation . . . 27
- 3.5 Scanning transmission electron microscopy . . . 30
  - 3.5.1 Principles of STEM . . . 30
  - 3.5.2 ADF imaging . . . 33
- 3.6 Contrast simulation . . . 36
  - 3.6.1 Multi slice simulation . . . 36
  - 3.6.2 Frozen phonon approach . . . 38
  - 3.6.3 Strain relaxation . . . 39

4 Simulation of the investigated materials 41
- 4.1 Determination of the configuration number for frozen phonon approach . 41
- 4.2 GaAs simulation for sample thickness determination . . . 46
- 4.3 Image background intensity . . . 47

5 Quantitative evaluation of the interface of (GaIn)As grown on GaAs 49
5.1 Quantitative evaluation of HAADF images and interfaces 49
5.1.1 HAADF image analysis 49
5.1.2 Quantitative evaluation of HAADF images (Q-method) 50
5.1.3 Thickness correction of the (S)TEM sample 53
5.1.4 Influences of other factors on Q-method 54
5.1.5 Quantitative evaluation of the interface 57
5.1.6 Quantitative evaluation of the chemical homogeneity of the QW . 60
5.2 The influences of growth parameters on the QW and the interface 62
5.2.1 Introduction to the investigated (GaIn)As/GaAs material systems 62
5.2.2 Image evaluation 62
5.2.3 Quantitative characterization of the QW and the interface 65
5.3 The influences of growth and interruption at different temperatures 71
5.3.1 Introduction to the growth conditions of (GaIn)As/GaAs 71
5.3.2 Overview of the top interface 72
5.3.3 Quantitative evaluation of the QW and the interface 74

6 Quantitative evaluation of the chemical sensitive interface of (GaIn)P grown on GaAs 81
6.1 Background intensity map subtraction (BIMS) method 81
6.1.1 Introduction to BIMS method 81
6.1.2 Backgrond intensity map subtraction method 82
6.2 Evaluation of the heterostructure interface 87
6.2.1 Investigated (GaIn)P/GaAs material systems and the growth conditions 87
6.2.2 Interface morphology under different growth conditions 88
6.3 Characterization of the microscopic island structure 95

7 Summary and Outlook 103
7.1 Summary 103
7.2 Outlook 105

8 Zusammenfassung und Ausblick 107
8.1 Zusammenfassung 107
8.2 Ausblick 109

References 111

Acknowledgement 113

1 Introduction

Nowadays semiconductors play an important role in our society from our everyday lives to the industry. The civilization of human beings is kind of based on the various applications of semiconductor devices. The more and more powerful computers and smart phones benefit greatly from the fast development of the transistors on the integrated circuits (IC) [1], [2]. The data transfer via fiber networks is also based on the widely applied laser (Light Amplification by Stimulated Emission of Radiation) devices realized by semiconductor materials with different working wavelengths. Besides, the realization of "white" light-emitting diode (LED) [3], based on semiconductors, has not only brought light to the 21^{st} century but also reduced the energy consumption. To further protect the environment, huge numbers of solar cell factories have been founded all around the world for the clean energy.

For the mentioned applications, semiconductor devices with high performances are required. To realize the aim, the design and manufacture of the device should be in a precisely controlled way. The highlight lies in the precise control of the interfaces, formed by two different semiconductor layers in a heterostructure. The interface presents different properties from these of both the bulk and surface and plays an essential role in the functionality of the device. "The interface is the device." was once said the Nobel Prize winner Herbert Kroemer [4]. The precise control of the solid-solid semiconductor interface includes the abruptness and chemical composition at the atomic scale, which determine the charge transfer and scattering properties across the interface. Then the interface can be tailored according to the need of the devices.

With growth techniques, like metal organic vapour phase epitaxy (MOVPE) and molecular beam epitaxy (MBE), the obtained interfaces in the heterostructure can be either polar or non-polar, either strained or unstrained, either abrupt or intermixed depending on the material systems and growth conditions. The interface morphology can be controlled to some degree by growth parameters, such as growth temperature, growth interruption time, introduction of an interlayer and so on. The interface properties can be indirectly measured by quantum hall effect with photoluminescence [5]–[7], secondary ion mass spectroscopy (SIMS) [8], high resolution X-ray diffraction (HR-XRD) [9] and also angle resolved X-ray photoelectron spectroscopy [10], [11]. Besides, the structural or compositional information of the nano-sized devices can be already obtained by atomic force microscopy (AFM) [12], [13], high resolution transmission electron microscopy (TEM) [14]–[16], energy dispersive X-ray spectroscopy (EDS) [17], and electron energy loss spec-

troscopy (EELS) [18], [19]. However, to better understand the interface formation process of heterogeneous structures, a technique that can directly provide the structural and compositional information at atomic scale is in desperate need.

High angle annular dark field (HAADF) in scanning TEM (STEM) provides the Z-contrast imaging [20]–[22], which means that the collected image intensity scales with the average atomic number and the specimen thickness. Compared with the phase contrast high resolution TEM, the Z-contrast image has no phase reversal and is therefore easy to interprete. With the introduction of spherical aberration C_s-correctors, STEM has promoted the resolution limit from nanometers [23] to sub-angstrom [24]–[26]. Together with STEM simulations, quantitative information like the specimen thickness, chemical composition maps of quantum wells (QW) [23], [26]–[28] and so on can be determined. It is possible to directly characterize the internal interface morphology [25], [29], deducted from chemical composition maps, and further correlate it with the growth conditions to optimize the growth parameters.

For the high resolution HAADF images, the intensities can be recognized as the intensity of the atomic column and the diffusely scattered background intensity. The latter is mainly determined by the specimen thickness and the average atomic number [30]. For material systems with chemically sensitive backgrounds, it is vital to subtract the image background intensity for a reasonable quantitative evaluation and comparison with the contrast simulation [30]–[33], especially to resolve the internal interface at atomic scale. The column ratio mapping method, taking into consideration the image background intensity, is introduced through the successful application in AlAs/GaAs material system [31], [32]. However, this quantification of the interface only works with material systems, whose chemical composition changes on only one sublattice across the interface. If the chemical composition changes on both sublattice across the interface, this method is not valid any more. Since the evaluated basic unit is a III/V dumbbell from the original image, the resolution of the result image is deteriorated compared to the original one. Therefore, a background intensity map subtraction (BIMS) method [34] is put forward in this work to overcome the drawbacks of the column ratio mapping method. BIMS can evaluate high resolution HAADF images acquired in either <110> or <010> orientations with composition changes at both group III and group V sublattices. With BIMS a corrected image with the same pixel size as the original one can be obtained and further used for the quantitative evaluation. In the case of material systems with non-chemically sensitive backgrounds, HAADF images with atomic resolution can be investigated with a quantitative evaluation method of HAADF images (Q-method) [29] without subtraction of the image background intensity in this study. Besides, the corresponding contrast simulation is also carried out to better understand the HAADF imaging and the interface morphology.

The structure of this thesis is as follows: Chapter 2 introduces the basic physical concepts of the materials under study and the used experimental techniques. The fundamen-

tal knowledge of STEM as well as the investigated material systems, like (GaIn)As/GaAs and (Ga,In)P/GaAs, is also included in chapter 2. Chapter 3 deals with the experimental methods used in this research work. It begins with the epitaxial growth of the investigated material systems and further covers characterization methods including HR-XRD, AFM, STEM. The preparation of the TEM sample and the contrast simulation of HAADF imaging are also introduced in chapter 3. The presented results in this study are composed of three chapters according to the topic. First chapter 4 exhibits the primary results of the contrast simulation. The influences of thermal diffuse scattering (TDS) on collected intensities in STEM mode are discussed, and the minimum number of phonon configurations required by frozen phonon method are studied to obtain a reliable and reasonable result. Besides, through the contrast simulation of different bulk materials the thickness determination and the image background intensity are also demonstrated. Chapter 5 presents the Q-method, which can be applied to material systems with non-chemically sensitive backgrounds. In addition, the determination of the chemical composition map as well as the criteria to characterize the interface abruptness and chemical homogeneity of QW are explained. Then this method is applied to (GaIn)As/GaAs material systems to investigate the influences of growth conditions on both the interface and QW. However, this method can not be applied in material systems with chemically sensitive backgrounds due to the influences of the image background intensity. Therefore, BIMS is introduced in chapter 6. The method is explained in detail through its applications in determining the interface structures containing the microscopic islands at the interface of (GaIn)P/GaAs material systems. In the end, chapter 7 sums up the current results and also presents a brief outlook of the future work.

The research work was financially supported by the German Research Foundation (DFG, Deutsche Forschungsgemeinschaft) in the frame work of SFB 1083.

2 Physical Background

In this chapter, the basic physical principles of the crystal and the interaction with electrons are introduced in order to understand the HAADF imaging in STEM mode. Section 2.1 covers the basic concepts of the crystal in both real and reciprocal space and the corresponding diffraction phenomena in both spaces. In section 2.2, the interactions between the electron and the specimen as well as the basic concepts of STEM are discussed. In section 2.3, the physcial properties of the investigated materials are introduced.

2.1 Crystal

2.1.1 Crystal structure

The investigated semiconductors in this study as well as metals and ceramics are usually crystalline. In perfect crystalline materials without defects, impurities or boundaries, identical atoms usually possess an identical environment to minimize the total energy, which lead to a periodic crystal structure. A perfect crystal is composed of strictly periodic arrangement of atoms or identical atom groups in three dimensions. Such an atom or atom group can be viewed as a lattice point due to their symmetry according to Bravais [35]. A Bravais lattice of points $\boldsymbol{R}$ can be defined mathetically in three dimensions by

$$\boldsymbol{R} = n_1\boldsymbol{a}_1 + n_2\boldsymbol{a}_2 + n_3\boldsymbol{a}_3 \tag{2.1}$$

where $\boldsymbol{a}_1$, $\boldsymbol{a}_2$, and $\boldsymbol{a}_3$ are three linearly independent basis vectors and the lengths of them are usually the lattice parameters. n_1, n_2 and n_3 are integers. In fact, $\boldsymbol{a}_1$, $\boldsymbol{a}_2$, and $\boldsymbol{a}_3$ can be also viewed as the translation vectors. Under a translation of an arbitrarily translation vector $\boldsymbol{T}$ (a combination of arbitrary n_1, n_2, and n_3), the lattice and structure of an infinite crystalline material are not changed. Therefore, all the lattice points in a perfect crystal can be reached from a unit or elementary cell. A unit or elementary cell [36], [37] is the smallest 'building block', by a repetitive arrangement of which the whole crystal can be generated without overlap or any voids due to the strict periodicity of the point lattice (Bravais lattice). If such a unit or elementary cell only contains only one lattice point, it is also referred to as primitive unit cell. Otherwise it is defined as a non-

primitive unit cell. The understanding and investigation of the crystal can be simplified and reduced to a unit or elementary cell.

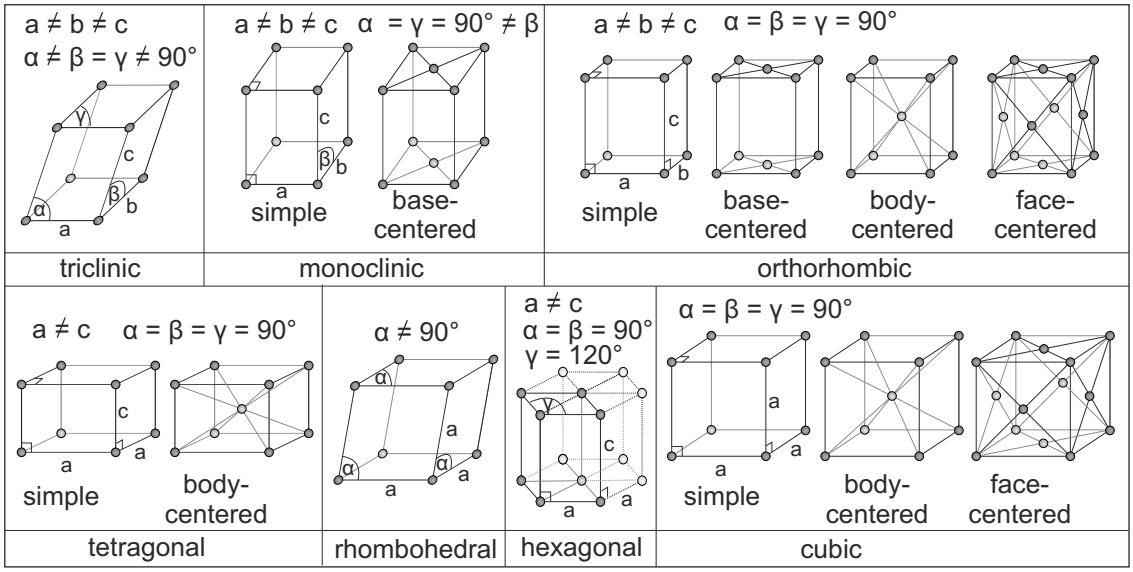

Figure 2.1: Schematic illustration of the 14 different Bravais lattice and seven crystal systems. [38]

According to the different lengths of the basis vectors and the angles between them (as shown in figure 2.1 the notation a, b, c, α, β, and γ are used to denote the vectors and angles, respectively.), there are in total seven different crystal systems. The most common and important structures are face-centered cubic (FCC), body-centered cubic (BCC) and hexagonal close-packed (HCP) structures. FCC and BCC together with the simple cubic (SC) belong to the cubic lattice systems. HCP is grouped in the hexagonal crystal system. The other five crystal systems are triclinic, monoclinic, orthorhombic, tetragonal, and rhombohedral. Bravais has proven that the several crystal systems are only composed of 14 different Bravais lattices. Considering the shape and symmetry, the crystals can be also grouped into 32 classes (point groups) and further divided into 230 space groups.

To describe the crystal, the atomic planes and directions in a crystal should be quantitatively characterized. To uniquely define the crystallographic planes and directions, the Miller indices are introduced. The Miller indices (hkl) can be obtained by multiplying the reciprocal values of the intersections of a chosen plane with the coordinate system with a proper factor so that the indices h, k and l are integers with no common divisor. Negative numbers are denoted by $\overline{h}$, $\overline{k}$, and $\overline{l}$. A detailed explanation can be found in Ref. [35]. With this method, the Miller indices of a specific crystallographic plane and direction can be written in parentheses ( ) and square brackets [ ], respectively. In a cubic system, the crystallographic direction [hkl] is normal to the crystallographic plane (hkl) [35]. Because of the symmetric arrangement of the atoms, some atomic planes and direction are iden-

tical. Such equivalent planes or directions can termed as a family of planes or directions, which are denoted by braces { } and angular brackets ⟨ ⟩.For example, a {001} plane family consists of (001), (010), (100) and all planes with the opposite sign. Also, for the hexagonal crystal structure, the Miller-Bravais indices [35] (hkil) are introduced to better describe the basal plane.

2.1.2 Reciprocal space

To determine and investigate the crystal structures mentioned in section 2.1, the diffraction techniques including X-ray, electron, and neutron diffraction are mostly used. Due to the wave-particle duality, the particles used in these techniques propogate as a wave and the wavevector $\boldsymbol{K}$ is perpendicular to the wave front. The introduction of the reciprocal space (momentum space), whose dimension is an inverse length, makes a better description of both the periodic structure and the corresponding diffraction. For a given Bravais lattice $\boldsymbol{R}$ expressed in equation 2.1, the reciprocal lattice $\boldsymbol{G}$ can be mathematically defined as

$$\boldsymbol{G} = m_1\boldsymbol{g}_1 + m_2\boldsymbol{g}_2 + m_3\boldsymbol{g}_3 \tag{2.2}$$

where m_1, m_2, and m_3 are integers. For any Bravais lattice vector $\boldsymbol{R}$ and any reciprocal lattice vector $\boldsymbol{G}$, they alwayse fulfill the following requirement

$$\boldsymbol{R} \cdot \boldsymbol{G} = 2\pi l \qquad l \in \mathbb{N} \tag{2.3}$$

In general terms, the requirement can be expressed as

$$\boldsymbol{g}_i \cdot \boldsymbol{a}_j = 2\pi\delta_{ij} \tag{2.4}$$

Here, i, j = 1, 2, 3 and Kronecker's delta (δ_{ij}) is 1 for i=j and 0 otherwise. In reciprocal space, the basis vectors of the reciprocal lattice can be mathematically determined from the basis vectors in real space as follows

$$\boldsymbol{g}_1 = 2\pi\frac{\boldsymbol{a}_2 \times \boldsymbol{a}_3}{\boldsymbol{a}_1 \cdot (\boldsymbol{a}_2 \times \boldsymbol{a}_3)}, \tag{2.5}$$

$$\boldsymbol{g}_2 = 2\pi\frac{\boldsymbol{a}_3 \times \boldsymbol{a}_1}{\boldsymbol{a}_2 \cdot (\boldsymbol{a}_3 \times \boldsymbol{a}_1)}, \tag{2.6}$$

$$\boldsymbol{g}_3 = 2\pi\frac{\boldsymbol{a}_1 \times \boldsymbol{a}_2}{\boldsymbol{a}_3 \cdot (\boldsymbol{a}_1 \times \boldsymbol{a}_2)}. \tag{2.7}$$

Here, the volume of one unit cell can be given by the scalar triple product $\boldsymbol{V}_{uc} = \boldsymbol{a}_1 \cdot (\boldsymbol{a}_2 \times \boldsymbol{a}_3)$. The reciprocal lattice is also a Bravais lattice. Every lattice point (hkl) in reciprocal space denotes a corresponding atomic plane (hkl) in real space.

2.1.3 Laue condition and Bragg interpretation

In the applied diffraction techniques, since both the source and the detector are far away from the sample, the waves can be viewed as plane waves. Therefore the wave vector $\boldsymbol{K}$ points to the wave propagation direction. For periodic structures, the diffracted beam can occur only if the difference between the incident and scattered wave vectors is equal to a reciprocal lattice vector. This is the so called Laue condition and can can be expressed by the following equation

$$\Delta \boldsymbol{k} = \boldsymbol{k}_{in} - \boldsymbol{k}_{sc} = \boldsymbol{G} \tag{2.8}$$

where $\boldsymbol{k}_{in}$ and $\boldsymbol{k}_{sc}$ are the wave vectors for incident and scattered waves, respectively. This is the foundation for all diffractions in periodic structures. To visualize the Laue condition, usually the geometrical construction of the Ewald sphere in reciprocal space is applied. The construction begins with an arbitrary selection of a reciprocal lattice point as the origin. Then the wave vector $\boldsymbol{k}_{in}$ is drawn towards the origin. An Ewald sphere with a radius $|\boldsymbol{k}_{in}|$ is constructed and centered at the starting point of $\boldsymbol{k}_{in}$. For elastic scatting ($|\boldsymbol{k}_{in}|= |\boldsymbol{k}_{sc}|$), the Laue condition as expressed in equation 2.26 is satisfied whenever the reciprocal lattice point touches the surface of the Ewald sphere. Assuming the angle between the incident and scattered wave vectors is 2θ, the wave vector $\boldsymbol{K}$ has a length of $2\pi/\lambda$. Also, in reciprocal space a lattice point indicates a set of atomic planes, so the reciprocal lattice vector $\boldsymbol{G}$ is equal to $2\pi/d_{hkl}$. Here d_{hkl} is the distance between neighboring atomic planes. So the Laue condition can also be written as follows

$$\mid \Delta \boldsymbol{k} \mid = 2\frac{2\pi}{\lambda} \cdot \sin\theta = \mid \boldsymbol{G} \mid = \frac{2\pi}{d_{hkl}} \tag{2.9}$$

This expression can be transformed into

$$2d_{hkl} \cdot \sin\theta = \lambda \tag{2.10}$$

This is exactly the expression of Bragg's Law on the first order of diffraction. For the complete expression a factor of n (n is an integer) should be added on the right side. n describes the order of the diffraction.The distance between neighboring atomic planes depends on the Miller indices {hkl} and the crystal structure expressed as follows.

$$d_{hkl} = \frac{a}{\sqrt{h^2 + k^2 + l^2}} \qquad \text{cubic structure} \tag{2.11}$$

$$d_{hkl} = \frac{a}{\sqrt{\frac{4}{3}(h^2 + k^2 + h \cdot k) + l^2(c/a)}} \qquad \text{hexagonal structure} \tag{2.12}$$

where a and c are the lattice parameters as indicated in figure 2.1. The physical meaning

behind Bragg's Law is that if the difference of the wave paths is equal to an integer multiple of the wavelength, the scattered waves will be in phase and the intensity will be in constructive interference (strengthened). Bragg's Law is a special case of the Laue condition and widely applied in X-ray diffraction technique, which will be explained in detail in section 3.2.

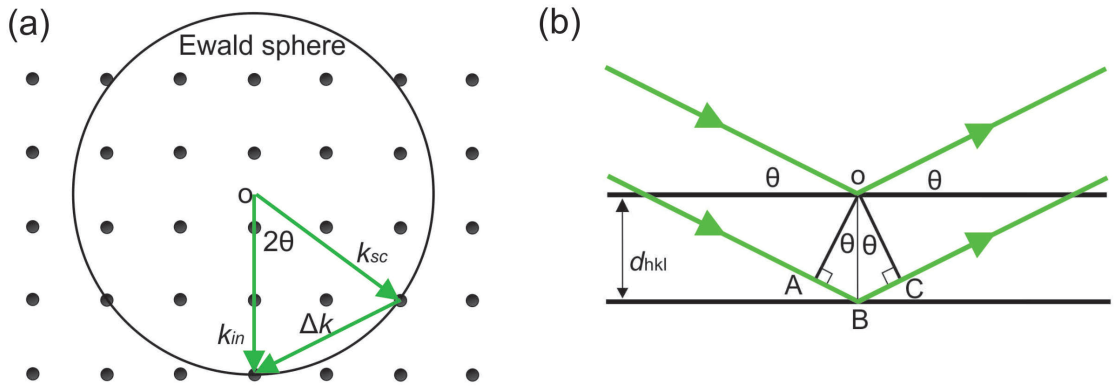

Figure 2.2: Schematic illustration of the Laue condition (a) and Bragg condition (b). (a) Ewald sphere is constructed in the reciprocal space. The dots denote the reciprocal lattice points. The labeled k_{in} and k_{sc} are the incident and scattered wave vectors. If Δk is equal to a reciprocal vector, then Laue condition is satisfied. (b) The reflected waves will be in phase, if the path difference (|AB|+|BC|) is an integer multiple of the wavelength.

2.2 Basic theories about scanning transmission electron microscopy

2.2.1 Electron-specimen interaction

The information of the TEM sample is obtained through analyzing the electron signals generated during the interaction between the electron probe and the specimen. Due to the wave-particle nature of the electrons, this interaction is treated in two different ways. The terminology elastic and inelastic scattering is used to describe if there is some energy loss during the particle collision while the terms coherent and incoherent refers to the wave nature of the electrons. For waves with the same frequency and same wavelength, if they have no phase difference or a fixed phase difference, they are referred to as the coherent waves. Otherwise they are termed as the incoherent waves. The interaction between a high-energy electron and an isolated atom is mainly caused by the coulomb repulsion from the electron cloud (low angle scattering) and the coulomb attraction from the nucleus (high angle scattering or backscattering) as shown in figure 2.3.

Usually, the electron-specimen (nucleus) interaction is regarded as similar to the Rutherford scattering. The statistical probability that a scattering event occurs can be described by the scattering cross section and the cross section of a single nucleus $\sigma_{nucleus}$ can be

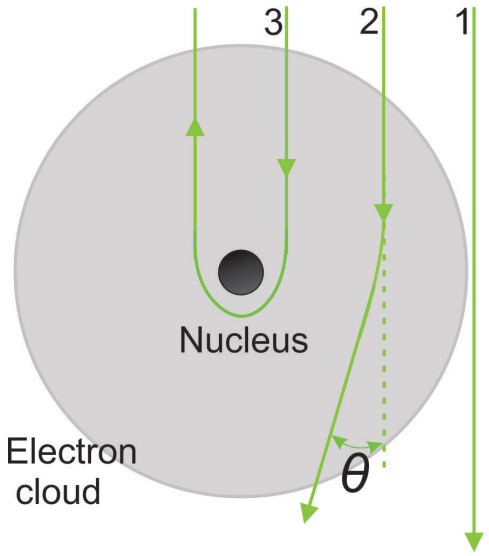

Figure 2.3: Different electron scatterings (beam path 1, 2, and 3) happened in an isolated atom. θ denotes the scattered angle, modified from [39]. Beam path 1 indicates the directly transmitted electrons without any interaction. Beam path 2 describes the low angle scattering caused by the coulomb repulsion. Beam path 3 shows the high angle scattering resulted from the coulomb attraction and the scattering angle θ can be larger than 90ř for backscattering.

expressed as

$$\sigma_{nucleus} = \pi r_n^2 \qquad \text{with} \qquad r_n = \frac{Ze}{E_0\theta} \tag{2.13}$$

where r_n is the effective radius of a nucleus, Z is the atomic number, E_0 is the accelerating voltage of the electron, e is the charge of an electron and θ is the scattering semi-angle. To describe the angular distribution of the electrons scattered from a nucleus, the differential cross section ($d\sigma/d\Omega$) is applied. In 1911 Rutherford [40] derived the differential cross section for the backscattering (high-angle) of α particles from a thin metal foil as follows

$$\sigma_{nucleus}(\theta) = \frac{e^4 Z^2}{16(4\pi\varepsilon_0 E_0)^2} \frac{d\Omega}{\sin^4 \frac{\theta}{2}} \tag{2.14}$$

ε_0 is the electric constant and Ω is the solid angle. However, Rutherford did not take the screening effect of the electron cloud into account and, therefore, underestimated the differential cross section. On the other hand, if the acceleration voltage is larger than 100 keV (This is the case for most modern TEM investigations), the relativistic effects should be considered. However, the expression (equation 2.14) has neglected the influences of relativity. After taking screening effects and relativity into account, the

modified expression of Rutherford backscattering is

$$\sigma_{nucleus}(\theta) = \frac{\lambda_R^4 Z^2}{64\pi^4 a_0^2} \frac{d\Omega}{[\sin^2(\frac{\theta}{2}) + \frac{\theta_0^2}{4}]^2} \tag{2.15}$$

θ_0 is a particular scattering angle used to describe the screening effect. If the scattering angle is larger than θ_0 (θ_0 is usually smaller than 3°), the electron-electron interaction can be ignored. λ_R is the relativistically corrected electron wavelength and a_0 is the Bohr radius (0.0529 nm). Based on equations 2.15 and 2.14, the electron wavelength (λ_R) (determined by acceleration voltage (E_0)), the atomic number of the atom (Z) and the scattering semi-angle (θ_0) can greatly affect the probability of the scattering event.

However, the Rutherford model has neglected the wave nature of the electron beam and can not be applied to get an accurate result of the nucleus cross section. Therefore, the atomic scattering factor f(θ) is put forward to include the wave nature of the electron beam. It is related to the differential cross section by

$$|f(\theta)|^2 = \frac{d\sigma_{nucleus}(\theta)}{d\Omega} \tag{2.16}$$

f(θ) is a measure of the amplitude of the wave feature of the electron beam and $|f(\theta)|^2$ describes the intensity of the scattered electron wave. Contrary to the Rutherford backscattering model, which matches the low-angle scattering (electron-electron interaction) badly, the atomic scattering factor can better describe the low-angle scattering process. $f(\theta)$ can be expressed as follows:

$$f(\theta) = \frac{(1 + \frac{E_0}{m_0 c^2})}{8\pi^2 a_0} \Big(\frac{\lambda}{\sin\frac{\theta}{2}}\Big)^2 (f_{en} - f_x) \tag{2.17}$$

where m_0 is the mass of an electron and f_x is the well known scattering factor for X-rays. The other denotions have already been explained in previous equations. On the right side of equation 2.17, the term f_{en} describes the elastic electron-nucleus scattering while the term f_x is the elastic electron-electron scattering. As shown in figure 2.4, $f(\theta)$ decreases with increasing θ and smaller atomic number Z.

The atomic scattering factor $f(\theta)$ describes the scattering ability of one single atom. Different atoms have different scattering powers. Also, the configuration of various atoms can significantly influence the final scattering. Since the material is composed of many repetitions of the unit cell in x, y, and z directions in the investigated semiconductors, they can be better described by the scattering power of one unit cell. Therefore, the atomic scattering factor $f(\theta)$ of all the atoms labelled by i in one unit cell are summed together with the correction of the phase change resulting from their corresponding positions. The

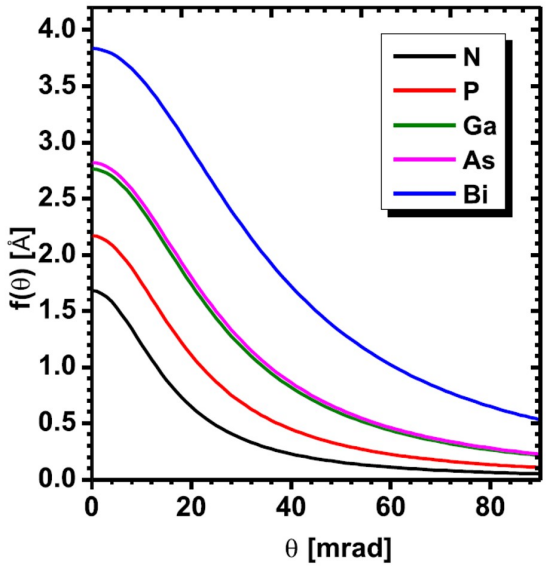

Figure 2.4: Diagram showing how the atomic scattering factor $f(\theta)$ changes with the scattering angle θ for group V elements with different aomic number Z. [41]

structure factor F(θ) is introduced and can be written as

$$F(\theta) = \sum_{i}^{\infty} f_i(\theta) e^{2\pi i(hx_i + ky_i + lz_i)} \tag{2.18}$$

where x_i, y_i, z_i and $f_i(\theta)$ are the atomic coordinates and the corresponding scattering atomic factor of the i-th atom. (hkl) is the corresponding atomic plane. The structure factor is widely applied in the X-ray diffraction and conventional TEM. It determines whether a diffraction spot is chemically sensitive or strain sensitive or forbidden.

2.2.2 Kinematical/dynamical scattering, channelling, and beam broadening

Kinematical/dynamical scattering

Electron scattering can be described by two different theories: Kinematic scattering and dynamical scattering. Kinematic scattering assumes that each particle from the probe (e.g. electron, neutron, or X-ray photon) can be scattered once or suffer from no scattering, and therefore the probe intensity is almost not decreased. The single scattering assumption agrees well in the case of neutron and X-ray scattering due to the weak interaction. It is also a good approximation for electron scattering in very thin samples. However, if the sample is relatively thick, the electron can be scattered more than once and it is termed as plural scattering. If the electron is scattered more than 20 times, then it is referred to as multiple scattering [39]. Under this circumstance, kinematic scattering will result in an overestimation of the scattered intensity. Dynamical scattering is therefore introduced in order to describe the plural scattering and multiple scattering.

It becomes more difficult to describe the dynamical scattering as more scattering events occur. In application, the TEM samples are alwayse prepared as thin as possible. Besides, the multiple scattering can lead to the so-called cross talk [29], [42]–[44] between the adjacent atomic columns in thick TEM samples. Since the scattered intensities are redistributed between neighboring atomic columns during cross talk, significant deviations can be produced during quantitative evaluation of the image. Therefore, the cross talk should be avoided through measurement at thin regions of (S)TEM samples.

Beam broadening

In TEM, the electron probe is generated by the electron gun and a group of probe forming lenses. The probe size is determined by the electron source size, lens aberrations and electron diffraction at the condenser aperture. When the electron beam propagates through the TEM sample, probe broadening takes place. In fact, the beam broadening begins before the collision with the sample due to the coulomb force between the electrons. Owing to the low beam current, this beam broadening effect can be neglected. During the interaction inside the sample, the beam broadening is mainly contributed by two factors: the beam divergence effect (2αt) and the broadening caused by elastic scattering as illustrated in figure 2.5. The beam divergence effect can be easily calculated from the convergence semi-angle (α) and the sample thickness (t). The broadening effect resulting from elastic scattering can be expressed by [45], [46]

$$b_2 \approx (625cm)(\frac{\rho}{A})^{\frac{1}{2}}\frac{Z}{E_0}[t(cm)]^{\frac{3}{2}} \tag{2.19}$$

where Z is the atomic number, A is the atomic weight, ρ is the density of the investigated material in g/cm^3 and E_0 is the applied energy for the incident beam in keV. These two effects can be simply added in quadrature in an approximation.

In spectroscopy and STEM, beam broadening determines the spatial resolution for the analysis of nanoparticles and nanostructures, especially for X-ray energy dispersive spectroscopy (XEDS). Most importanly, the parameters of the electron probe can be properly chosen in simulation to agree better with the experimental setups. In addition, when a supercell is generated for the STEM simulation, the supercell should have a large enough size perpendicular to the beam direction, so that the intensity is not partly lost at the edge of the supercell due to the beam broadening effect.

Channelling

Electron channelling describes the phenomenon when an electron probe is situated at an atomic column (usually the major zone axis of the crystal), the electrons will travel along the column due to the attraction from the electrostatic potential. During the

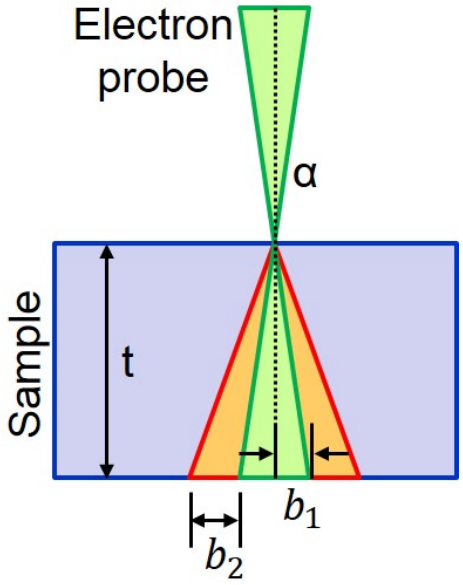

Figure 2.5: Illustration of the electron broadening inside the sample. b_1 is caused by beam devergence effect and b_2 is result from the elastice scattering. Both effects can be added in quadrature in a first approximation.

channelling process, the intensity oscillations of the wave at the atomic site can be viewed as a funcction of depth in the crystal. The electron channelling can be regarded as the exciation of the strongly localised 1s-type states [20] according to a Bloch wave analysis. Bloch waves are the solutions to the Schrödinger equation in a crystal. Due to the periodic potential, bloch waves also have the required translation feature of the crystal. The channelling effect strongly depends on the sample thickness and can be greatly influenced by the existence of defects or strain-induced lattice bendings. On the other hand, under some conditions, electron channelling occurs, which can alleviate the beam broadening effect. Besides, as shown in figure 2.6, the doping atoms or clusters situated in the investigated atomic column can influence the 1s state of the electron beam and hence affect the channelling process.

2.2.3 Coherent and incoherent imaging

In respect of the wave nature of the electron beam, the electron scattering can be divided into coherent scattering and incoherent scattering. To better understand the difference between coherent and incoherent scattering, we start with the phase changes happening during the scattering. As already mentioned in sections 2.1.3 and 2.2.2, if the scattered waves are in phase (e.g. the phase differences are the integer multiple of 2π), this results in constructive interference. Similarily, a fixed phase difference of π can lead to the annihilation of the amplitudes (destructive interference). In both cases, since the scattered

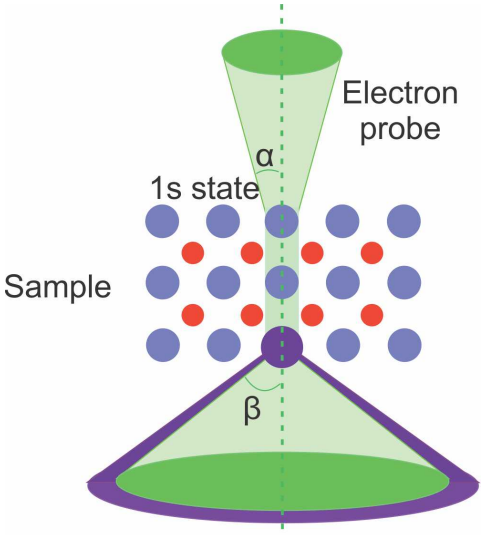

Figure 2.6: Schematic illustration of the electron channelling. The purple atom denotes a heavy doping atom.

waves are in phase, they are coherent. On the other hand, if the phase differences of the scattered waves are random, most waves can cancel each other out and this is called incoherent scattering. If a coherent plane wave is scattered by randomly spaced scatterers in a plane, the forward (on-axis) scattering usually suffer from the same phase change and therefore is coherent whereas the high angle (off-axis) scattering owing to the random arrangement of the scatterers is incoherent.

In the Conventional TEM (CTEM), in order to obtain the diffraction patterns and the diffraction contrast images, a coherent illumination source is needed. Also, the phase-contrast high resolution TEM (HRTEM) technique requires high coherence. In HRTEM a parallel coherent electron beam is used to illuminate the sample. The exit electron beam with a wavefunction ψ(R) is magnified by the objective lens and other lenses and then projected onto the detector/camera. The spherical lens aberration results in a blurring of the exit wavefunction in the image plane. The blurring can be described by a point-spread function P(R) and its convolution with the exit wavefunction is measured by the recording system as intensity. This coherent image can be mathematically written as follows

$$I_{coh}(R) = |P(R) \otimes \psi(R)|^2 \tag{2.20}$$

The intensity of the coherent image is influenced by the complex amplitude, which means the electrons scattered by spatially separated parts of the sample are in phase and result in either constructive or destructive interference. The image contrast can reverse as the defocus [47] or the sample thickness [48] is changed. Therefore, the corresponding HRTEM simulation is needed to determine whether atoms appear as bright or dark points in the image.

For the incoherent image, there is no interference between electrons scattered from different parts of the specimen. The mathematical defination can be expressed as

$$I_{incoh}(R) = |P(R|^2) \otimes |\psi(R)|^2 \tag{2.21}$$

Compared with equation 2.20, the incoherent image is a convolution in intensity instead of the complex amplitude. According to Lord Rayleigh [49], incoherent imaging provides a better spatial resolution than the coherent imaging, which can be explained by the optical transfer function as illustrated in figure 2.7. Besides, there is no phase reversal concerning the defocus or the sample thickness. The obtained image is easy for interpretation without any contrast simulation. Together with the contrast simulation, the obtained image can be quantitatively evaluated to get the information like chemical composition, interface roughness and so on.

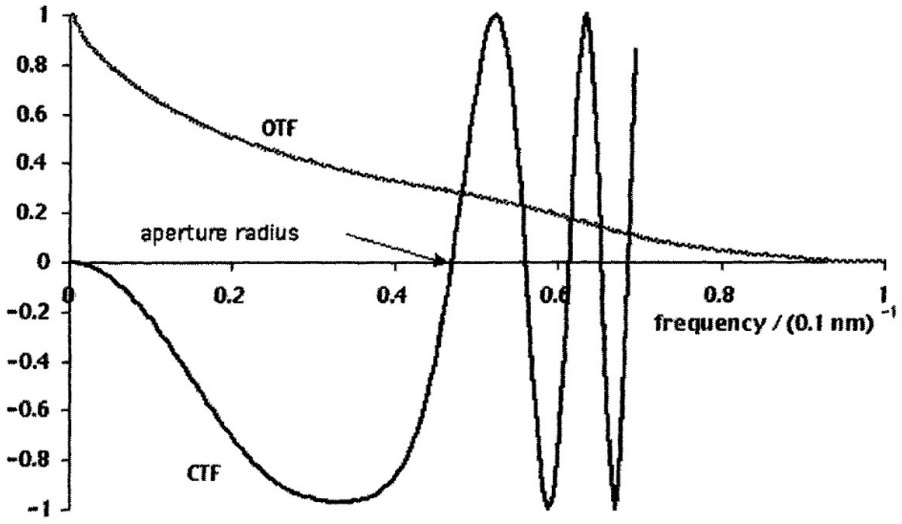

Figure 2.7: The optical transfer function (OTF) for incoherent image and the contrast transfer function (CTF) for coherent image with the same defocus and spherical aberration. The used objective aperture for OTF is marked in the figure[50].

2.2.4 The resolution and lens aberrations

For an ideal optical system, a single point source will be imaged as a series of concentric rings and the central brightest disc is termed as the Airy disc [51]. The distinguish of two incoherent point sources is defined as the theoretical resolution of a lens and is influenced by diffraction effects. According to Rayleigh criterion, the theoretical resolution can be expressed as follows:

$$r_{th} = 1.22\frac{\lambda}{\beta} \tag{2.22}$$

where r_{th} is the theoretical resolution, λ is the wave length of the electron beam and β is the collection semi-angle of the lens.

However, in reality, due to the imperfection of the lens, the resolution of a lens can be greatly influenced by mainly two abberations, namely monochromatic aberration and chromatic aberration [51]. The monochromatic aberration can be divided into spherical aberration, astigmatism, coma, field curvature and distortion. This section will focus on spherical aberration, astigmastism, coma and chromatic aberration.

Spherical aberrations are mainly caused by the fact that the off-axis rays are not focused on the same point as paraxial rays due to the strong deflection effect at the edge of the lens. The aberrations of the objective lens are most important, since they not only can deteriorate the quality of the TEM image but also will be further magnified by the other lenses. As shown by the sketch in figure 2.8 (a), the best resolution happens at a plane termed as 'plane of least confusion' or 'plane of minimum confusion' instead of at the Gaussian image plane formed by paraxial rays. The radius of this plane is given by

$$r_{sph} = 0.25 C_s \beta^3 \tag{2.23}$$

where C_s is the spherical aberration coefficient and is a constant for a particular lens. It has a dimension of length and is usually a few millimeters.

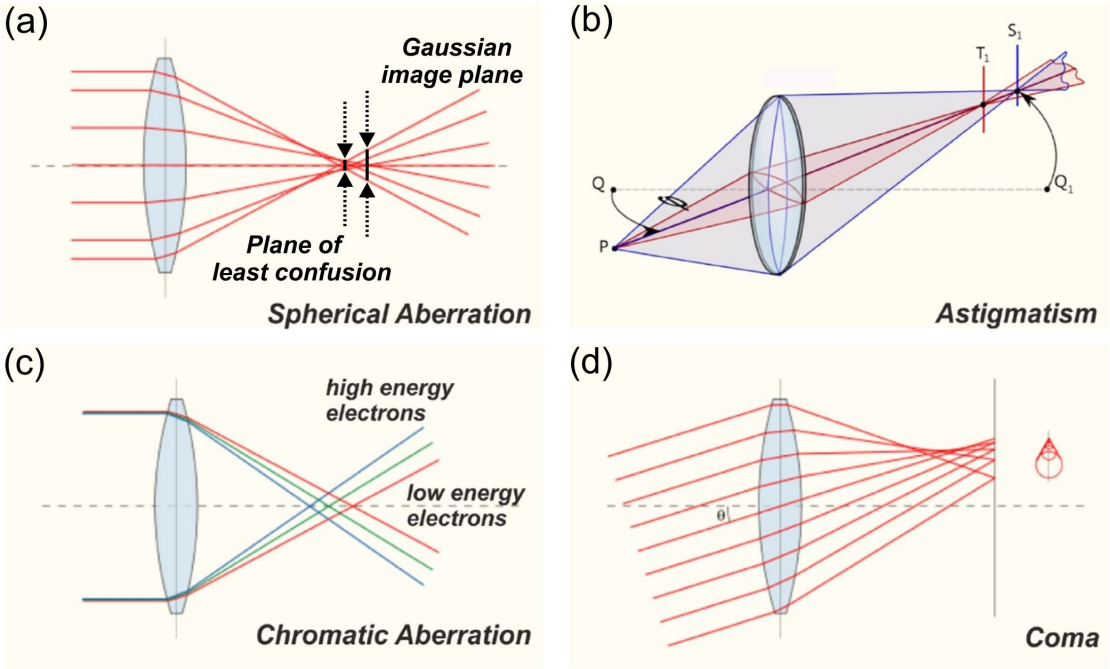

Figure 2.8: Schematic illustration of the spherical aberration (a), astigmatism (b), chromatic aberration (c) and coma (d). The gaussian image plane and plane of least confusion are marked the arrows in (a), modified from Ref [52].

Astigmatism exists commonly for all the lenses due to the heterogeneous magnetic field, which can be caused by either the non-cylindrical soft iron or the microstructural textures inside the iron or the nearby apertures. Because of astigmatism, the cross-over of the off-axis rays is shifted along the optical axis as illustrated in figure 2.8 (b) and the degree of displacement depends on the azimuthal angle of the corresponding beam. The radius of plane of least confusion can be expressed as

$$r_{ast} = \beta \Delta f \tag{2.24}$$

where Δf is the maximum difference in focal length. Luckily, astigmatism can be easily corrected by exerting an external magnetic field to balance the inhomogeneous one with stigmators.

In the case of coma (comatic aberrations), when an object point source is slightly off the optical axis, the rays travelling through the center of the lens will be focused at a point deviated from the optical axis whereas the rays passing through the peripheral field of the lens will also be braught to different focus points as shown in figure 2.8 (d). The image of the object therefore appears to have a comet tail.

For the above mentioned aberrations, we have assumed that all electrons have the same frequency. In fact, the electrons produced by the gun do not satisfy the assumption and hence lead to the chromatic aberrations. Assuming that the lens is perfect and ideal, electrons with lower energy will be deflected strongly to the optical axis. Therefore, electrons with different wavelengths are focused at different positions along the optical axis as shown in figure 2.8 (c). Again, the radius of the plane of least confusion can be written as

$$r_{chr} = C_c \frac{\Delta E}{E_0} \beta \tag{2.25}$$

where C_c is the chromatic aberration coefficient and again has a dimension of length. ΔE is the energy loss during the electron-specimen interaction. E_0 is the initial energy. In fact, with development of the high voltage systems, the electron energy spread is usually smaller than one part of one million [39]. So chromatic aberration can be completely ignored unless a C_s corrector is applied. After the C_s aberrations are compensated, then the C_c aberrations will dominate the quality of the images. Chromatic aberrations increase with increasing specimen thickness due to the larger chances to loss energy. That is also the reason why a thin sample is desired during preparation.

As a result, the theoretical resolution can be improved according to the Rayleigh criterion (equation 2.22), if larger collection semi-angle β is used. However, under this circumstance, the resolution will deteriorate, since both spherical and chromatic aberrations will become larger. As β changes, there must be an optimum value for the best resolution. Detailed treatment is suggested to read Ref. [53].

2.3 The investigated III-V semiconductor compounds

Generally speaking, the semiconductor [54], [55] usually has a band gap of less than 3 eV. A materials with a band gap larger than 3 eV is regarded as an insulator. If the valence and conduction bands overlap with each other, then it is called a metal. The most common semiconductors are from group IV elements (e.g. Si and Ge), group III-V (e.g. GaAs) and group II-VI (e.g. CdSe). In semiconductors, the band gap is determined by the energy difference between the maximum of the valence band and the minimum of the conduction band. However, if the maximum and minimum positions do not share the same $\boldsymbol{k}$-vector ($\boldsymbol{k}$-vector is the wavevector in momentum space.), it is referred to as the indirect semiconductor, otherwise it is termed as direct semiconductor. Direct band gap materials provide more efficient absorption and emission of light for optoelectronic devices. The reason can be explained by the E($\boldsymbol{k}$) sketch in figure 2.9. For direct band gap semiconductors, an electron from the valence band can be easily activated to the conduction band by a photon with an energy larger than E_g and therefore an electron-hole pair can be created as illustrated in figure 2.9 (a). For indirect band gap semiconductors, the activation process is much more complicated, since an electron not only has to gain energy from a photon to overcome the energy gap but also has to suffer from a momentum exchange with a phonon to jump to the conduction band as shown in figure 2.9 (b). A photon [56], [57] is the quantum (fundamental particle) of an electromagnetic wave (e.g. light). The group IV elements, such as Si and Ge, have an indirect band gap, while most of the III-V compound semiconductors (except GaP and AlSb) possess a direct band gap. Therefore, III-V semiconductors are widely applied in the optoelectronic industries.

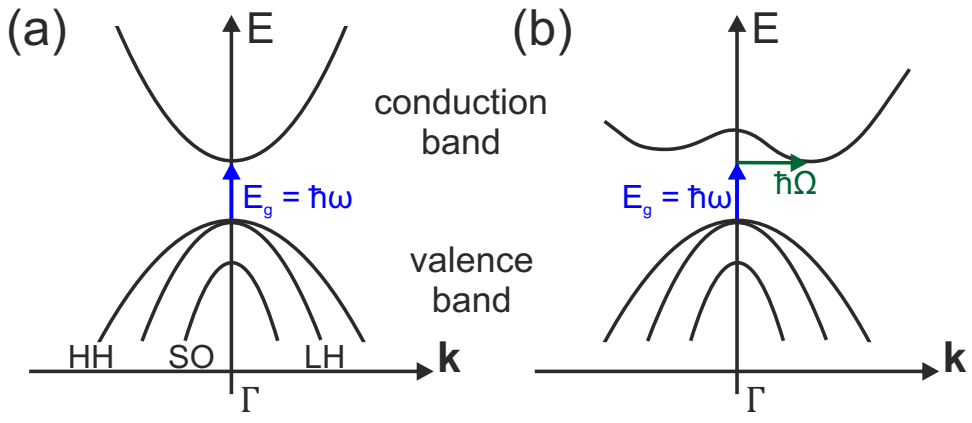

Figure 2.9: Schematic illustration of a direct (a) and an indirect band gap (b) with qualitative bandstructure of the valence band. The valence bands with different curvatures correspond to the different masses of the holes, the so-called heavy holes (HH) and light holes (LH). A third band slightly split off from the other two is caused by the spin-orbit interaction and is denotey by SO. The center of the Brillouin zone ($\boldsymbol{k}$=(0 0 0)) is denoted by Γ [58]

For the investigated III-V semiconductor in the current study, the linear combination of the 2s and 2p orbitals results in the four so-called sp^3 orbitals that stick out in a tetrahedral configuration. Every group III atom is surrounded by four group V atoms and vice versa. They can form either the zinc blende or wurtzite structure. There are in total 12 different combinations of the binary compounds and the corresponding band gaps vary in a large range. In modern semiconductor industries, III-V semiconductor compounds [59] are heavily studied because of their wide application in heterogeneous device designing. On one hand, the band gap of the ternary or quaternary compounds can be tunable within a large range by changing the corresponding composition. This process will change the lattice parameter according to Vegard's law [60], [61]. This means, on the other hand, the ternary or quaternary compounds can also be designed in the epitaxial growth, to generate the abrupt/intermixing, strained/unstrained interface. For the ternary or the quaternary compound, the lattice parameters can be simply determined by the Vegard's Law. Take $(Ga_{1-x}In_x)As$ for example, mathematically, it can be expressed as a solid solution of InAs in GaAs as

$$a_{(Ga_{1-x}In_x)As} = x \cdot a_{InAs} + (1-x) \cdot a_{GaAs} \tag{2.26}$$

where x is the fraction of InAs in GaAs. a denotes the lattice parameter.

The investigated materials, like (GaIn)As/GaAs, and (GaIn)P/GaAs, all have a zinc blende structure, which is composed of two basic sets of the fcc Bravais lattices, shifted along the body diagonal of the unit cell of GaAs by a quarter of the diagonal length as shown in figure 2.10. Group III and group V atoms are situated on one fcc lattice, respectively.

Nowadays III-V semiconductor devices are usually composed of mainly heterojunctions. With the miniaturization of the semiconductor devices in the past few decades, the devices can be regarded as the arrangement of many different interfaces. Therefore, the quality of the interfaces greatly determines the physical properties of the devices, since the interface structure and abruptness can significantly influence the scattering and recombination of the charge carriers. The inferface morphology can be controlled to some extent by the growth temperature, the application of the growth interruptions (GI) and the introduction of interlayers. To understand the growth process and optimize the growth parameters, the investigation of the interface structure at atomic resolution is crucial.

2.3.1 (GaIn)As/GaAs

As a promising candidate in optoelectronic and microelectronic devices, especially in the long wavelength vertical cavity surface emitting lasers (VCSEL) towards the telecommunication applications, (GaIn)As/GaAs quantum well structure [62]–[64] has attracted a

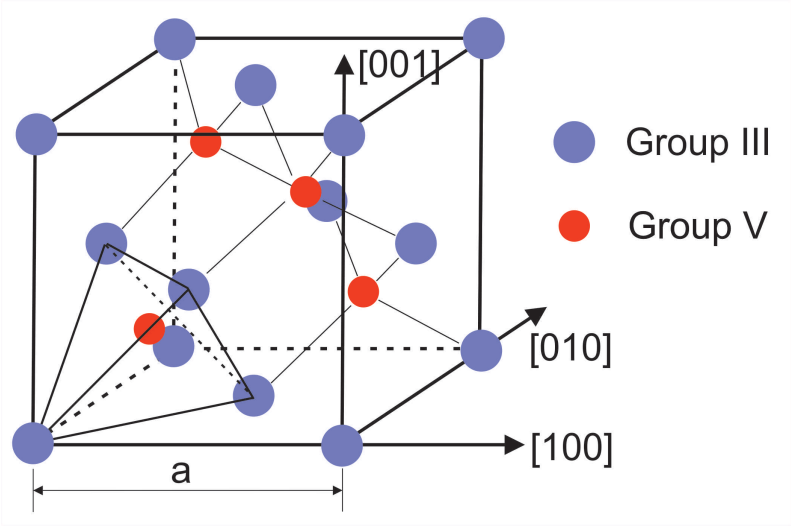

Figure 2.10: Schematic illustration of one unit cell in Zinc blende structure and the corresponding crystallographic direction. Every group V atom is located in a tetrahedron composed of four group III atoms and vice versa.

lot of interest in the past few decades. The especially high electron mobility and high ratio of electron to hole mobility of $(Ga_{0.47}In_{0.53})As$ [65] can significantly improve the device efficiency, noise and power consumption. In the heterostructure semiconductors, the high performance devices are realized by abrupt high quality interfaces. However, the heteroepitaxy of (GaIn)As on GaAs is strongly influenced by the indium atom segregation [66]–[68] at the interface. During epitaxial growth, the In atoms tend to accumulate at the growth front and hence alter the In distribution and the interface morphology.

2.3.2 (GaIn)P/GaAs

(GaIn)P/GaAs [69]–[71] has drawn much attention in the last few years due to the application in the optoelectronic and electronic industries, for example, heterobipolar transistors, lasers, solar cells and so on. The excellent physical properties, such as low deep level concentrations, a large valence band discontinuity and the low recombination velocities at the (GaIn)P/GaAs interface [72] make it a promising materials in the future. However, the wide application is greatly limited due to the poor physical qualities. In fact, a desired abrupt heterointerface can not be acquired so easily [73]–[75] because of the memory effect [5] occured in the growth reactor. Memory effect is referred to as the incorporation of the residual atoms grown into the subsequent layer. Besides the memory effect, the exchanging mechanism caused by the different bond energy [76], the mixed phases and/or quaternary phases including the As/P rich interfaces could also be present at the interface and thus deteriorate the interface quality.

3 Experimental and Numerical Methods

In this chapter, the epitaxy growth of the investigated materials is briefly introduced in section 3.1. The characterization methods, like high resolution X-ray diffraction (HRXRD) and atomic force microscopy (AFM), which can be directly measured without sample preparation, are explained in sections 3.2 and 3.3, respectively. After the (S)TEM sample preparation is introduced in section 3.4, the principles of STEM and ADF imaging are presented in section 3.5. To better understand the STEM imaging, the corresponding simulation is briefly introduced in section 3.6.

3.1 Metal organic vapor phase epitaxy

In this study, the investigated ternary material systems are grown by metal organic vapor phase epitaxy (MOVPE), also known as MOCVD (metal organic chemical vapor deposition), which is a complex process for the industrial production of III-V compound semiconductor thin films. The materials can be widely used as lasers, transistors, solar cells and so on.

In MOVPE system, the liquid metal organic precursors, stored in separate closed stainless steel containers (bubblers), are connected to the reactor via a special stainless steel pipe. During growth, the gas phase of liquid precursors are transported separately into the reactor by the highly purified hydrogen carrier gas, to avoid the chemical reactions during transportation. In the reactor, the substrate is located on a graphite plate, embedded in a graphite block (susceptor). The temperature of the substrate can be controlled by infrared lamps and measured by a temperature sensor inside the susceptor. At a high temperature, the mixed gas phase precursors decompose and react with each other on the substrate. Then the decomposed III/V metals are incorporated into the crystal while the organic gases are guided into the exhaust system, in which the toxic productions are filtered by a scrubber before they go to the atmosphere. To get the homogeneously deposited thin films, the whole system can be rotated via gas flow. The growth is based on a non-thermal equilibrium and therefore is favorable to grow metastable materials.

The investigated (GaIn)As/GaAs and (GaIn)P/GaAs material systems were grown in a commercial AIXREON AIX 200 with triethylgallium (TEGa) and trimethylindium (TMIn) as group III source and tertiarybutylarsine (TBAs) and tertiarybutylphosphine (TBP) as group V source. The qualities of thin films, including layer uniformity, interface

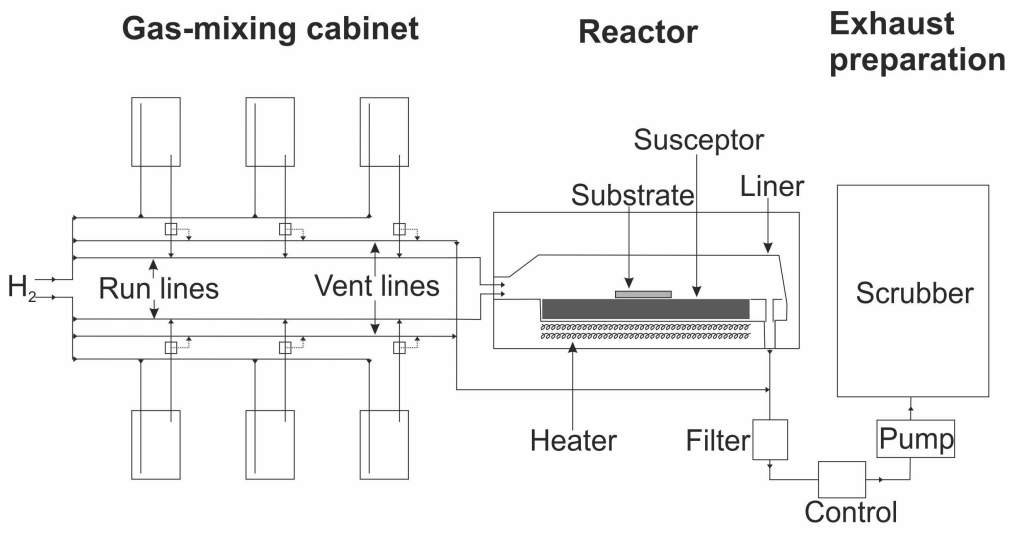

Figure 3.1: Schematic illustration of a MOVPE reactor system with its gas-mixing cabinet, reactor and exhaust preparation. [77]

abruptness, crystalline quality and so on, are mainly determined by the growth parameters like pressure, growth temperature, growth interruption, group III/V ratio. Detailed information of MOVPE and the corresponding growth theory [78] are not discussed here. This work is mainly focussed on the quantitative evaluation of the internal interfaces of III/V semiconductors and the influences of the growth conditions on the interface morphologies. In total, 11 different experimental samples are numbered and presented in this study. The detailed growth conditions and the layer structures are shown separately, together with the results in the following chapters.

3.2 High resolution X-ray diffraction

As a non-destructive method, high resolution X-ray diffraction (HR-XRD) is widely applied to determine the structural information of the materials, especially for the epitaxially grown thin films, such as layer thickness, chemical composition, strain and so on. Like neutron and electron diffraction, the theoretical foundation of HR-XRD is Bragg's law (equation 2.10), which describes the spatial relationship between the coherent elastically scattered waves and the crystal lattice. The epitaxially grown thin films can be directly measured by HR-XRD without sample preparation. The measurement is proven to be accurate and reliable, since the information of a large volume of the crystal is collected. However, due to the low resolution, the information at the interface or individual atomic column is unavailable. Therefore, HR-XRD is used in this study just as an auxiliary method and the quantitative evaluation at atomic resolution is carried out with scanning transmission electron microscopy.

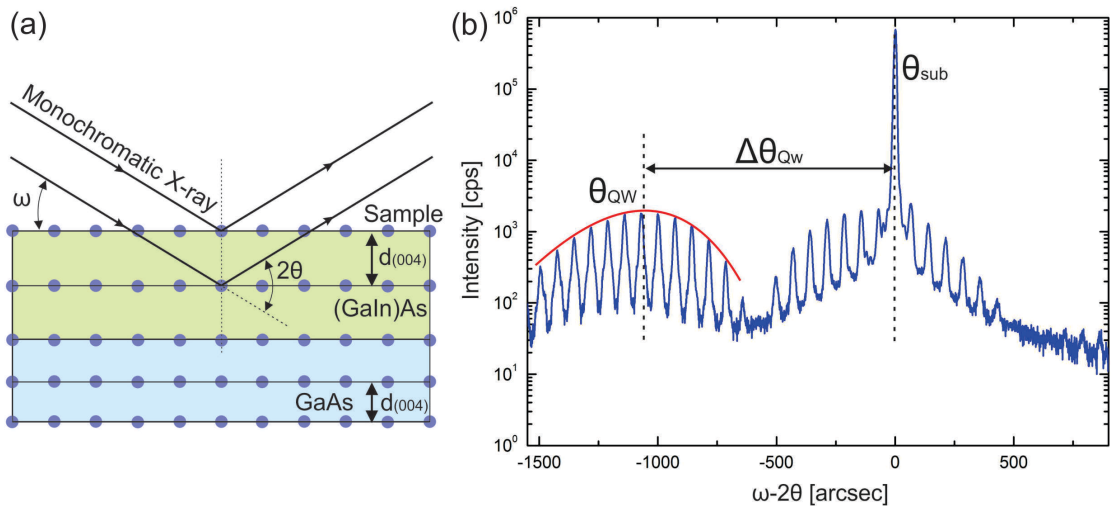

Figure 3.2: (a) Schematic illustration of the HR-XRD (004) ω-2θ scan. The X-rays hit the sample surface with an angle of ω. 2θ is the angle between the incident and scattered X-rays. Due to the addition of In into GaAs, the corresponding lattice parameter is enlarged. During the pesudomorphous growth, (GaIn)As will have the same lattice parameter as GaAs in the in-plane directions while the lattice will be elongated along the growth direction to obey the volume conservation law. (b) An examplary rocking curve of the (GaIn)As grown on GaAs with five repetitions. As marked in (b), θ_{sub} is the peak caused by the substrate. θ_{QW} (red curve) denotes the peak caused by the QW. It is composed of several satellite peaks because of the superlattice. The angle difference $\Delta\theta_{QW}$ between θ_{sub} and θ_{QW} can be used to determine the strain between the QW and the substrate.

In the current study, the rocking curve is measured in a Panalytical X'Pert Pro system. During the measurement, the applied (004) ω-2θ scan is used to determine the average chemical composition of the quantum well for further quantitative evaluation at atomic resolution. Because the sample growth takes place on (001) GaAs substrate in MOVPE (the sample surface is parallel to the (001) atomic plane), the angle ω between the incident X-rays and the sample surface is equal to the Bragg angle θ between the reflected beam and the lattice plane as shown in figure 3.2 (a). Also, for the pseudomorphous grown layer, (GaIn)As QWs will share the the same lattice constant in the in-plane directions but will be deformed along the growth direction. Due to the large In atoms, the atomic plane distance of (GaIn)As unit cells along growth direction (e.g. $d_{(004)}$) will be elongated and therefore result in a new peak in the rocking curve. This deformation can be detected and measured by rocking curve and further be used to calculate the chemical composition of the QW. The detailed explanation is suggested to refer to Ref. [58] and [79] and the basic steps can be found as follows. As shown in figure 3.2 (b), the strain ε between the quantum well and the substrate can be determined by

$$\varepsilon = \frac{a_{QW}^{\perp} - a_{sub}}{a_{sub}} = -\Delta\theta_{QW} \cdot \cot(\theta_{sub}) \tag{3.1}$$

where a_{sub} is the lattice constant of the substrate. $a_{QW}^{\perp}$ is the deformed lattice parameter of the quantum well along the growth direction. $\Delta\theta_{QW}$ is the angle difference between θ_{sub} and θ_{QW} as marked and explained in figure 3.2. After the $a_{QW}^{\perp}$ is determined, using the elastic constants C_{11} and C_{12}, the relaxed lattice parameter a_{rel} can be calculated as follows

$$a_{rel} = \frac{C_{11}}{C_{11} + 2C_{12}}(a_{QW}^{\perp} - a_{sub}) + a_{sub} \tag{3.2}$$

The relaxed lattice parameter a_{rel} can be applied into Vegard's Law, which is explained in detail in section 2.3, and the chemical composition of a ternary QW can be easily determined.

3.3 Atomic force microscopy

Besides HR-XRD, the epitaxially grown sample can also be directly measured by atomic force microscopy (AFM) to reveal the top surface morphology. In order to investigate the internal interface, the measurement can be carried out after the top layer is etched away. In the current work, the tapping mode is applied to carry out the AFM measurement with a Digital Instruments MultiMode SPM. As a simple and non-destructive method, AFM works through a raster scan of a tip fixed on a cantilever over the sample surface. During the scan process, the short-distance surface interactions, e.g. coulombic interactions and van der Waals interactions are recorded and analyzed. The position of the cantilever, which vibrates with its resonant frequency in tapping mode, is tracked by a laser beam, which is reflected from the cantilever to a photo detector. Both the resonant frequency and the amplitude of the oscillation are influenced by the force exerted by the tip-surface interaction, determined by the distance between the tip and the sample surface. Therefore, the distance between the tip and the sample surface can be measured through the change of the amplitude of the oscillation. A feedback circuit is used to maintain a constant amplitude of oscillation. Since the distance between the tip and the sample surface is kept constant, the positions of the cantilever, controlled with extreme accuracy by the scanner (usually piezo crystal), can be used to construct the 3-D image of the sample surface. The corresponding images are analyzed using Gwyddion and NanoScope from Digital Instruments company. The vertical resolution (z-direction) can be up to 0.1 nm to realize atomic resolution, however, the lateral resolution (x-y-direction) is relatively low (around 30 nm) due to the convolution effect.

3.4 (S)TEM sample preparation

After the samples are fabricated with MOVPE, they need to be carefully prepared before the characterization in STEM. Since the samples can be directly measured by HR-XRD and AFM without preparation. This section is mainly focussed on the sample preparation of inorganic semiconductors for STEM. In fact, the samples can be prepared with either focused ion beam (FIB) method [80] or conventional mechanical preparation method. In this study, since all the investigated samples are applied with the latter method, FIB is not dealed with. The sample preparation begins with a wafer with a special layer structure and ends with an electron-transparent cross-section sample. Generally speaking, this process is divided into three different stages, namely pre-preparation, mechanical thinning and ion thinning. Now let's have a look at the preparation in detail in the following parts.

Pre-preparation involves the processes from cutting of the wafer into small TEM samples. First two small pieces usually with a size of 5 mm × 5 mm are cleaved from the wafer marked by the broken lines in figure 3.3 (a). During cleavage the direction of wafer should be taken care, to make the TEM sample with the desired zone axis. After the two small pieces are cleaned with acetone and propanol, they are face-to-face sandwiched together with an epoxy, which is a mixture of 10 drops of resin and 1 drop of hardener. The epoxy becomes hard after heated for 15 minutes at 120 °C. The glued sample is then fixed on a round plate with wax. The wax melts at around 100 °C, at which temperature the epoxy is still hard. With the diamond saw, the small pieces is cut into small TEM samples (usually 1.8 mm × 0.9 mm) with a specific zone axis (e.g. [010], [110]) according to applied cutting angles as illustration in figure 3.3 (b). After heated, the TEM samples can be removed from the plate. Again they are cleaned with acetone and propanol and stored in a labelled box for further treatment. Then the pre-preparation process is finished and the samples are ready for thinning to be electron transparent.

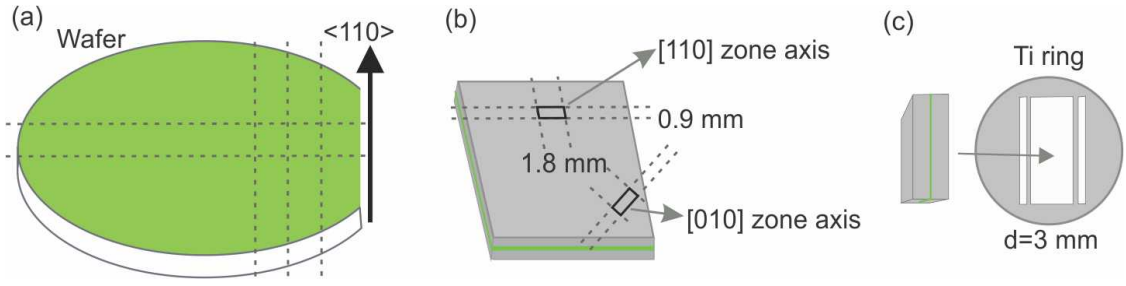

Figure 3.3: Schematic illustration of (a) TEM samples cut from the wafer and (b) the determination of the zone axis and (c) the arrangement of a TEM sample into a Ti-ring. The orientation of the wafer is marked by the arrow. Detailed explanation is given in the text.

During mechanical thinning, the TEM samples are usually thinned from several hundred μm to around 20 μm. To realize this aim, two routine approaches can be used either by using grinding and polishing papers or by using multi-preparation machine.

To begin with the first method, the TEM samples have to be fixed in the slot in a titanium ring with a diameter of 3 mm as shown in figure 3.3 (c). Then the rings are glued on top of a steel pole with wax, and the pole can be later inserted into a steel ring stage during grinding or polishing as shown in figure 3.4 (a). The thinning process of the sample (Ti-ring) begins with grinding on silicon carbide(SiC) paper with a grit size of 800. The starting grit size is determined by the thickness and the hardness of the sample. For thicker and harder samples, coarse SiC paper with a grit size of 600 or even 320 can be used. The sample is thinned further with grinding papers of grit 1200 and grit 2400. If the surface of Ti-ring is composed of homogeneous scratches with grinding paper of grit 2400, it is ready for mechanical polishings on 3 μm, 1 μm and 0.25 μm polishing clothes, respectively. With a mirror-like surface, the polishing of one side of the sample is finished.

To polish on the other side, the pole together with the Ti-ring is heated until the wax melts. Then the Ti-ring is carefully turned up side down and glued at the same position on the pole with wax again. Then the same grinding and polishing procedures are applied just as the first side. The difference is that the thickness of the sample should be controlled during grinding and polishing. Usually the Ti-ring is mechanically grinded to a thickness of around 90 μm. After the mechanical polishing, the final thickness is around 70 μm. Theoretically, the deformed region caused by grinding/polishing should be removed by the next finer grinding/polishing, which, as a basic rule, applys for all the samples with different thinning methods. During the thinning process, everytime when the grinding or polishing paper is changed, the steel pole with the Ti-ring should be cleaned carefully with water and the steel ring stage should also be cleaned and exchanged accordingly, to avoid the cross contamination.

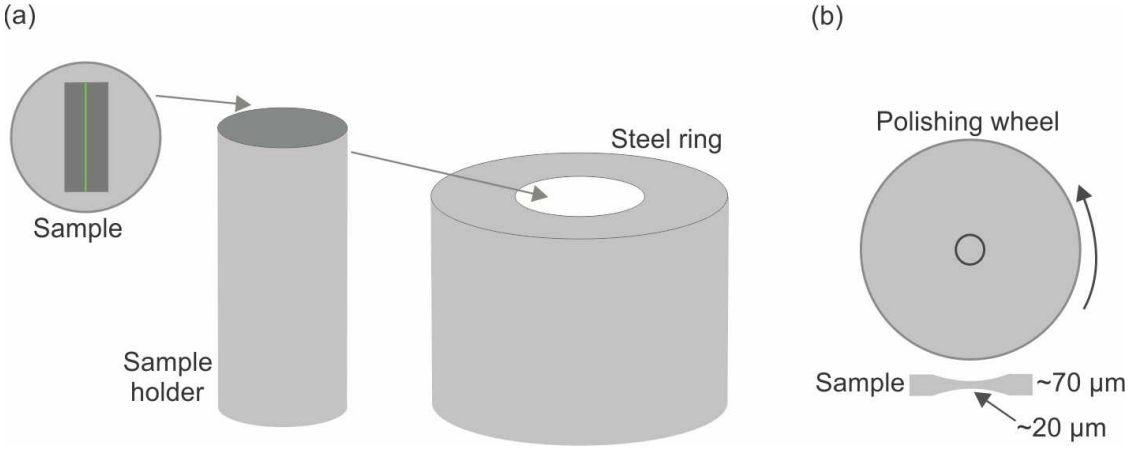

Figure 3.4: Setups of (a) the conventional mechanical thinning and (b) the dimpling grinder. Detailed explanation is given in the text.

Now the mirror-like sample is still too thick for the ion polishing. It has to be further thinned by wheels in dimpling grinder (Fischione model 200) as illustrated in figure 3.4 (b), in which the sample can be mechnically grinded and polished. For the following ion polishing, a thickness of around 20 μm is expected at the dimple center. So the sample has to be removed in total around 50 μm from both sides by dimpling. Before grinding, the center of the sample should be well aligned with the center of the dimpler. The sample is grinded with 3 μm wheel and the removed thickness depending on the need can be changed accordingly. Then the sample is polished with 3 μm, 1 μm and 0.25 μm wheel and the removed minimum thicknesses for the last two steps are 9 μm and 3 μm, respectively. During each step, the diamond paste with the corresponding size should be used and the polishing is usually 15 minutes long with a weight of around 20 Gram. When one side is finished, the thickness at the thinnest part should be remeasured and the applied parameters for the other side should be changed to reach the final thickness.

Alternatively, the multi-preparation machine can be applied to thin the sample and the detailed parameters can be found in Ref. [81]. With this method, the cutted TEM sample is directly glued on a sample hold with wax. Then the sample is thinned on 9μm, 6μm, 3μm, 1 μm 0.5 μm and 0.1 μm diamond paper. During the thinning process, water is used as both cooling and lubricant agent except that the Green Lube is used for both 0.5 μm and 0.1 μm polishing. The thickness control again begins from the second side. When the thickness reaches 100 μm after grinding with 6μm diamond paper, an angle of 2° between the sample surface and the diamond paper is applied through changing the height of the corresponding screws. Theoretically, the sample can be directly grinded and polished to be electron transparent. In application, the sample is thinned to around 20 μm at the thinner edge. In the end, the sample has to be fixed on a ring for the ion polishing and also the STEM investigation. Compared with the first method, the multi-preparation method is much faster but it needs more experiences.

Ion thinning is carried out in a precision ion polishing system (PIPS) (Gatan model 691) to remove the degraded surface caused by mechanical grinding and polishing. In PIPS the argon ions polish the sample surface at a low angle of 4° with a voltage changing from 5 keV to 1.0 keV. With the so-called double sector polishing method, the electron transparent region has a wedge shape, which can significantly influence the quantitative evaluation. To minimize the thickness gradient and obtain a flat region, the single sector polishing method is applied [82]. The samples are polished by argon ions at a low incidence angle of 4° and the accelerated voltage varies from 3.5 keV to 1.0 keV. However, the flat electron transparent surface obtained with the single sector polishing method usually takes longer polishing time.

It is worth mentioning that the electron transparent sample should be plasma cleaned before the (S)TEM measurement to remove the hydrocarbon contaminations. In this study, all the samples were cleaned by the Argon-Oxygen plasma in a plasma cleaner

(Fischione model 1020) for 2 minutes. However, this process can severely destroy organic samples, since the organic sample is mainly composed of hydrocarbon bonds.

3.5 Scanning transmission electron microscopy

3.5.1 Principles of STEM

As a widely applied analytical technique, scanning TEM (STEM) has combined the features of both scanning electron microscopy (SEM) and TEM. In SEM, a focused electron beam is used to scan the sample surface in a raster manner. During this process, the generated secondary electrons are collected to form an image to show the surface topography. In contrast, TEM makes use of a parallel electron beam to illuminate the electron-transparent specimen. During the process, the transmitted electrons, carrying the corresponding chemical and structural information of the investigated sample, can provide the diffraction patterns, dark field images, weak beam dark field images, bright field images, HRTEM images and so on. In STEM, a focused electron probe is made use of to scan the specimen in a raster way. The transmitted beam is collected to obtain the information of the specimen. Since STEM shares similar beam paths with TEM, it can be realized in TEM setup easily. The introduction to STEM begins with the explanation of the construction of TEM. After that, STEM will be explained in detail.

TEM is suggested to be divided into three different components [39]: namely the illumination system, the objective lens/stage and the imaging system. The illumination system is composed of the electron gun and the condenser lens (CL). The objective lens/stage comprises the objective lens (OL) and specimen stage and is the most important part of the TEM, since it determines both the image and the diffraction pattern of the investigated sample. The imaging system contains intermediate lens (IL), projector lens (PL), viewing screen, detectors and cameras. The illumination system has two different working modes: parallel beam and convergent beam. The first mode corresponds to the TEM while the second mode is mainly used in STEM and convergent beam electron diffraction (CBED). The schematic construction illustration of STEM/TEM is shown in figure 3.5.

Here, we mainly focus on how STEM works. On the top of the setup a Schottky field emmission gun (FEG) is used as the electron source as shown in the sketch. In thermionic guns [83] the filament (cathode) has to be heated to a high temperature so that the electrons can overcome the energy barrier and be emitted to the outside of the solid whereas in FEG the working temperature of the filament is reduced due to the introduction of an electric field. The Schottky FEG is a balance of the advantages of both thermionic and FEG and can provide a relatively stable and bright eletron beam with a high emission current. In STEM mode, the emitted electrons are formed into a focused electron beam by the CL system. Together with the CL aperture, the CL system

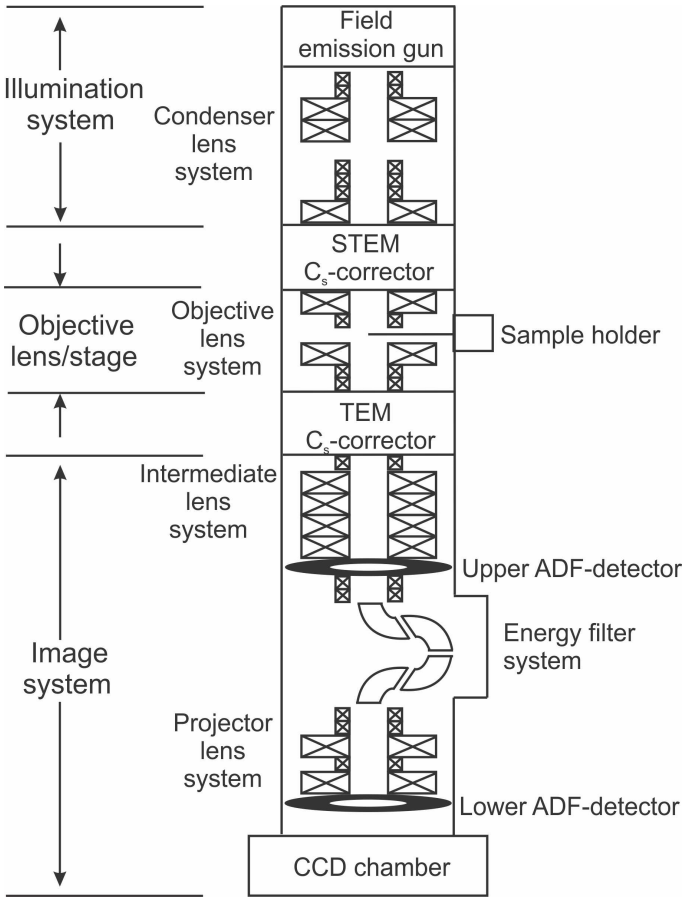

Figure 3.5: Construction of JEOL JEM 2200FS used in the present study with Cs-correctors for both TEM and STEM, modified from Ref [41].

can change the intensity and the convergence semi-angle of the beam. Below the CL, the installed STEM C_s-corrector can correct the spherical aberrations of the CL to provide better resolution. Then the corrected convergent electron beam, controlled by the scan coils, scans over the sample in a raster. The investigated sample is fixed on a goniometer stage in different sample holders. For example, the double tilted sample holder can control the sample position in x, y and z directions and tilt the sample in x and y directions. The sample holder is usually situated between the upper and lower pole piece of the OL. During the interaction between the probe and the sample, electrons carrying various signals are collected and plotted as a function of the probe position to generate the STEM image. By applying detectors with different shapes and sizes as illustrated in figure 3.6, the structural, compositional and electrical information can be obtained simultaneously or separately. The transmitted electron signals can be mainly divided into three different kinds:

1. Electrons that are deviated from the optical axis with relatively low angles [84] (usually smaller than the beam convergence angle). As illustrated in figure 3.6, the bright field (BF) detector usually collects electrons scattered from 0 mrad up to

around 24 mrad. According to the principle of reciprocity [85], the beam path in STEM imaging is equivalent to the beam path in conventional TEM and the detector in STEM should have similar role as the electron source in TEM as illustrated in figure 3.7. Therefore BF STEM imaging, like high resolution TEM (HRTEM) imaging, should have mainly the same phase contrast. If the signal of the phase contrast part of the transmitted beam disc, which is located in the center with an angle range of around 10 mrad, is removed with the annular bright field (ABF) detector, this ABF technique with a collection angle range from around 12 to 24 mrad can visualize both heavy and light atoms simultaneously. The atoms are viewed as dark points with a bright background. However, it is worth pointing out that the mentioned collection angles can change slightly depending on the investigated materials, since light and heavy elements have different scattering abilities. This principle also applies for descriptions in the following parts.

2. Electrons that are scattered to higher angles with respect to the optical axis. This is the so called annular dark field (ADF) imaging. Depending on the collection angle range, this mode is subdivided into medium angle ADF (MAADF) STEM and high angle ADF (HAADF) STEM. The collection angle is determined by the camera length (figure 3.6), which is the distance from the specimen to the detector and can be adjusted by the IL and PL. Compared with ABF STEM, MAADF detector excludes the whole transmitted beam disc and makes use of the zeroth order laue zone (ZOLO) (typically electrons scattered at around 25 mrad to 50 mrad at 100 keV) [86]. The MAADF imaging can be used to provide the information about the defects, interface roughness, boundaries and so on. By increasing the inner collection angle, the incoherently elastically scattered electrons can be collected by the HAADF detector. The HAADF STEM technique provides the so-called Z contrast, which means that the collected intensity of the imaging is proportional to the average atomic number of the atomic column and the specimen thickness. With the introduction of the spherical aberration C_s corrector, the resolution of HAADF STEM can be down to sub-angstroms.

3. Electrons which suffer from the inelastic collisions and lose some amount of energy. These electrons can be made use of to carry out the electron energy loss spectroscopy (EELS) analysis with the application of the in column Ω-filter (figure 3.5), which is located between the upper ADF detector and the projector lens system.

Besides the above mentioned signals, X-rays, generated during the measurement, can be used to do energy dispersive spectroscopy (EDS). For the inelastic scattering, the energy changes during the electron-specimen interaction can provide the corresponding structural and chemical information about the sample via EELS [87].

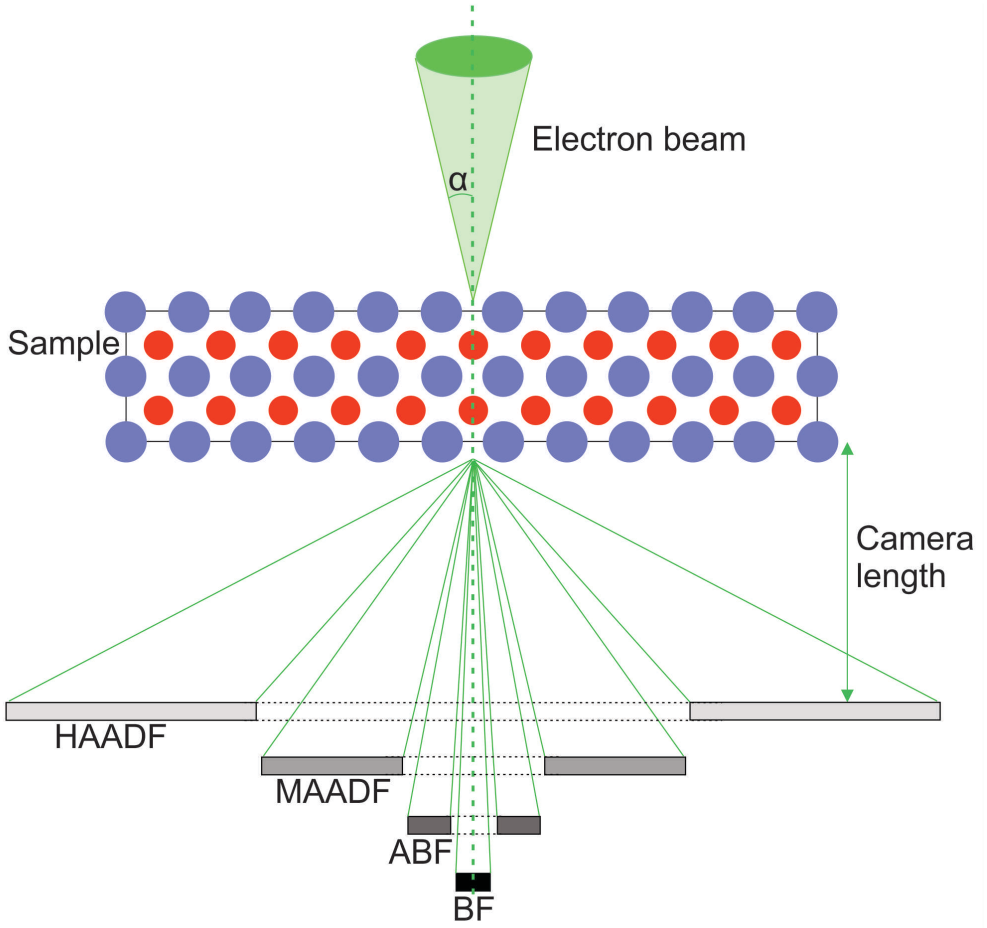

Figure 3.6: Schematic stacking of the mentioned detectors in STEM showing the different collection angle ranges and that different signals can be collected simultaneously. α denotes the convergent angle of the electron probe. The ring detectors are situated at different heights as also shown in figure 3.5. The broken lines indicates the unvisiable part of the annular detectors. Camera length is defined as the distance between the specimen and the detector. In reality, not all the mentioned detectors are installed in a TEM, because one detector can be used to collect different signals by changing the camera length.

3.5.2 ADF imaging

To understand the origin of contrast of STEM imaging technique, the reciprocity [85] is usually made use of. As mentioned in section 3.5.1, BF STEM imaging has the same phase contrast as HRTEM according to the reciprocity theorem as illustrated in figure 3.7. It states that if the electron source and detector exchange their positions, the electron intensity and beam path are still the same. The detector used in BF STEM works similarly to the illumination source in HRTEM and therefore the BF STEM images should be equivalent to the HRTEM images. The theorem only applies for the elastic scattering required by the reversible electron beam path between the source and detector. Besides BF STEM and ABF STEM imaging, it also works for the ADF imaging, which is based

on the high angle incoherent elastic electron scattering whereas the most coherent elastic scattering is excluded by the ADF detector.

In order to form the ADF image with Z-contrast, the coherence of the image must be removed in both transverse (perpendicular to the optical axis) and longitudinal (parallel to the optical axis) directions. The destruction of the coherence are mainly contributed by the detector geometry and thermal diffuse scattering (TDS). Other factors, such as electron source and aberrations, which can also result in the incoherent image, are not discussed in the study.

How detector geometry influences the ADF imaging can be again understood by the application of the reciprocity theorem. Based on Lord Reyleigh's suggestion, if an object is illuminated by an incoherent source over a large angle range, the object becomes self-luminous and the scattering from spatially different positions of the object can not be interfered with each other. The incoherent image is formed under this condition. The large source described here in TEM plays the same role as a large detector in the STEM. A large detector sums over large regions in transverse direction and thereby destroys the phase coherence. As mentioned in section 3.5.1, the transmitted disc is phase contrast and also dominates the intensity of the scattered electrons, therefore an inner hole is used to remove the influences from the transmitted disc and its neighboring regions. The inner collection angle should be at least three times the beam convergent angle [88]. Detailed mathematical explaination about how the detector geometry influences the imaging in STEM is given in Ref. [50]. As a result, a large ring detector with a large hole produce the incoherent images in STEM.

On the other hand, the longitudinal coherence is mainly destroyed by the phonon scattering. Phonon scattering is caused by the thermal atomic vibrations, which is composed of many modes with different frequencies and wave vectors. Every mode is referred to as a phonon, which deteriorates the periodic crystal potentials and further influences the electron scattering. Phonon scattering involves the exchange of both momentum and energy between the electron and the phonon. The electrons are mainly coherently scattered into the Bragg beams according to the elastic scattering whereas the inelastically scattered electrons are incoherent with the elastically scattered electrons and distributed within the Bragg angles. The energy, used for the generation or destruction of phonons, are in the order of tens of meV, which is far below the energy resolution (0.1 eV) of the energy spectrometer in the current microscopy. In addition, considering that the energy spread of a probe is usually around 0.25 eV, TEM can not easily distinguish the elastically scattered electrons and the thermal diffuse scattered electrons. The latter is also subsumed in the elastically scattering and dominates the incoherent nature of the ADF imaging.

It is worth mentioning [50] that the scattering to higher-order Laue zones (HOLZ) leads to the coherent scattering and hence contributes to the phase contrast. However, the HOLZ scatterings only produce some fine lines instead of discs. Therefore the collected

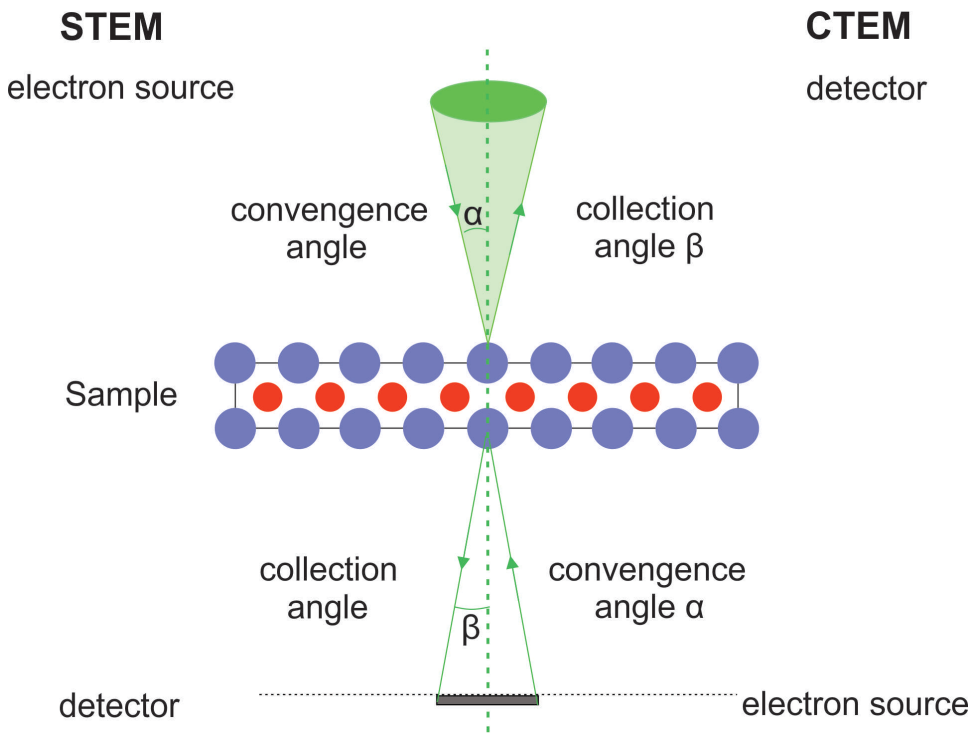

Figure 3.7: Schematic illustration of the equivalent beam path between BF STEM and HRTEM with the application of reciprocity theorem. The arrows indicates the electron travelling directions. The used lenses and apertures are not marked in the skectch. The reciprocity theorem can also be used for ABF STEM and ADF STEM.

HOLZ scatterings by ADF detector only amount to a tiny part compared with TDS at these angle ranges. The incoherence of ADF imaging is not affected at all.

In the present case, JEOL JEM-2200FS equipped with two spherical aberration C_s-corrector as shown in figure 3.5 is made use of, to characterize the sample at room temperature. In STEM mode, the emitted electrons, accelerated with a voltage of 200 keV, are focused into an electron probe by the CL system. Here, the CL aperture with a diameter of 40 μm is used producing a convergence semi-angle of 24 mrad. The STEM C_s-corrector installed under the CL system corrects the spherical aberrations of the CL system and provide a probe with a size of approximately 75 pm. Then the corrected convergent electron beam, controlled by the scan coils, scans over the sample in a raster. The scattered electrons are collected by the lower ADF detector (EM-24590YPDFI YAP detector produced from JEOL company) as illustrated in figure 3.5. The corresponding inner collection angle can be decided by measuring the size of its shadow on a charge coupled device (CCD) camera. For all measurements, the chosen camera length of 4 cm is used to obtain the HAADF images with atomic resolution, which corresponds to an inner collection angle of 73 mrad, whereas the outer collection angle is 4 times as large as the inner collection angle. In fact, the maximum outer collection angle is 173 mrad, decided by the geometric limitations of the microscope settings. At the beginning, the

HAADF images were recorded with a dwell time of 40 μs and a large size of 1024 $\times$ 1024 pixels. Later, a series of at least 6 frames with a size of 1024 $\times$ 1024 pixels and a short dwell time of 3 μs per pixel were acquired, aligned non-rigidly and then averaged for further quantitative evaluation [89], in order to improve the signal-to-noise ratio (SNR) and minimize the influence of drift during the measurement.

To compare the experiment with the simulation, the acquired images have to be normalized to the impinging beam and brought to an absolute intensity scale. The current of the impinging beam [90] (usually around 25 pA in the present study) was determined by its image recorded on the CCD camera (Orius SC2002), of which the conversion factor is 0.1087 electron/count, as provided by the manufacturer. After subtraction of the detector black level [91], which is the detector intensity without illuminaing the TEM sample, the intensity counts of HAADF images were also converted into currents by dividing them by the gain value of the detector system at fixed brightness and contrast settings. Then the image is normalized to the impinging beam according to the following equation:

$$I_{norm} = \frac{I_{exp} - I_{bl}}{I_{beam} - I_{bl}} \tag{3.3}$$

where I_{norm} is the normalized current and directly comparable to the simulations. I_{exp} is the experimental image current calculated from the intensity counts. I_{bl} is the mean black level current measured from the detector. I_{beam} is the current of the impinging beam.

3.6 Contrast simulation

Image simulation plays an important role in understanding both HRTEM and STEM images. For example, simulations are required to determine atomic positions for the phase contrast HRTEM images. Even if the incoherent images obtained with the HAADF technique are easy to interpret, the contrast simulation is also a necessity to understand the detailed structure of the specimen and to understand the image formation mechanism. Nowadays, with the development of quantitative evaluation of the HAADF STEM imaging, the simulation is widely used to determine specimen thickness, chemical composition and so on. In this section, the

3.6.1 Multi slice simulation

Generally speaking, there are two basic methods that can be used to carry out the STEM image simulation, namely the Bloch wave method [20], [50] and the multi slice method [92], [93]. The Bloch wave method makes use of the Bloch wave function, which satisfies the Schrödinger equation in the crystal. The method works well for the perfect crystal, since the defects or interfaces can severely influence the periodic potentials in the crystal. Also, it becomes very inefficient and requires more computing resources when the simulated

sample becomes larger. Multi slice method divides the investigated sample into many thin slices and then calculates the probe wave function after every slice. Besides relatively large supercells, it can also be used to simulate the defects and interface or amorphous materials. Due to the application of the fast Fourier transform [94], the efficiency is greatly improved.

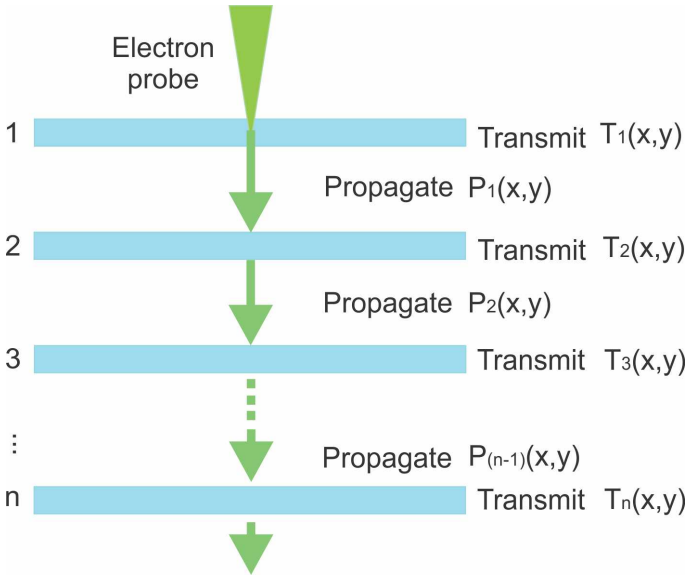

Figure 3.8: (s)TEM sample is split into many slices. The transmitting through the n^{th} slice and the following propagation in the free space are described by the transmission function T_n(x,y) and the propagator function $P_n(x,y)$, respectively. Both functions cause only a phase modification to the probe wave function. The amplitude of the probe wave function is not influenced.

Within this method, the TEM sample is divided into many thin slices with the same thickness, labeled as n=1, 2, 3, ... as shown in figure 3.8. The initial wave function ψ_1(x,y) is the probe wave function in the STEM mode. The probe wave function on top of the n^{th} slice is denoted by ψ_n(x,y). Then it propagates through the sample by transmitting through all the slices. For the n^{th} slice the atomic potential $v_n(x,y)$ is projected onto the first projection plane (phase grating) and each slice can result in a phase shift to the probe wave function due to this projected atomic potential. The transmitting process through one slice can be described by the transmission function T_n(x,y) [95]

$$T_n(x,y) = exp[i\sigma v_n(x,y)] \quad \text{with the interaction parameter} \quad \sigma = \frac{2\pi\gamma m_0 e\lambda}{h^2} \tag{3.4}$$

where m_0 is the rest mass, e is the charge of an electron, γ is the Lorentz factor and h is Plank's constant. Between each slice, the wave function propagates in the free space according to the Fresnel diffraction (near-field approximation), which is described by the propagator function $P_n(x,y)$. Mathematically, the repeated process can be expressed as

follows

$$\psi_{n+1}(x,y) = [\psi_n(x,y)T_n(x,y)] \otimes P_n(x,y) \tag{3.5}$$

where $\otimes$ indicates the convolution between the wave function and the transmission function of each slice. These are the basic ideas about multi slice method and more detailed explaination are not discussed in this study and can be found in Ref. [96]. To carry out the simulation, different methods and softwares have been developed.

3.6.2 Frozen phonon approach

As mentioned in the previous section, TDS dominates the contributions to the incoherent nature of HAADF images. Therefore, it is a necessity to include the TDS during the contrast simulation for the quantitative comparison between the experimental images and the simulated results. Two different methods have been developed to describe the TDS: absorptive potentials [97], [98] and frozen phonon [99]. Absorptive potentials gets its name from the adsorpted phenomenon of inelastically scattered electrons in the conventional diffraction contrast image as described as follows. The inelastically scattered electrons are distributed between the Bragg angles, due to the thermal vibration of the atoms. Therefore, if a Bragg diffracted spot is selected to form an image by a small objective aperture, the TDS electrons seem to be 'absorbed'. This absorptive effect can be included in the multislice method by adding an imaginary absorptive potential to the projected atomic potential $v_n(x,y)$. The detailed explanation and calculation process is explained in Ref. [43]. This method is fast and requires less computer resources compared to the frozen phonon approach. Though it agrees well with the experimental results, it is not appropriate for the quantitative evaluation due to the samll discrepancy between the calculation and the experiment. The frozen phonon approach is regarded as the most accurate method for the calculation of HAADF images [100]–[102] and therefore is applied for all the simulations in the current study.

The frozen phonon approach is put forward based on the following facts. Considering a most commonly used TEM with an electron acceleration voltage of 200 keV, the electron speed is 2.086×10^8 m/s taken into account the relativistic effects and the individual electron is spaced about 1 meter apart. It transmits a TEM sample with a typical thickness of 20 nm within 10^{-16} s, much shorter than a typical period of a lattice vibration of around 10^{-13} s. The thermally vibrating lattice seems to be stationary, when the electron transmits through the sample. Obviously, every time only one electron is inside the sample and it sees a different configuration of the atoms. Therefore a number of configurations of the lattice are applied to include the influence from thermal vibration during the simulation. In each configuration, the position of each atom is changed randomly with displacements caused by the thermal vibration. The thermal vibration is described by

the Debye-Waller factors [103]. Debye-Waller factor is widely used in electron diffraction and image calculations. Since it is resulted from thermal atomic vibration on the periodic potential of the crystal, it is mainly determined by the temperature and the crystal structurre. In the end, all the calculated images from different configurations are summed and everaged. The more configurations, the more accurate the simulation is. Also it requires more computing power and longer time.

3.6.3 Strain relaxation

To carry out the mentioned contrast simulations, firstly a supercell is created to simulate the TEM specimen. Basically speaking, two kinds of supercells are used in the present study: the bulk materials, like GaAs or GaP, which are used to determine the thickness of the investigated TEM samples, and the interfaces. During the epitaxial growth of a heterogeneous interface, due to the lattice mismatch between different layers, pseudomorphic growth can take place if the layer thickness is below a certain value. Pseudomorphic growth means that the layer shares the same lattice parameters as the previous layer perpendicular to the growth direction and suffers from either elongation or compression (tetragonal distortion) along the growth direction. As the sample is thinning down during the sample preparation, the stored strain at the interface can be relaxed to minimize the total energy. The relaxation can change the sample geometry and lead to lattice plane bending. The bending can influence the electron channelling effect and therefore the collected intensity by the annular dark field detector [104]. To find out how the strain relaxationat the interface influence the HAADF imaging [105], [106], the corresponding simulation is necessary. In this study, after the TEM sample is modeled, it is further relaxed with the COMSOL Multiphysics®suite by applying periodic boundary conditions [107]. The relaxed supercell is then applied in the multislice simulation.

HAADF contrast simulations are carried out with both STEMsim [108] and STEMsalabim [95]. Both softwares are based on the multi slice method. To include TDS, frozen phonon method is applied during the simulation. STEMsim has already been widely used in the simulation of both STEM and TEM images [23], [25], [26], [109]. The software allows to simulate both bulk materials and the interface with different approaches. Besides frozen phonon, absorptive potential approach is also available together with multi slice method or Bloch wave method. This software, written in Matlab language, can be run on desktop computers with many processors. However, it is not suitable for massive parallelization on high performance computing clusters. Therefore, the simulation is limited by the relatively small size of the supercell or interfaces.

Compared with STEMsim, STEMsalabim is specially designed for the application in high performance computing clusters on many computing nodes. The contrast simulation of relatively larger supercells can be finished within an acceptable time scale. STEMsalabim has calculated 10 different phonon configurations to include TDS with the multi

slice method. In addition, in order to take into account the chromatic aberration, it has computed a series of 7 defocus for each phonon configuration. Since a new configuration is generated for each defocus, in total 70 different phonon configurations are used in STEMsalabim to provide a robust result. In the current study, the constast simulation was carried out with STEMsim at the beginning stage. Then the contrast simulations were carried out with STEMsalabim after it is available. However, no matter which software is used, the parameters for the simulation are determined by considering the microscope settings. The applied parameters for the simulation of bulk materials are listed in table 3.1. According to the need, the simulations of bulk materials, e.g. GaAs, GaP, $(Ga_{0.5}In_{0.5})P$ and 5 super cells with strained interfaces are investigated. The detailed results are presented together with the corresponding experimental samples in the following chapters.

Table 3.1: Parameters used for the multi slice simulation with frozen phonon approach

Acceleration voltage HT	200 kV
Defocus C1	-2 nm
Spherical aberration C3	2.3 μm
Spherical aberration C5	5 mm
Objective aperture angle	24 mrad
HAADF collection angle	73 mrad -173 mrad
Specimen thickness	Up to 50 nm
Zone axis	[010]
Number of phonon configuration	15
Pixel size of simulated image per unit cell	50

4 Simulation of the investigated materials

This chapter presents the main results about the contrast simulation for the current study. In section 4.1, the influences of TDS on the collected intensity by the detector is discussed. Then the required minimum number of phonon configurations is studied in order to describe the thermal vibration properly using the least computing time and resources. Section 4.2 deals with the simulated results of bulk GaAs, which is used to determine the thickness of the investigated region of all experimental samples. The image background intensity, which can significantly influence the quantitative evaluation of the HAADF STEM images, is discussed in section 4.3 through the simulation of different materials.

4.1 Determination of the configuration number for frozen phonon approach

To carry out quantitative evaluation of the HAADF STEM images, contrast simulation is a necessity. Since the TDS dominates high angle scattering, thermal atomic vibration should be taken into consideration during the simulation. To find out the influences of thermal atomic vibration on high anlge scattering, GaP bulk material with a thickness of 50 nm is used to find out its different performances at both 0 Kelvin and 300 Kelvin. After simulation, the scattered mean intensity of one GaP unit cell is plotted against the scattering angle from 30 mrad to 300 mrad as shown in figure 4.1. Obviously, atoms are stationary at 0 Kelvin without vibration. Therefore, the scattering mainly takes place at the Bragg angles (holz lines) as mentioned in section 3.5.2 whereas the scattered intensities between the Bragg angles are extremely small and can be ignored. At 300 Kelvin, due to thermal atomic vibration the atoms are shifted from the ideal positions with a random displacement, which obeys a gaussian distribution. Correspondingly, the Bragg conditions are changed as well. The scattered intensity distribution is also significantly changed and the intensities at Bragg angles are redistributed between the Bragg angles and holz lines at high angles can not be observed any more. As a result, TDS should be included in the HAADF STEM simulation.

It has already been confirmed in section 3.6.2 that frozen phonon is the most complete approach to calculate TDS, if enough number of the lattice configurations is applied during calculation. However, this can result in the extremely long computing time and occupation of huge computing resources. Therefore, to save time and computing resource,

it is quite important to find out the minimum number of atomic configurations used for the frozen phonon method to obtain realiable results.

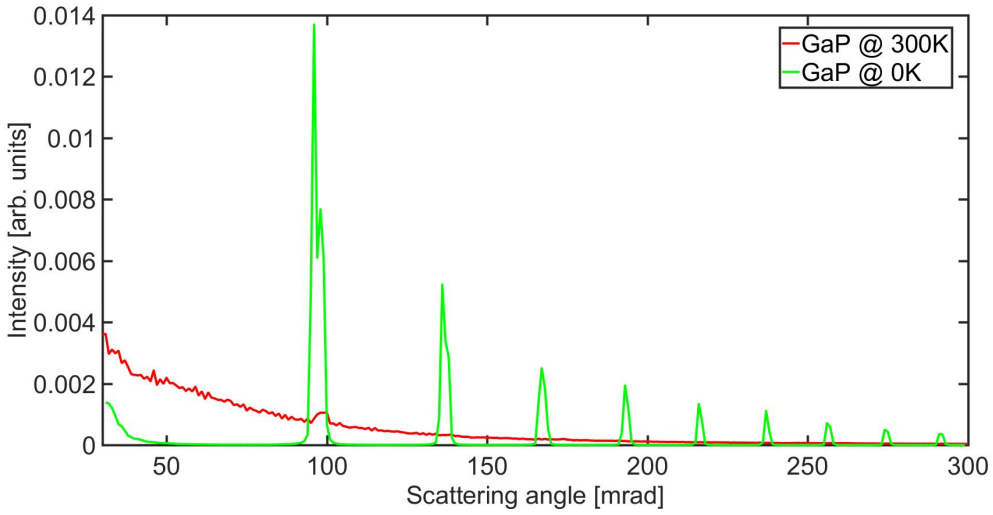

Figure 4.1: Scattered mean intensity of GaP unit cell changing with the detection angle at both 0 K and 300 K to show the influences of thermal atomic vibration.

The researched materials (GaP and GaAs) introduced in section 2.3 are chosen to execute the simulation. In total, 15 different atomic configurations of the simulated bulk materials are generated. In each configuration of the supercell, the positions of all atoms are changed with a displacement (Gaussian distribution) caused by the thermal vibration, which is sensitive to the temperature and is determined by Debye-Waller factor. For each configuration, the result obtained from the simulation is a 3-dimensional matrix in x, y and z coordinates with x and y representing the image coordinates and z indicating the thickness of the sample along electron beam direction. Therefore, the results are in total 15 different 3-dimensional matrices corresponding to the 15 configurations. For a fixed configuration number from 1 to 14, we randomly choose 15 different combinations of matrices for each number of configurations and then an averaged matrix is calculated for each combination of configurations. Obviously, the larger the configuration number, the smaller the discrepances between averaged results of different combinations and vice versa. For example, if 7 or 8 configurations out of 15 configurations are chosen, as many as 6435 different combinations are available. If only 1 configuration is selected, then each configuration is a 'combination of different configurations' used for the calculation and there are in total only 15 choices. To make the comparison fair between different configuration numbers, 15 possible combinations of different configurations are chosen to show how the number of configurations influence the averaged result.

For the averaged 3-dimensional matrix of chosen combinations, first group III and group V peak positions are separated from each other for images in x and y coordinates and

next the peak intensities are calculated for both group III and group V atomic columns with different thicknesses. The image evaluation method will be explained in detail in section 5.2.2. Peak intensities for both group III and group V atomic columns at certain thicknesses (10 nm, 20 nm, 30 nm, 40 nm and 50 nm) determined from averaged matrices are plotted to show the absolute image intensity distribution changing with the number of averaged configurations, as shown in figure 4.2 (a) for group III atoms and in figure 4.3 (a) for group V atoms. Obviously, image intensities increase with the increasing sample thickness. The intenstiy distribution also covers a larger range for thicker samples, especially when the number of averaged configurations is smaller. The image intensity distribution tends to converge at a certain point with increasing number of averaged configurations for each sample thickness.

To better reveal the results, the relative intensity distribution at each thickness are plotted against the number of chosen configurations for both Ga (group III atoms) and P (group V atoms) as shown in figure 4.2 (b)-(f) and in figure 4.3 (b)-(f). To realize the aim, first 15 configurations are averaged as the final result. Then the averaged matrix of chosen combinations of different lattice configurations are normalized to the final result at selected thicknesses. To compare the distribution of relative intensities changing with configuration numbers at different thickness, figures are plotted with the same scale. Althrough absolute intensities distribute in a larger range for thick samples than that for thin samples, relative intensities in fact is distributed in a smaller range for thick samples. Judged from the envelope functions of plotted graphs, 15 phonon configurations is still not large enough to get to a convergent point. However, for simulated samples with a thickness larger than 20 nm averaged from 14 different configuration, the relative difference is already smaller than 0.5% for group III (Ga) atom while the relative difference is even smaller for group V (P) atom. Therefore, 15 phonon configurations are considered enough to provide a realiable and reasonable result. The simulation of GaAs presents the same conclusion. Since the plotted curves are quite similar to these of GaP, they are not shown here.

In conclusion, a minimum of 15 different phonon configurations is already able to provide a trustable result for a multi slice simulation with frozen phonon approach. Considering the required extremely long computing time, larger number of phonon configurations is not applied in the current study, though it definitely gives more accurate results. In order to save the computing time, all simulations using STEMsim software use 15 different phonon configurations. However, only 10 phonon configurations are used for simulations carried out with STEMsalabim software [95]. Since STEMsalabim corrects the chromatic aberration by calculating a series of 7 defocus values and for each defocus value 10 new phonon configurations are generated, therefore, the result is even more accurate based on in total 70 different phonon configurations.

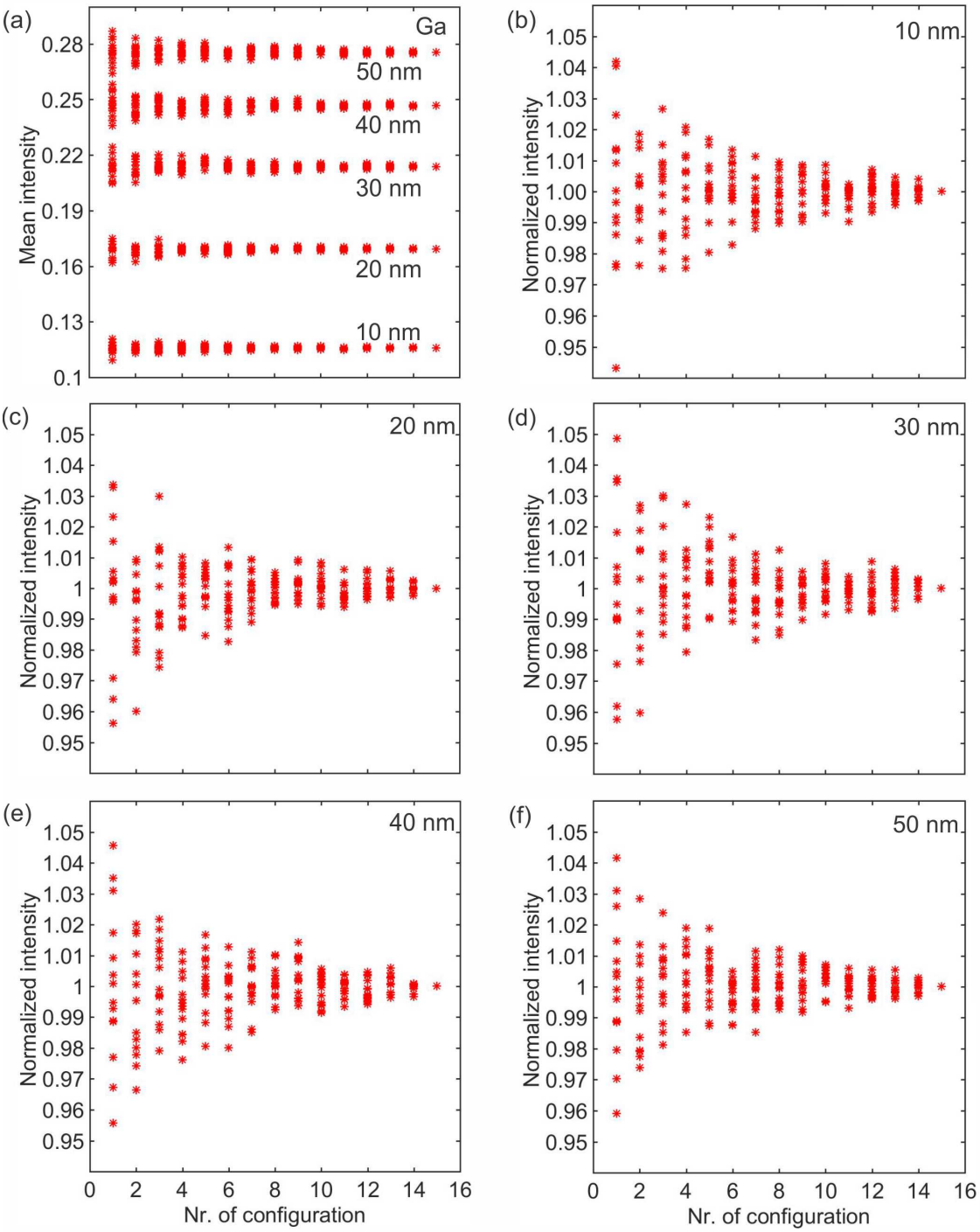

Figure 4.2: Simulated results showing how the number of applied configurations influences the image intensity for group III (Ga) atoms. (a) Overview of the absolute image intenstiy distribution changing with the number of configurations at different thicknesses. (b), (c), (d), (e) and (f) describe how the relative intensity difference changes with the number of configurations at a thickness of 10 nm, 20 nm, 30 nm, 40 nm and 50 nm, respectively.

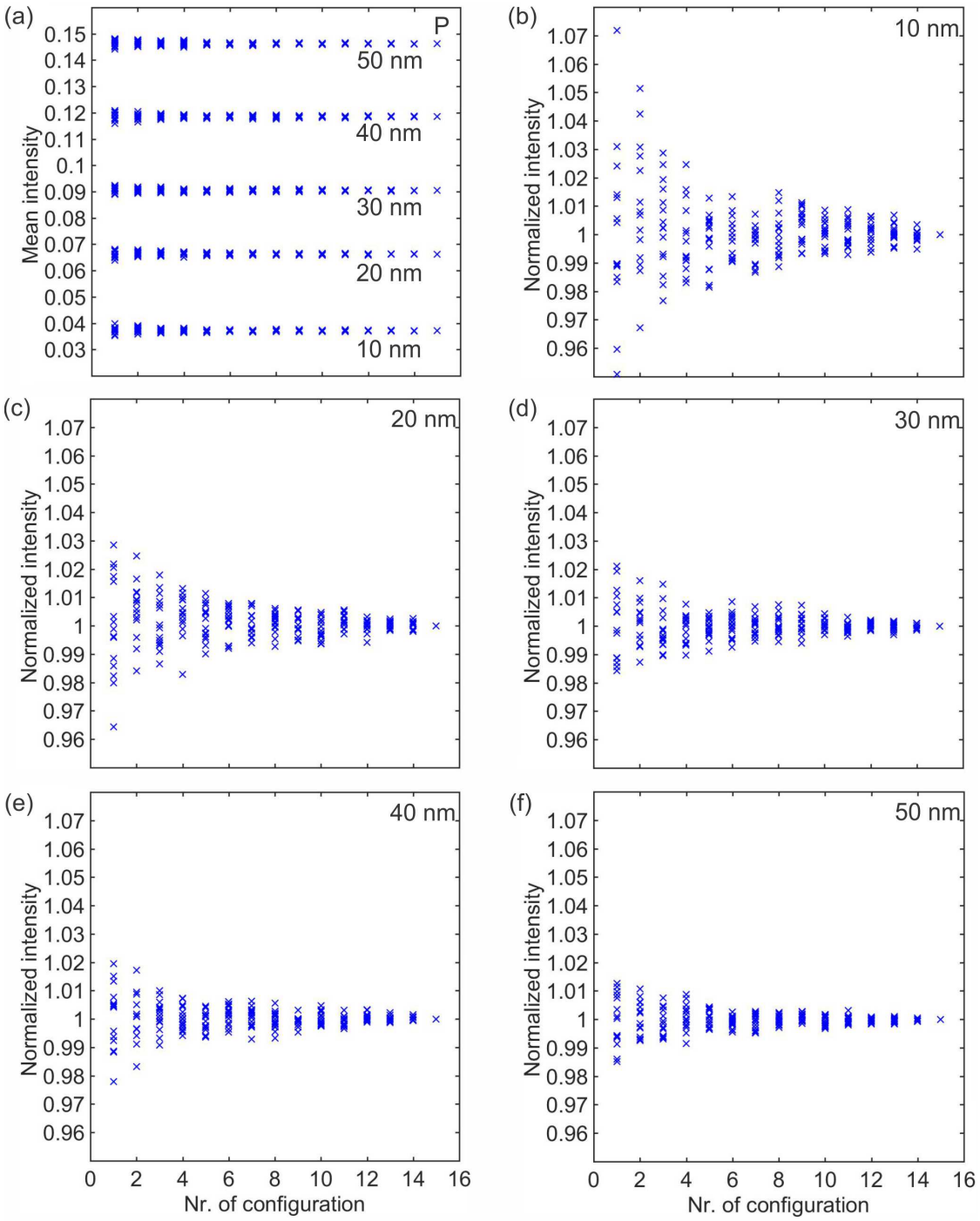

Figure 4.3: Simulated results showing how the number of applied configurations influences the image intensity for group V (P) atoms. (a) Overview of the absolute image intenstiy distribution changing with the number of configurations at different thicknesses. (b), (c), (d), (e) and (f) describe how the relative intensity difference changes with the number of configurations at a thickness of 10 nm, 20 nm, 30 nm, 40 nm and 50 nm, respectively.

4.2 GaAs simulation for sample thickness determination

In the present study, the used substrate and the barrier are GaAs. Also, every design in this study is based on GaAs. Since both the thickness and the composition of the ternary material can vary and hence influence the detected intensity, therefore, GaAs is chosen as the reference materials to determine the thickness of imaged regions. To fullfill the aim, a supercell of GaAs with a thickness up to 50 nm is generated as an input to the STEMsim simulation. To avoid the intensity loss caused by the beam broadening, the supercell is larger enough in x and y directions. The beam broadening is assumed to depend on the convergence angle and the TEM sample thickness and also elastic scattering. Take a 50 nm thick GaAs bulk material with the applied STEM settings (convergent angle: 24 mrad, acceleration voltage: 200 keV) in this study for example, using the equations introduced in section 2.2.2, the beam broadening b_1 caused by divergence effect is 2.4 nm and the beam broadening b_2 resulted from elastic scattering is 3.06 nm. Based on the quadrature relationship, the total beam broadening is 3.88 nm. So the supercell should be larger than 3.88 nm in both x and y directions.

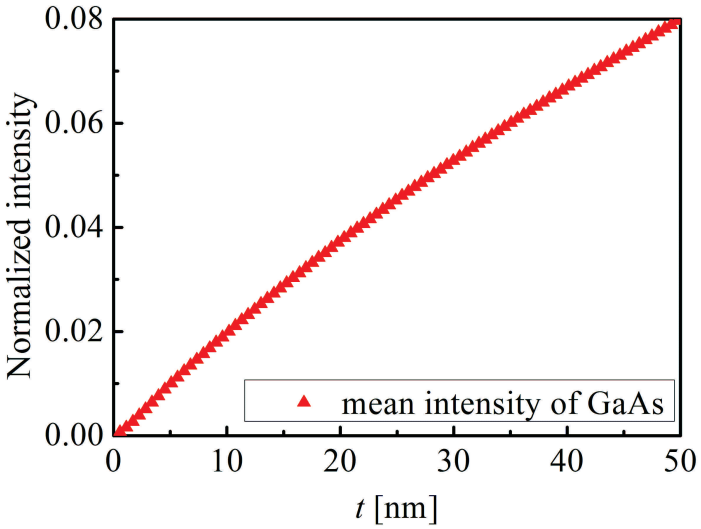

Figure 4.4: Normalized mean intensity I of one GaAs unit cell changing with the TEM sample thickness t [29].

The main parameters used for the simulation are listed in table 3.1. The thickness determination is based on the comparison between experimental and simulated images. If group III or group V peak intensities are made use of for comparison, the intensity distribution of the probe and the integrated radius should be carefully taken into account. To minimize such influences, the mean intensity of the whole unit cell of GaAs is chosen for comparison instead of group III or group V atom columns. Besides, the inner collection angle has to be accurately decided, since it can also significantly influence the determined intensity. The realiability of the method has already been confirmed by the EELS mea-

surement [110] . As shown in figure 4.4, the normalized mean intensity of one GaAs unit cell derived from the simulation is plotted against the TEM sample thickness. It is clear that the mean intensity increases almost linearly with the sample thickness, which agrees well with the experimental data. With this curve, the thickness of the TEM sample can be easily determined.

4.3 Image background intensity

The diffusely scattered background intensity distinguishes itself from the atomic column intensities. It is contributed by the average scattering from the sample by the de-channelled electron probe [31] and depends on the specimen thickness and is also a reflection of the average atomic number of the crystal [30]. Since background intensity equally contributes to the atomic columns, it should be subtracted from the original image to obtain the reasonable results. Otherwise, the image background intensity can strikingly influence the quantitative evaluation. The evaluation method is explained in detail in section 6.1.2.

To better understand the origin and influences of the image background intensity, simulations of GaAs, GaP and $(Ga_{0.5}In_{0.5})P$ have been chosen. $(Ga_{0.5}In_{0.5})P$ has almost the same lattice parameter as GaAs and is usually grown on GaAs to create a lattice-matched heterointerface. The applied parameters for $(Ga_{0.5}In_{0.5})P$ are listed in table 3.1 and the results of GaP and GaAs are already available in previous sections. The normalized intensity of both atomic columns (group III and group V) and image background changing with the TEM sample thickness are calculated and shown in figure 4.5 (a)-(b). The evaluation methods are presented in detail in in sections 5.2.2 and 6.1.2.

As expected, intensities of group III, group V and image background increase with the sample thickness. Due to the absorption effects, the slopes of the heavy atoms, such as Ga, As or In are greatly decreased with a thickness larger than 7 nm. An almost linear relationship exists for light atoms (P). Also, image background intensity increases approximately linearly for samples with a thickness larger than 10 nm. The image background intensities of all materials are much smaller as shown in figure 4.5 (b). GaAs has the highest image background intensity because of the largest average atomic number of GaAs (32). GaP has the smallest image background intensity, which is obviously apart from the image background of GaAs and $(Ga_{0.5}In_{0.5})P$. The image background intensity of $(Ga_{0.5}In_{0.5})P$ is relatively large compared with GaP and is only slightly lower than that of group V (P). Due to the large average atomic number, both the group V and the image background intensity of $(Ga_{0.5}In_{0.5})P$ are raised to a higher level compared to those of GaP. If the image background intensity is not properly subtracted, the quantitative evaluation can be severely influenced, especially at the interface, which will be dealed with in detail in Chapter 6.

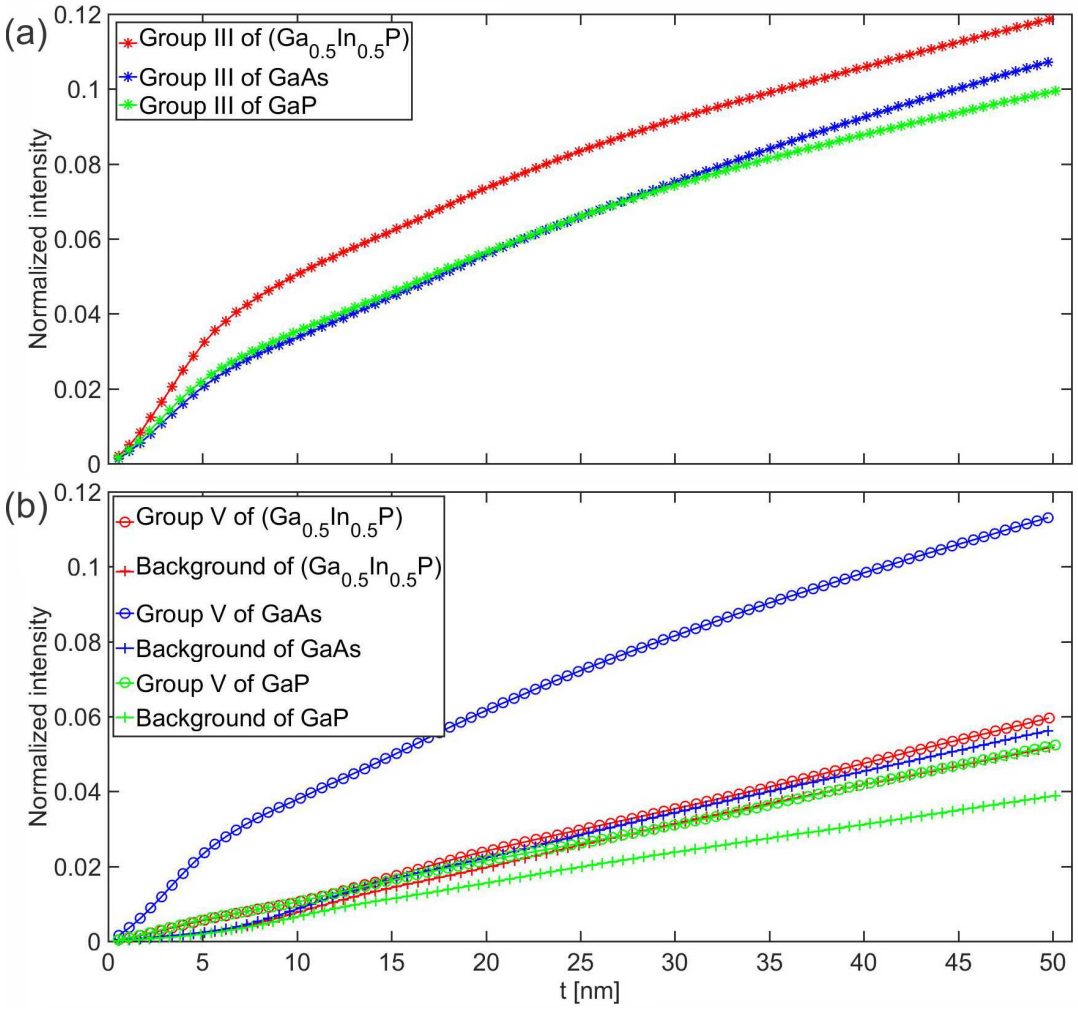

Figure 4.5: Normalized intensity I of (a) group III atomic column, (b) group V atomic column and image background changing with the TEM sample thickness t. The intensities of group V atomic columns and image background are plotted in the same figure for better comparison.

5 Quantitative evaluation of the interface of (GaIn)As grown on GaAs

This chapter presents the quantitative evaluation method applied in material systems with non-chemically sensitive backgrounds, like (GaIn)As/GaAs. This investigated materials have similar average atomic numbers across the interface for both sublattices, and the influences of background intensities from different regions on sublattice inensities can be negelected. Therefore, this kind of materials is considered to have non-chemically sensitive backgrounds. Similarily, if the average atomic numbers are significantly different for any sublattice on both sides of the interface , like (GaIn)P/GaAs, background intensities from different sides of the interface can strikingly affect the sublattice intensities. Hence, this kind of mateials is assumed to have chemically sensitive backgrounds. Section 5.1 deals with the quantitative evaluation of HAADF STEM images (Q-method) and the related characterization of both the QW chemical homogeneity and the interface roughness. In section 5.2, the explained evaluation method is applied to the (GaIn)As/GaAs material systems grown under different conditions, to find out the influences of growth parameters on the QW homogeneity and interface roughness. In this section, the growth as well as its interruption takes place at the same temperature for every sample. If they occur at different temperatures for every sample, the influences of such complicated conditions on the QW properties are also investigated via (GaIn)As/GaAs system and the corresponding results are presented in section 5.3. Section 5.1 and section 5.2 are mainly based on the contents of the paper [29] and some results are recalculated with the application of some new methods.

5.1 Quantitative evaluation of HAADF images and interfaces

5.1.1 HAADF image analysis

To better carry out the quantitative evaluation of HAADF images, first we have to understand the image contrast and read the corresponding information from the image. Therefore, a brief analysis of the investigated micrograph in a view of [010] zone axis is given in figure 5.1. Obviously, every atomic column can be resolved from the high resolution HAADF STEM image. The image is composed of (GaIn)As on the left side, GaAs on the right side and the interface between them. A line profile of the averaged intensity of the whole image is overlaid on top of the image showing the intensity changes across the

interface. Based on the atomic column intensity, group III and group V columns can also be distinguished from each other and an overlay of the corresponding crystal structure is also shown in figure 5.1. The thickness difference in this field of view can be neglected and is in the range of around 1 nm, the intensity of the Z-contrast image is propertional to the average atomic number. The (GaIn)As region is hence brigher than the GaAs region owing to the heavy indium atoms.

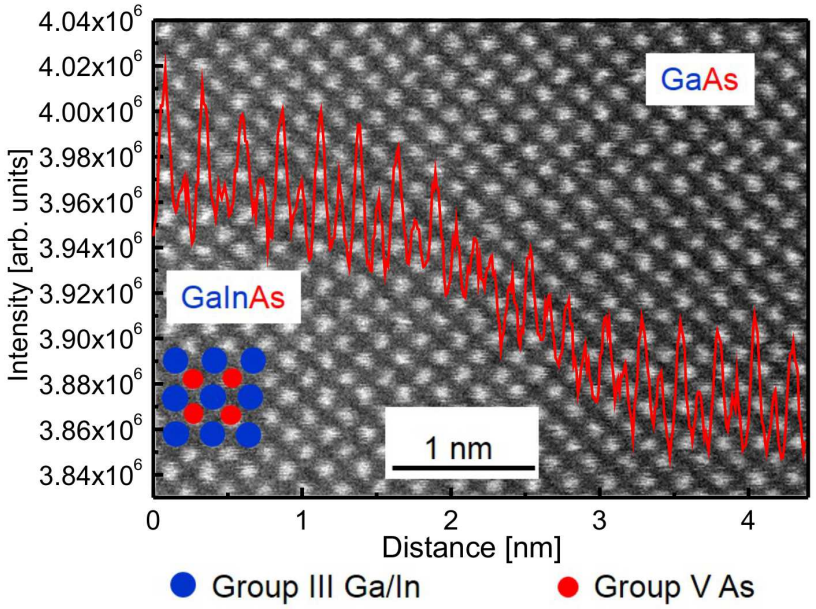

Figure 5.1: An examplary experimental HAADF STEM image of (GaIn)As/GaAs in [010] zone axis with the overlay of the schematic illustration of one Ga(In)As unit cell. The blue dots indicate the group III atomic columns, whereas the red dots denote the group V atomic columns. Group III atomic columns are brighter at (GaIn)As QW and darker at GaAs barrier compared to their neighboring group V atomic columns. The line profile of the average intensity of the whole image is shown overlaid to the image.

5.1.2 Quantitative evaluation of HAADF images (Q-method)

The quantitative evaluation of HAADF images, which is referred to as Q-method in this study, allows the interface and QW to be compared with each others quantitatively. To make the comparison between different images realiable, the evaluation process is carefully carried out for the investigated images. The image evaluation begins with the original HAADF image as shown in figure 5.2 (a). As explained in section 3.5.2, after the black level is subtracted from the original image, the intensity of the image is converted into current and then normalized to impinging beam as explained in section 3.5 (Figure 5.2 (b)). The normalized image is then analyzed using the Peak Pairs Analysis (PPA) software [111] to identify the atomic columns and determine their relative position in the image.

This procedure can also be done using the original image, because peak positions are not influenced during the image normalization. Using a home-written Matlab script the group III and group V sublattices are further separated from each other. Also the atomic column intensities are calculated through a circle integration around the peak position with a radius of $1/3^{rd}$ of the distance between the next nearest neighbors. Also, after the mean intensity of one unit cell in GaAs region is calculated, the sample thickness of this region can be determined by comparing with the simulation data. For the investigated images with a viewing area of around 10 nm x 10 nm, the thickness difference within the viewing field should be taken into consideraion during quantitative evaluation.

For the investigated material systems like (GaIn)As grown on GaAs, the group V sublattice is completely composed of by As without any chemical composition change across the interface. The determined intensity of group V sublattice is only determined by the local thickness without the influences of cross talk. Therefore, the intensity distribution of group V sublattice is a reflection of the sample thickness and can be made use of to correct the thickness gradient. Without thickness correction, the wedge shape of the sample can lead to great deviation to the quantitative results. The procedure of thickness correction is explained in detail in section 5.1.3. First the intensity gradient (thickness) information of the investigated region is fitted with a 3-dimensional surface function. Second this function is used to compensate the thickness gradient of the region to get a 'flat' TEM sample. After thickness compensation, the thickness fluctuation of the region is mainly a result of the surface roughness produced during the sample preparation.

In respect of group III sublattice, it is not chemically homogeneous across the interface. The In composition changes across the interface from (GaIn)As QW to GaAs barrier. In order to determine the In composition at every atomic column in the QW, a reference regions with at least 300 atomic columns for Ga is carefully selected and the mean intensity of every atomic column is calculated and denoted as I_{Ga}. Similarly, a large region with more than 1200 atomic columns for GaIn is chosen and the mean intensity is denoted as I_{GaIn}. Theoretically, the selected reference region should be as large as possible to provide a statistically realiable data. After thickness correction, the intensity of every group III atomic column scales to the average atomic number. The individual In composition x at every atomic column can be determined according to the following expression:

$$x = \frac{c_{In}(I_{exp} - I_{Ga})}{I_{GaIn} - I_{Ga}} \tag{5.1}$$

where c_{In} is the average Indium concentration of the (GaIn)As QW, determined using HR-XRD. I_{exp} is normalized image intensity of every atomic column after thickness compensation. With a Matlab script the Indium composition of every atomic column can be calculated according to equation 5.1 and plotted as a composition map shwoing the Indium concentration distribution at every local atomic column of the HAADF image

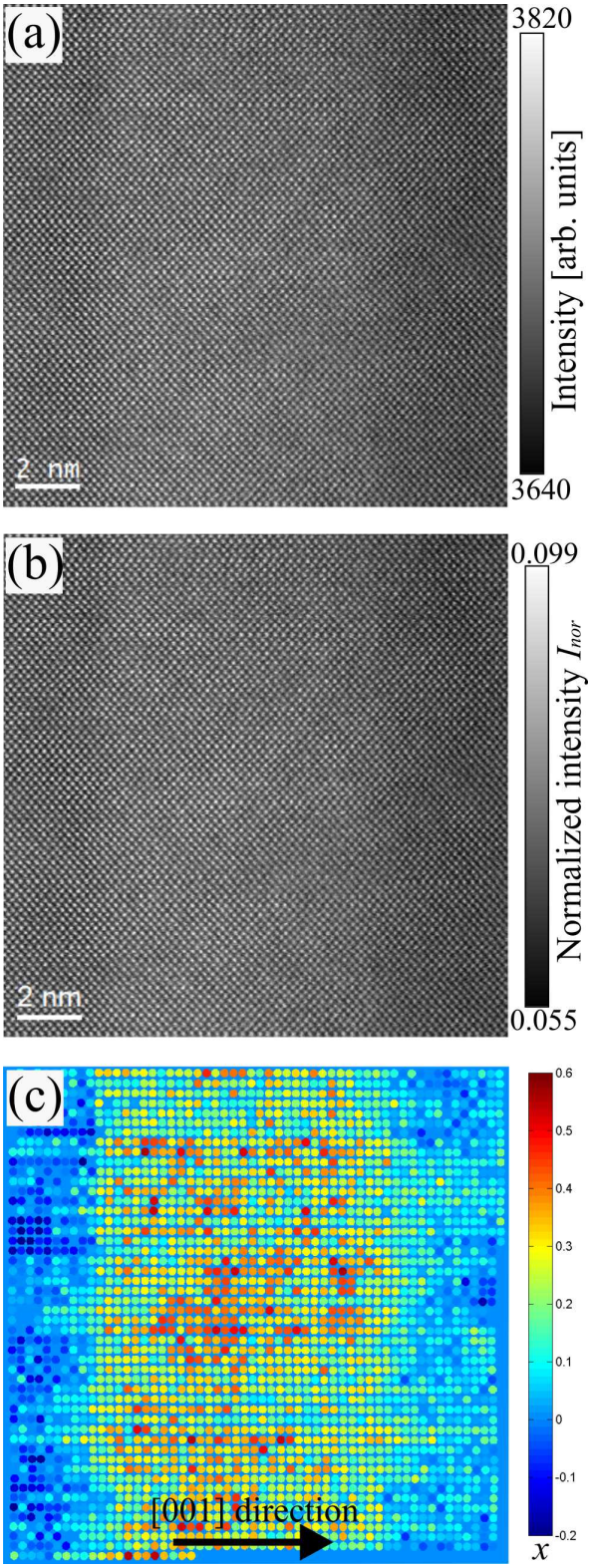

Figure 5.2: Evaluation process of the experimental images: (a) the original HAADF STEM image scaled with the absolute counts of the detector, (b) the analyzed image after background subtraction and normalized to the impinging beam, (c) Indium composition x map of the group III sublattice. In (b) the grey scale indicates the normalized intensity I_{norm}. In (c) the color bar means the In composition x in every atomic column.

(Figure 5.2 (c)). Since a linear relationship is assumed to exist between the In concentration and the measured normalized intensity according to equation 5.1, the chemical composition maps such as shown in Figure 5.2 (c) is only an rough approximation. Van Aert et al.[24] has also assumed the linear change of the scattered intensity with the chemical composition, but Rosenauer et al. [24] and Martinez et al. [26] has proposed that a non-linear relationship could better agree with the experiment instead of the linear relationship. In the current study, the investigated interfacial characteristic features, such as interface width and interface abruptness, are not influenced by the linear assumption, taking into account that the In composition theorectically changes from 0 in the barrier to the averaged 28% in the QW, determined from HR-XRD measurement.

5.1.3 Thickness correction of the (S)TEM sample

The investigated (S)TEM samples usually possess a wedge shape, generated during the sample preparation. This thickness gradient can significantly influence the applied quantitative evaluation processes, since image intensities depend on both the sample thickness and the averaged atomic number (the chemical composition). To get a robust result, it is of great importance to correct the thickness gradient in a proper way. During the thickness correction, on one hand, the wedge shape should be corrected, on the other hand, the mean intensity of the original image should not be altered.

In this study, the thickness correction of images is explained in detail with an exemplary HAADF image as shown in figure 5.3. The original image is composed of one (GaIn)As QW sandwiched by two neighboring GaAs barriers. The profile of the averaged intensity of the whole image is plotted in red curve and overlaid on top of the original image (Figure 5.3 (a)). After the Indium-containing (GaIn)As region is removed, a 2-dimensional surface fitting is carried out to obtain the thickness gradient, based on the image intensity of only GaAs barriers. With this surface fitting function, the thickness gradient of (GaIn)As region can be extraplolated. Then the thickness gradient map of the whole image can be plotted as shown in figure 5.3 (b). To correct the thickness gradient, the intensities of the original HAADF image (Figure 5.3 (a)) are divided by the thickness gradient values obtained at corresponding positions from the gradient map (Figure 5.3 (b)). A new image is generated as shown in figure 5.3 (c). According to the plotted profile of the average intensity of this new image, the thickness gradient of the image is significantly minimized. However, the intensity level of the image (Figure 5.3 (c)) is changed, as can be confirmed by the given scale bar. To maintain the original image intensity, this image (Figure 5.3 (c)) is multiplied by the mean thickness gradient of figure 5.3 (b). Then another new image is obtained as shwon in figure 5.3 (d). Obviously, the thickness gradient is minimized and the mean intensity is also unchanged for this image. After thickness correction, the newly obtained image can be applied further with the explained Q-method in section 5.2.2.

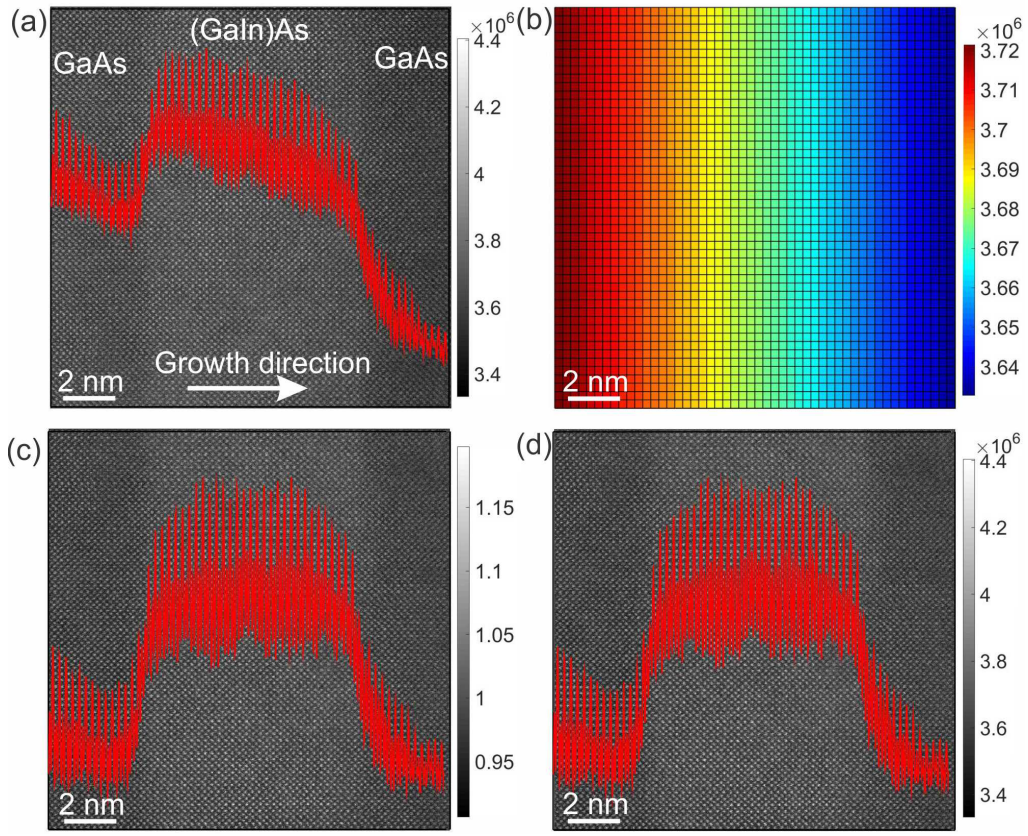

Figure 5.3: (a) Original HAADF image of the investigated QW with atomic resolution. The image is composed of one (GaIn)As QW sandwiched by two neighboring GaAs barriers. The growth direction is marked by the arrow. The overlaid profile of the average intensity of the whole image clearly shows the local thickness gradient. (b) The thickness gradient map is derived from GaAs barriers in the original image (a) and has the same size as the original image. (c) Thickness gradient is corrected through dividing the original image (a) by the thickness gradient map (b). The overlaid mean intensity profile of the whole image presents the corrected thickness. (d) The intensity of the corrected image is brought back to the original level. Detailed explanation is given in the text.

5.1.4 Influences of other factors on Q-method

It is worth pointing out that the mentioned Q-method works for the same sample thickness, electron probe size and the chosen crystal zone axis without the influences of cross talk between group III and group V atomic columns. The cross talk as explained in section 2.2.2 destroys the relationship between the chemical composition and the intensity and therefore makes the whole evaluation process impossible. In the present case, the existence of cross talk can be detected by intensity maps of group V (As) atomic columns. Theoretically, intensities of As atomic columns only depend on the sample thickness for the (GaIn)As/GaAs material systems. However, the detected intensities of group V atomic columns in the QW can be strengthened by the cross scattering from heavy neighboring group III atomic columns (a mixture of gallium and indium atoms), especially for the thick TEM samples.

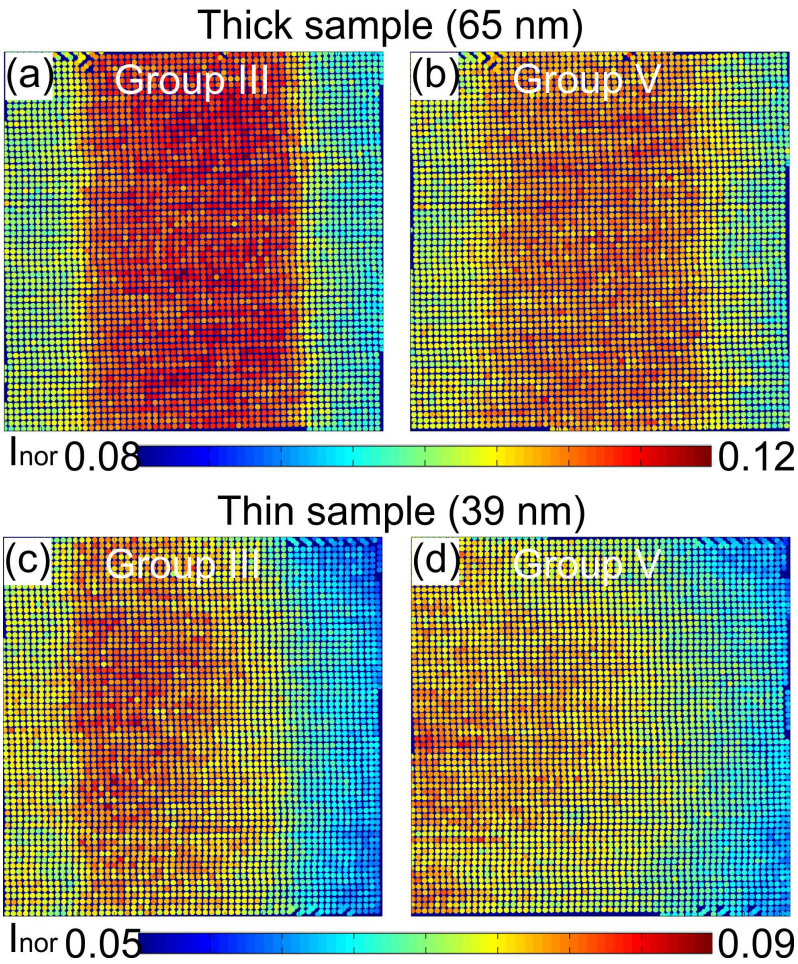

Figure 5.4: Normalized intensity (I_{norm}) map of both thick ((a) group III and (b) group V atomic columns) and thin specimen regions ((c) group III and (d) group V atomic columns) with atomic resolution. Due to the wedge shape the intensity decreases from the left side to the right side. The higher intensity in the middle of the maps indicates either the existence of (GaIn)As QWs for (a) and (c) or cross talk for (b). It is obvious that no cross talk happens in thin specimen regions as shown in (d).

An example is given in figure 5.4 to show the influences of cross talk on the sublattice intensities. Two samples with different thicknesses are chosen and the corresponding normalized intensity maps of both group III and group V are plotted without thickness correction. Figure 5.4 (a) and (b) are the intensity maps of group III and group V atomic columns of a thick TEM sample (around 65 nm), respectively. From figure 5.4 (a), the position of the (GaIn)As QW is revealed by the higher intensities of Ga/In atomic columns. In figure 5.4 (b), the intensities of group V atomic columns should be a reflect of the thickness of the investigated region. However, the position of (GaIn)As QW is still visible owing to the cross scattering from group III atom columns, which has redistributed the original intensities. Since the cross scattering mainly depends on the sample thickness and the averaged atomic number, this effect can be neglected for thin samples. The intensity maps of group III and group V atomic columns of a thin TEM

sample (around 39 nm) are shown in figure 5.4 (c) and (d), respectively. As expected, the position of (GaIn)As QW can be observed from figure 5.4 (c) and a thickness gradient of the sample is presented in figure 5.4 (d). Therefore, to carry out Q-method, we should carefully select the investigated regions to minimize the cross talk effects.

After the quantitative evaluation of images taken from carefully chosen thin regions, the QW and the corresponding interface can be revealed due to different indium compositions at the barrier and the QW. Because the strain relaxation [112] can greatly change the sample geometry of regions around the interface and also the corresponding intensities, the comparison between different TEM samples makes sense, only if they have identical or similar thicknesses. Otherwise, the plastic relaxation of thin TEM samples [109], [113] could introduce differences in shape chagnes. In addition, strain relaxation can significantly influence the characterization of interface abruptness. Hence, the corresponding simulation should be executed to help understand the interfacial features.

Besides, since the HAADF image is a two- dimensional projection of a three-dimensional (S)TEM sample. The projection of different interface structures along the beam direction can also make the comparison difficult, if the chosen (S)TEM samples have different thicknesses. For instance, a structured interface could have an intermixing two-dimensional projection (HAADF image), since the interface features could be smeared out for especially thick (S)TEM samples. In addition, the quantitative comparison between different samples is mainly based on statistics. Therefore, the calculated image regions should also have similar field of views, besides the similar thicknesses of (S)TEM samples, to make statistical results from different images comparable.

Additionally, the sample can be misaligned from the targeted zone axis orientation without notice in (S)TEM experiment. This tilting angle of the zone axis can alter the geometry between the incident beam and the specimen and further influence the HAADF imaging [114]. In fact, the tilt of zone axis can affect the channelling effect of the incident beam. Therefore, a reduction in intensity is expected. Special attention should be paid to materials with strained interfaces, since the zone axis can be slightly bent due to the strain relaxation [104]. Therefore, the zone axis orientation of the imaged region should be checked through the CBED pattern, every time when an image is acquired. If the strained QW is thin (only a few nanometers), the center of the QW should be properly aligned with the optical axis of the microscopy, to minimize the influences of tilt on HAADF imaging.

In summary, the selected HAADF images should be taken at thin regions of (S)TEM samples to avoid the cross talk. To make the comparison of statistical data obtained from different samples reliable and robust, the images should be taken at regions with similar thicknesses and they should also have similar field of views. In addition, the zone axis should be properly aligned with the help of CBED patterns.

5.1.5 Quantitative evaluation of the interface

Nowadays the semiconductor devices are mainly composed of different heterointerfaces. Therefore, it is quite important to optimize the growth parameters to get the desired interface. In this study, two different quantitative approaches have been applied to characterize the interface. To begin the introduction of these methods, a detailed look into the chemical composition map is presented to help to understand the data analysis.

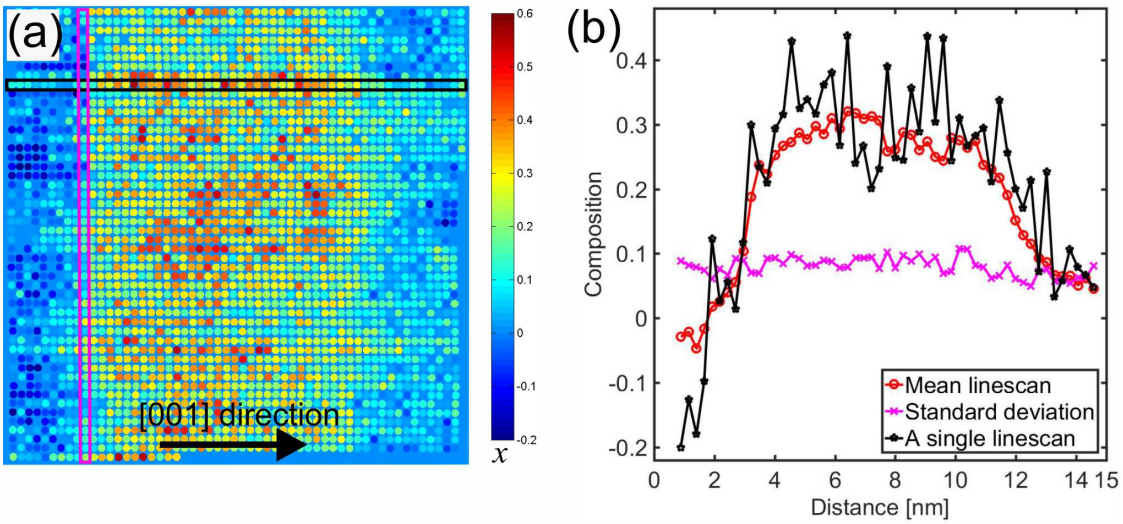

Figure 5.5: (a) Chemical composition map of indium across the (GaIn)As QW shown in 5.2 (c). The indium comcentration of every atomic column along the [001] growth direction chosen by the black box in (a) is plotted by a black line with pentagrams in (b). The atomic plane chosen by the magenta box is one (001) atomic plane perpendicular to the growth direction. The average In composition of every such (001) atomic plane along the growth direction is calculated and plotted by the red line with circles in (b). The standard deviation of the indium composition of every atomic column in the (001) atomic plane is calculated, and the standard deviation changing along the growth direction is plotted as shown in (b) by the magenta line and crosses.

The determined indium chemical composition map in figure 5.2 (c) is further made use of to give an exemplary explanation as shown in figure 5.5. In the map the [001] growth direction is marked by a black arrow. The (GaIn)As QW and the interface are perpendicular to the growth direction. The GaAs barriers next to (GaIn)As QW have no indium atoms, and the indium atoms only exist in the QW. The indium composition variation from the barrier to the QW and again to the barrier can reflect the evolvement of the interface. A black box in figure 5.5 (a) has selected one (100) atomic plane parallel to the growth direction. The corresponding indium composition of every atomic column is calculated and then plotted against atomic column positions as shown in figure 5.5 (b) by a black line with pentagrams. Such an operation to show property changes (like chemical composition) in a specific crystallographic plane is termed as a linescan in this study. Obviously, the interface feature can be revealed from such a linescan along the

growth direction. However, the discontinuity of the indium composition at neighboring atomic columns makes it difficult to evaluation the interface. As a result, such a linescan is carried out for every (100) atomic plane. In the end all linescans are averaged and the mean linescan is plotted by a red line with circles in figure 5.5 (b). The mean linescan looks more smooth and the interface can be better observed. A mean linescan is also referred to as a profile in this study. Alternatively, to draw the mean linescan (profile), every (001) atomic plane perpendicular to the growth direction is chosen, and then the mean indium composition of all atomic columns and the standard deviation of indium compositions among all atomic columns in (001) plane are calculated to plot the linescans of both indium compositions (red line with circles in figure 5.5 (b)) and standard deviation (magenta line with crosses in figure 5.5 (b)) across the QW. One (001) atomic plane is selected by the magenta box in figure 5.5 (a) and it only provides one data point for both profiles at the corresponding postion.

After linescans of the mean chemical compositon and the standard deviation are plotted, the quantitative evalution of the interface can be started. The most interesting feature of the interface is the abruptness and an abrupt interface is desired for most high performance devices. In this study, the abruptness of the interface is characterized with two approaches explained as follows.

One is the 90/10 evaluation approach, which defines the interface width as the number of atomic layers, whose chemical composition are between 10 % and 90 % of the bulk region. Obviously, the wider the interface is, the more intermixing (rough) the interface is. This approach is easy to carry out and the result is straightforward. However the accurcy of the method is limited to ± 1 group III/V atomic layer, since the linescan is based on the chemical composition map of either group III or group V atomic layers.

Error function fitting method is the other approach applied for interface characterization. With this method, the abruptness of the interface is evaluated by fitting an error function to its composition profile. The fitting error function is expressed as follows:

$$y = A + B \cdot erf(K \cdot (x - C)) \tag{5.2}$$

where the error function is defined as

$$erf(x) = \frac{2}{\sqrt{\pi}} \int_0^x e^{-t^2} dt \tag{5.3}$$

where K is the parameter to describe the abruptness of the interface. The larger K indicates an abrupt interface. The parameter C determines the position of the interface. A can shift the error function in y-direction whereas B compresses or stretches the error function in y direction. Since the abruptness of the interface is described by K, which is a continus real number, this approach is more accurate compared with the 90/10 evaluation

method. With the home-written Matlab script, the characterization is also easy to carry out. It is worth pointing out that K changes non-linearly with abruptness of the interface, which is determined by the error function itself (equation 5.3). For example, if the abruptness improves with the same quantity, K changes only slightly for an intermixing interface but increases significantly for an abrupt interface.

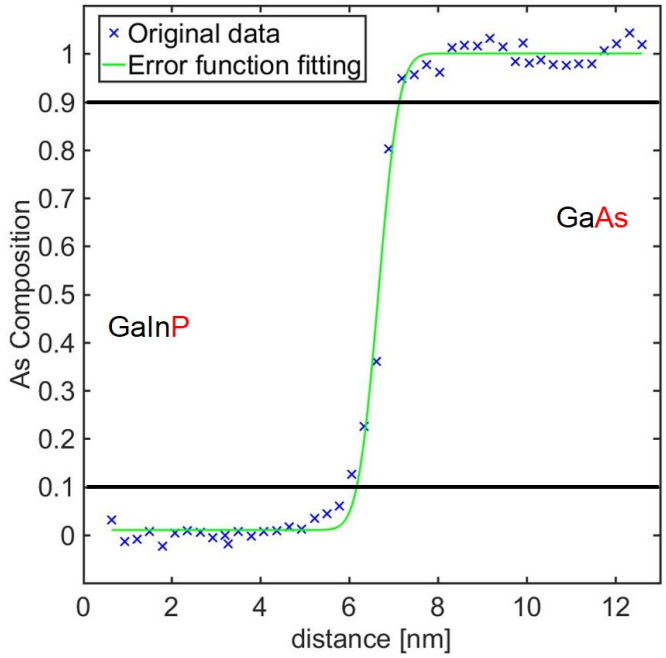

Figure 5.6: An examplary composition profile of As across the interface of (GaIn)P grown on GaAs. The original As composition of every (001) atomic plane is plotted by the blue cross. The fitted error function is plotted in green line. The black lines indicates the 90/10 evaluation method.

An examplary composition profile across the interface of (GaIn)P/GaAs material systems, instead of (GaIn)As/GaAs material systems investigated in this chapter, is chosen to explain the two approaches, because the chemical composition difference of group V atomic columns across the interface of (GaIn)P/GaAs is larger than that of (GaIn)As/GaAs. The arsenic composition profile of group V sublattices across the interface is plotted in figure 5.6. The arsenic composition is 0 % on the left side in (GaIn)P region and 100 % on the right side in GaAs region. The blue cross denotes the mean arsenic composition of every atomic plane along the growth direction. The black lines mark the position of 10 % and 90 % of the arsenic composition of the bulk GaAs region. The interface width can be determined by counting the number of atomic layers between two lines. It is clear that the interface has a width of 4 group V atomic layers. The green line is a fitted error function, which agrees well with the original data points. After the profile is fitted with equation 5.2, all four parameters are available. The obtained K is an indicater of the abruptness of the interface and can be applied to compare different interfaces. C determines the

position of the interface and is usually used to calculate the distance between group III and group V interfaces.

With the above two approaches, different interfaces can be quantitatively evaluated and compared with each other. Their application will be given in detail in following sections.

5.1.6 Quantitative evaluation of the chemical homogeneity of the QW

Besides the interface, the chemical homogeneity of the QW can also greatly influence the device performances. For binary materials, there is no such concern. For ternary or quarternary materials, a homogeneous chemical distribution is desired to realize the high device performances. The chemical homogeneity of the QW can be described by the standard deviation (σ) of chemical compositions of every atomic column at the QW. If all atomic columns have the same chemical composition, the theoretical standard deviation at the QW should be 0. Otherwise the larger the standard deviation, the more heterogeneous the chemical distribution at the QW.

The standard deviation of a QW is mainly determined by the chemical distribution. In addition, it is also significantly influenced by the surface roughness, the measurement error and the sample thickness. Mathematically, the total standard deviation (σ_{total}) of a QW can be expressed as:

$$\sigma_{total} = \sqrt{(\sigma_{com})^2 + (\sigma_{rou})^2 + (\sigma_{mea})^2 + ...} \tag{5.4}$$

where σ_{total} can be directly obtained through the calculation of the standard deviation of every atomic column in the QW. σ_{com}, $\sigma_{rou}$and σ_{mea} denote the standard deviation contributed by the composition distribution, the surface roughness and the measurement error, respectively. σ_{rou} and σ_{mea} can not be measured directly. However, their contributions can be estimated through the standard deviation of the barrier. Since there is no chemical composition fluctuation among different atomic columns for barriers, the standard deviation is mainly contributed by the surface roughness and the measurement error. Therefore, the standard deviation purely caused by the chemical composition can be obtained through subtracting the standard deviation of the barrier from the standard deviation of the QW. In addition, to make the comparison of standard deviations between different samples reliable, (S)TEM samples with similar thicknesses are chosen, and the influences of the (S)TEM thickness on the standard deviation can be neglected. It is worth noting that this statistical method is only valid when a larger number of atomic columns has been taken into account. In the present case, all applied samples consist of around 1000 atomic columns, to make the statistical method robust. Otherwise this method can lead to inaccuracy results.

Besides the chemical homogeneity of the QW, the profile of the standard deviation along the growth direction can also be applied as an indicator of the interface structure.

Within one HAADF image, the measurement error is on the same level and the (S)TEM sample has similar roughnesses and thicknesses. Under this condition, the total standard deviation of every atomic plane mainly depends on the interface structure and can be directly compared with each other. Also, additional errors caused by the standard deviation subtraction method can be avoided. The application will be explained in detail in following sections.

5.2 The influences of growth parameters on the QW and the interface

Material systems, like (GaIn)As/GaAs with different indium concentrations, have wide applications in modern optoelectronic devices. The device properties are strikingly influenced by the chemical distribution and the interface morphology. The interface morphology can be in a degree controlled by growth conditions, like the growth and growth interruption temperature, and the growth interruption time, applied at the interfaces.

5.2.1 Introduction to the investigated (GaIn)As/GaAs material systems

In this section, (GaIn)As/GaAs was chosen as a model system to investigate the internal interfaces of (GaIn)As grown on GaAs as well as GaAs grown on (GaIn)As. The investigated (GaIn)As QWs and GaAs barriers were grown on the (001) GaAs substrate using MOVPE under different growth conditions. The investigated (GaIn)As QWs, which are separated by GaAs barriers (approximately 70 nm wide), are around 9 nm wide. The average indium composition of the investigated (GaIn)As QWs is 28 %, determined by HR-XRD measurement and corresponding dynamical simulations. This method was also proved to be valid for (GaIn)N/GaN QWs [115]. The growth temperature and growth interuption time at the interfaces were varied to find out their influences. The deteiled growth information of all samples is given in table 5.1. The growth temperature and growth interruption temperature for both the bottom interface (BI), namely (GaIn)As grown on GaAs, and the top interface (TI), namely GaAs grown on (GaIn)As, are the same. The growth interruption times are different for the three samples as listed in the table.

Table 5.1: Detailed growth parameters for the investigated (GaIn)As/GaAs materials.

	Sample 1	Sample 2	Sample 3
Growth temperature [°C]	625	525	525
Interruption temperature [°C]	625	525	525
Interruption time at BI [s]	120	120	0
Interruption time at TI [s]	40	120	0

5.2.2 Image evaluation

HAADF images provide an overview of all QWs as shown in figure 5.7. Due to heavy indium atoms, (GaIn)As QWs present a bright contrast and are clearly revealed in the images. The growth direction is marked by the black arrow. However, because of the relatively low magnification of the overview image, the interface morphorlogy is not clear and hence can not be quantitatively compared with each other. Therefore, HAADF images with atomic resolution are needed to carry out the Q-method. For every sample, many images are taken at regions with different thicknesses. After image normalization,

the thickness of the image is determined by comparison with simulations. Then images of different samples with the same or similar thickness are chosen for further evaluation.

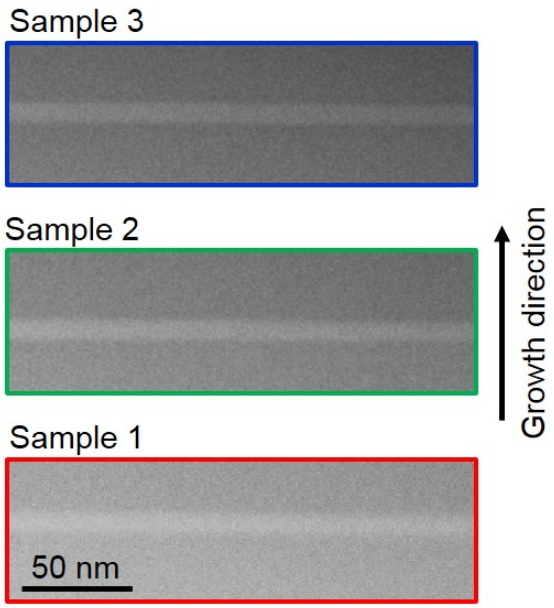

Figure 5.7: HAADF STEM overview images of the investigated samples. The growth direction is marked by the arrow on the right side. The indium-containing QWs can be revealed due to their bright contrast in respect to GaAs barriers.

Instead of original images, the indium composition maps of all samples are determined with Q-method and shown in figure 5.8. The mean thickness of the investigated region is marked above each indium composition map. All regions have a similar thickness of around 40 nm, with which thickness the cross talk effects can be negelected as confirmed in section 5.1.4. To make the statistical comparison between different images reliable, the evaluated total number of atomic columns of three samples is similar. Every dot in the composition map stands for one atomic column and its color indicates the indium composition of this atomic column. The indium composition is theoretically 0 at the GaAs barriers whereas it is higher at the QWs. It is clear that the indium composition at every atomic column in the QW is far from homogeneous. At some atomic columns the indium compositions can be twice as high as the mean indium composition of the QW, determined by HR-XRD. This implies the existence of possible compositional clustering of indium atoms. Besides, the QW (Sample 1) grown at higher temperature (625 °C) seems to present a more heterogeneous indium distribution than the other QWs (Sample 2 and sample 3) grown at lower temperature (525 °C). Also, a more intermixing interface can be observed in sample 1. Generally speaking, the bottom interfaces are more abrupt than the top interfaces for sample 2 and sample 3 grown at 525 °C.

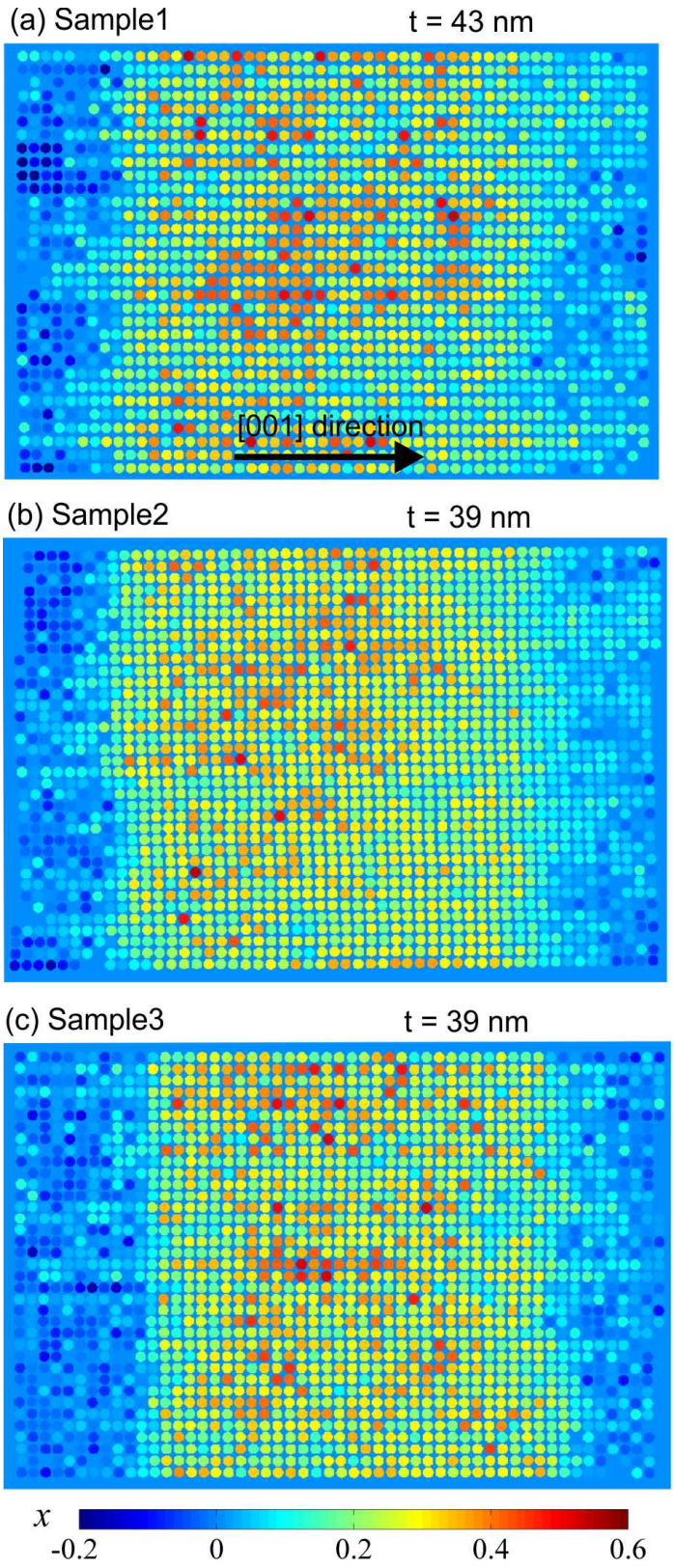

Figure 5.8: Indium composition x maps of (a) sample 1, (b) sample 2 and (c) sample 3. The thickness t of the investigated region in each (S)TEM sample is given above each map. All samples have the same growth direction, marked by the black arrow in (a). In each map the number of investigated atomic columns is similar.

5.2.3 Quantitative characterization of the QW and the interface

To carry out the quantitative evaluation of the QW and the related bottom and top interfaces, the mean line scan of the indium composition along [100] growth direction is carried out for all the composition maps and the corresponding profiles are plotted in figure 5.9. Sample 1, sample 2 and sample 3 are denoted by red square, green circle and blue pentagram, respectively. It is clear that the three samples have a similar indium composition distribution at QWs and the profiles present a similar shape. The bottom and top interfaces are marked by BI and TI as shown in the figure. Due to the memory effects of indium atoms, the indium compositions at the barriers near the top interface are slightly higher than that of the barriers near the bottom interface as shown in the figure.

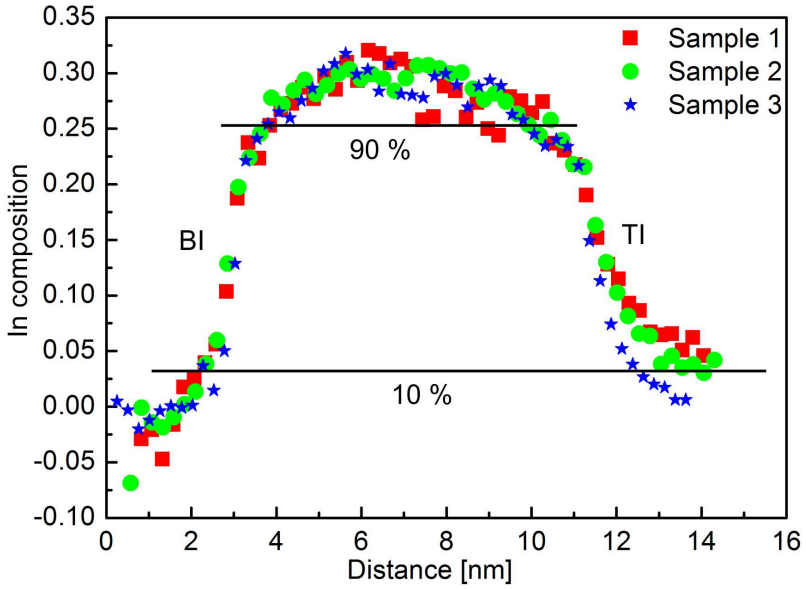

Figure 5.9: The indium composition profile of every (001) atomic plane, perpendicular to the growth direction, across the (GaIn)As QW for all investigated samples. BI and TI stand for the bottom and top interface, respectively. The black lines, with which the interface width is determined, mark the positions of 10 % and 90 % of the indium composition in the QWs.

The plateau region of the QW is made use of to determine the total standard deviation (σ_{total}) of the QW. The standard deviation of the barrier (σ_{bar}) is determined as the mean value of the three samples. Then the chemical homogeneity of the QW in every sample can be calculated through subtracting the standard deviation of the barrier from the total standard deviation of the QW. Both the original total standard deviation and the subtracted standard deviation of the QWS in differernt samples are shown in figure 5.10. After the subtraction, the standard deviation of the barrier is 0. The original and subtracted results have the same trends. The statistical data show that a high

growth temperature (625 °C) results in larger composition fluctuations (more heterogeneous chemical distribution) at the QW. Therefore, a lower growth temperature at 525 °C can benefit to obtain homogeneous chemical distribution compared with the high growth temperature. Besides, the growth interruption time can also significantly influence the homogeneity of the QW. Through the comparison between sample 2 and sample 3, an introduction of a growth interruption time of 120 s at 525 °C at both interfaces leads to a smaller standard deviation of the QW. A conclusion can be drawn that the growth interrruption can greatly improve the heterogeneous chemical distribution of the QW.

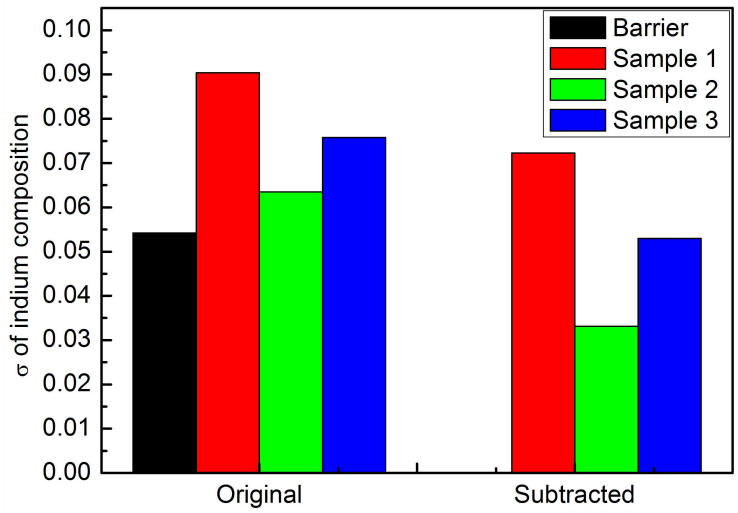

Figure 5.10: The original and subtracted standard deviation of both the QW and the barrier. The subtracted standard deviation of the QW is an indicator of the chemical homogeneity.

The interfaces of the QWs can be characterized with both approaches as explained in section 5.1.5. Using the 90/10 evaluation method, the interface widths can be determined by the black lines as shown in figure 5.9. The detailed results about the interface width are depicted in figure 5.11 to better compare the interface morphology. Even if the investigated three samples have different growth conditions, the bottom interfaces of them have the same width of 6 group III atomic layers. Compared with the bottom interfaces, all samples have a much wider top interface (13, 12, and 10 group III atomic layers for sample 1, sample 2, and sample 3, respectively). With the above information, the conclusion can only be drawn that the bottom interfaces are much abrupt compared to the top interfaces. Whether the bottom interfaces are abrupt or not, can not be determined yet. For the investigated (GaIn)As/GaAs material systems, the strain, generated by the lattice mismatch at the interface, can be relaxed after sample preparation. The strain relaxation can change the geometry of the thin (S)TEM samples and therefore influence the detected intensity distribution of HAADF imaging. So the observed wide interface can

also be caused by the strain relaxation. Hence, the conclusion of the interface abruptness can not be drawn without the support of the simulation.

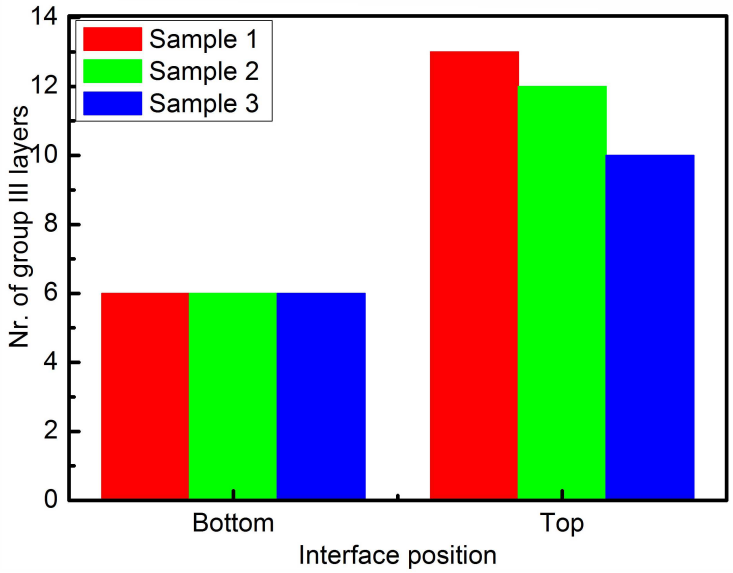

Figure 5.11: Interface width of both the bottom and top interfaces for different samples. The interface width is counted by the number of group III atomic layers using the 90/10 evaluation method.

To understand how the strain relaxation influences the interface, a supercell of GaAs-to-(GaIn)As interface is created as the input for the contrast simulation. In the (GaIn)As region of the supercell the indium composition is 28 % exactly the same as that in the experimental sampes. The thickness of the supercell is 40 nm, approximate to the thickness of the investigated samples. The supercell is inputted into the simulation after it is strain relaxed. It is worth noting that the atomic diffusion of indium atoms is not taken into account during the simulation. The profile of the indium composition of the simulated image along the the [001] direction is shown in figure 5.12. The profile shows the indium composition development across the interface. The GaAs barrier near the interface has a negativ indium composition due to the strain relaxation. The simulation shows that the abrupt interface under the influences of strain relaxation is 7 group III atomic layers wide.

A simple comparison between the simulation and experiment reveals the fact that bottom interfaces ((GaIn)As grown on GaAs) are abrupt for all samples in the current case and top interfaces (GaAs grown on (GaIn)As) are intermixing. This is probably caused by the memory effect of indium atoms. After the growth of (GaIn)As QW, there are still some indium atoms left in the chamber in MOVPE. These indium atoms can be incorporated into the first couple of monolayers of the GaAs barrier until they are used up. During this process, an island-like structure on the (GaIn)As top surface might be formed, which is then overgrown with GaAs upon barrier growth. At higher growth temperature

of 625 °C the top interface is slightly wider than that grown at lower temperature of 525 °C, indicating that larger segregation also happens at higher temperature.

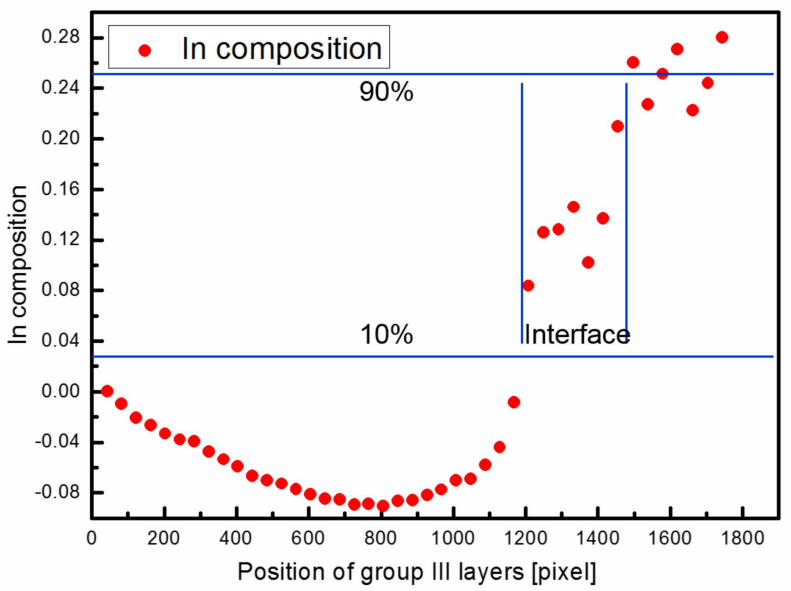

Figure 5.12: Simulation of a supercell (with a thickness of 40 nm), containing the interface between (GaIn)As and GaAs with an indium composition of 28 % on the (GaIn)As side. The profile of the indium composition in group III atomic layers along the [001] growth direction is plotted again the pixel. The 90/10 evaluation method is applied to determine the interface width of the interface.

From the indium composition maps (Figure 5.8), the three samples have similar interfacial features. The top interfaces grown at low temperature (525 °C) are slightly more abrupt. To better understand the interface morphology, the standard deviation of the indium composition of every [010]-oriented atomic column in the (001) atomic plane for both the bottom and top interfaces are shown in figure 5.13 for the three samples. The standard deviation of (001) atomic planes at the interface are mainly determined by the existence of different structures, such as island structure or indium-segregation. Therefore, the standard deviation at the interface can be used as a quantitative measure of interface structures, such as the distribution and size of islands and segregations. The standard deviations at the interface as shown in figure 5.13 reveals the following facts. Higher growth temperature (625 °C) leads to higher standard deviation (larger indium composition fluctuation) at both interfaces and also a more intermixing bottom interface. The growth interruption can significantly influence the internal interface morphology, especially the top interface. With an growth interruption of 120 s, the standard deviation of the top interface in sample 2 is greatly reduced, compared with other samples. The indium segregations on the surface of (GaIn)As is probabaly desorbed by the surface or the formation of the island structure smoothens the surface during the growth interruption.

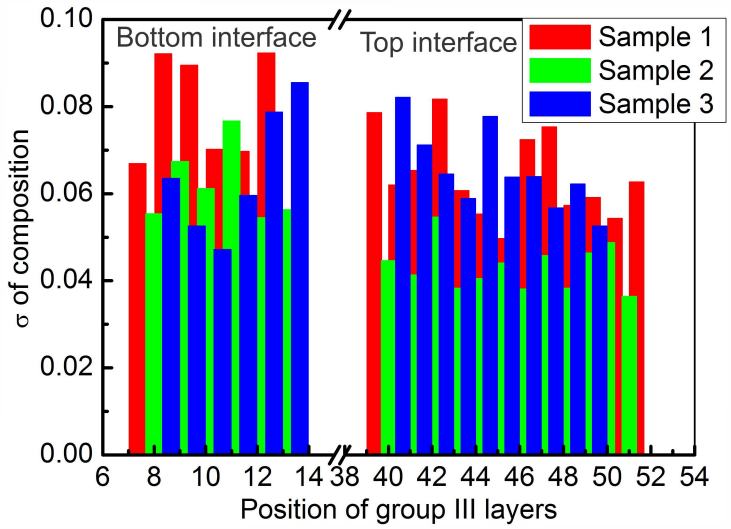

Figure 5.13: Total standard deviation of every (001) atomic plane perpendicular to the growth direction at both bottom and top interfaces for the three samples.

To better visualize the interface morphology, the evolvement of indium compositions at the interface region is plotted in three dimension as shown in figure 5.14. The nodes of the black lines represent the position of the [001]-oriented atomic positions. The x and y axes denote the relative position of atomic columns in the corresponding image. The height in z axis indicates the indium composition. Larger indium composition fluctuation in the (001) plane is reflected as a high standard deviation value in figure 5.13.

The error function fitting method is also applied to characterize the interface. As explained in section 5.1.5, a larger K factor indicates an abrupt interface and vice versa. The corresponding results are listed in table 5.2. The larger K factors of bottom interfaces point out an abrupt interface. Though bottom interfaces in three samples are of the same width, they have different K factors. It confirms that the accuracy of the error function fitting method is better than that of the 90/10 evaluation method. The small K factor of the bottom interface in sample 1 indicates a more intermixing interface compared with other samples, which is also supported by the standard deviation results. The K factors of top interfaces also agree well with interface width results. Basically speaking, two evaluation methods of the interface will present the same result.

Table 5.2: Determined K factors for the investigated internal interfaces with the error function fitting method.

	Sample 1	Sample 2	Sample 3
K (Bottom interface)	0.91	1.07	1.35
K (Top interface)	0.63	0.63	0.77

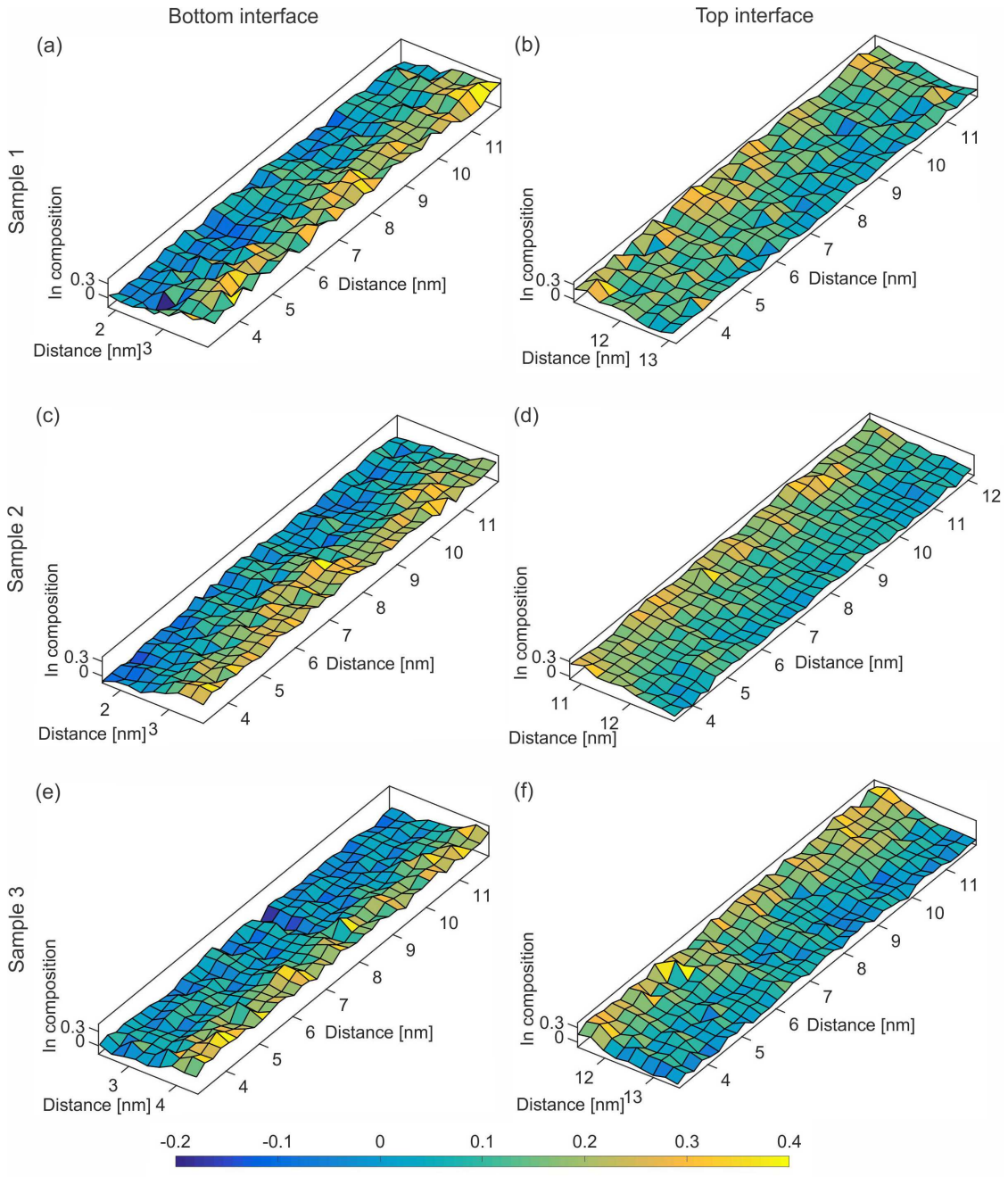

Figure 5.14: Indium compositions at the interfaces are plotted as the position in the corresponding images in three dimension to show the interface structures. The color bar indicates indium compositions at the interface.

5.3 The influences of growth and interruption at different temperatures

In section 5.2, the influences of growth conditions have already been discussed on both the interface morphology and the chemical homogeneity of the QW. The growth and growth interruption temperatures for samples investigated in section 5.2 are the same. However, the growth and growth interruption temperatures could also be varied to realize a better control of the interface morphology. It is necessary to find out the influences of growth and growth interruption at different temperatures on the interface morphology and chemical homogeneity of the QW. As presented in section 5.2 an abrupt bottom interface can be already achieved. Therefore, only the morphologies of top interfaces are discussed in this section. So the aim of this section is to investigate influences of growth and growth interruption at different temperatures on the top interface morphology and the chemical homogeneity of the QW.

5.3.1 Introduction to the growth conditions of (GaIn)As/GaAs

To realize the aim, the (GaIn)As/GaAs material system is again chosen as a model system. The growth of the samples takes place via MOVPE on (001) GaAs substrate. All samples share the same layer structure as shown in figure 5.15, with different growth conditions and indium concentrations. The (GaIn)As QW with a thickness of 4 nm is repeatedly grown four times and they are separated by the GaAs barrier with a thickness of 50 nm. Every time after the growth of (GaIn)As, a growth interruption of 40 s is introduced. After the growth of the last (GaIn)As QW, a AlAs layer with a thickness of 85 nm is grown. To avoid the oxidation of aluminium, a GaAs cap is introduced. As an etching layer, AlAs will be removed to reveal the top surface of (GaIn)As with AFM measurement.

The detailed growth parameters are listed in table 5.3. Clearly, the investigated four samples have the same growth interrruption time of 40 s. All possible combinations of the two temperatures (525 °C and 625 °C) are used for growth and interruption times. The growth and growth interruption temperatures are still the same for sample 4 and sample 7 whereas sampe 5 and sample 6 have different growth and growth interruption temperatures. After the sample growth is finished, HR-XRD measurement is carried out for the four samples. The determined average indium compositions of (GaIn)As QWs are also listed in the table. The indium concentrations in the QWs are lower compared to the former group samples, which makes it difficult to determine the position of the QWs from the HAADF images due to the low contrast.

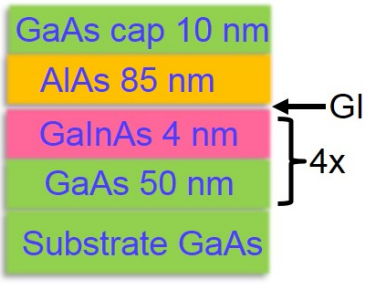

Figure 5.15: Schematic layer structure of the investigated samples. GI: growth interruption

Table 5.3: Detailed growth parameters for the investigated four samples

	Sample 4	Sample 5	Sample 6	Sample 7
Growth temperature [°C]	625	625	525	525
Interruption temperature [°C]	625	525	625	525
Interruption time [s]	40	40	40	40
In composition [%]	10.3	10.7	11.0	11.5

5.3.2 Overview of the top interface

After the AlAs layer is etched away, the surface morphology of (GaIn)As is revealed by the AFM measurement as shown in figure 5.16. The revealed surface of (GaIn)As QW, viewed along the [001] growth direction, is the top interfaces of (GaIn)As grown on GaAs, as investigated by HAADF images in section 5.2.

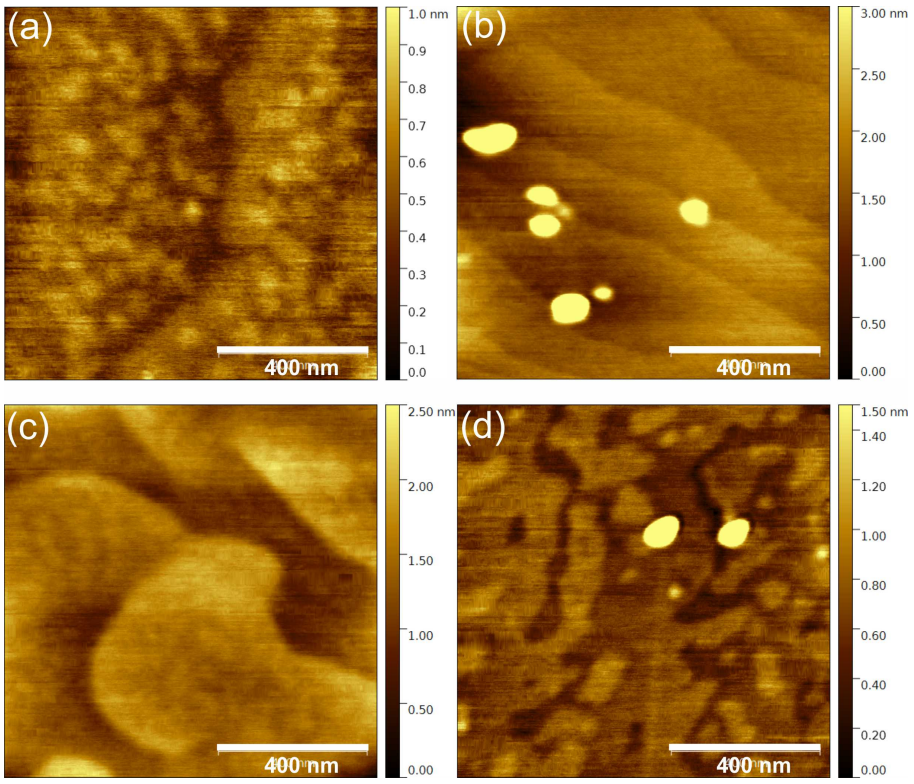

Figure 5.16: AFM images showing the surface morphology of (a) sample 4, (b) sample 5, (c) sample 6 and (d) sample 7. The bright spots in (b) and (d) are caused by the remaining parts of AlAs layer.

Obviously, some island structures are formed on top of (GaIn)As QW in sample 4 (Figure 5.16 (a)). The round islands have a diameter of around 100 nm and a height maximum of 1 nm. They are evenly distributed at the surface of (GaIn)As. Compared with sample 4, sample 6 as depicted in figure 5.16 (c) shows an improved surface but still with the existence of island structures. Sample 5 and sample 7 present quite a smooth

surface without the formation of islands, although some steps can be observed from the surface. The bright spots in figure 5.16 (b) and (d) are caused by the remaining parts of AlAs layer. Correlated with the growth conditions, it is obvious that growth and growth interruption at higher temperature of 625 °C lead to the formation of island structure in sample 4. If the sample is grown at 525 °C and growth interrupted at 625 °C, the island structure still exists as depicted in sample 6. On the other hand, the samples with a growth interruption temperature of 525 °C have a flat surface without forming any islands at the surface. The island formation seems to be determined by the applied growth interruption temperature.

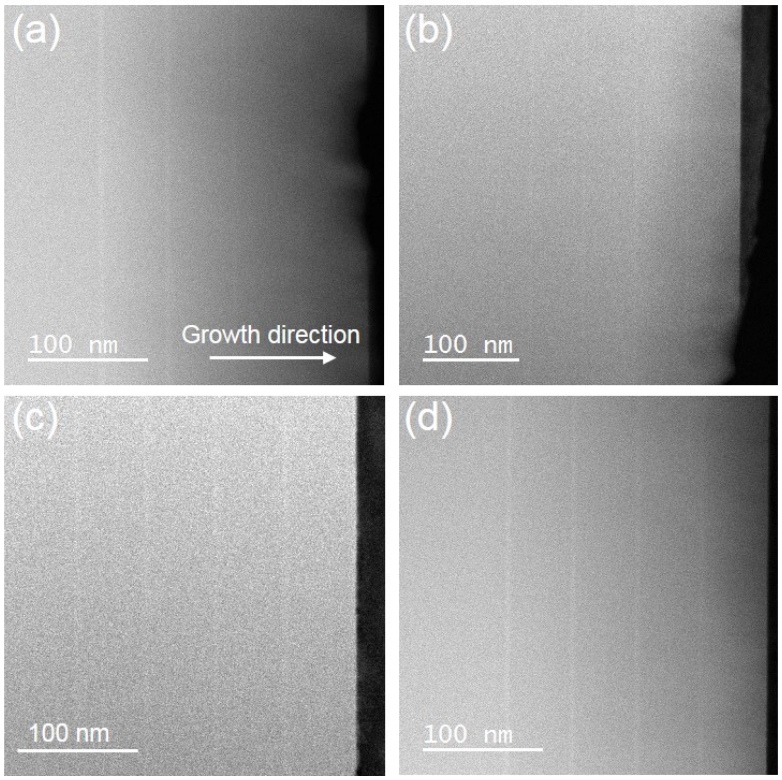

Figure 5.17: HAADF STEM overview images of (a) sample 4, (b) sample 5, (c) sample 6 and (d) sample 7. The growth direction is marked by the arrow in (a).

To confirm the influences of growth conditions, HAADF STEM images are taken to provide an overview for the four samples as shown in figure 5.17. The four samples have the same growth direction as marked by the arrow in figure 5.17 (a). The (GaIn)As QWs can be distinguished from the GaAs barriers with quite a low contrast, because of the low indium concentration. From the overview images, the (GaIn)As QWs in all samples look quite similar. The island structure can not be observed from the overview images due to the low resolution, since the island structure has a diameter of around 100 nm but with a height less than 1 nm. If HAADF images with atomic resolution are taken for the four samples, the edges of the island structure can be probably detected

in the growth direction. But it is still difficult to view one complete island due to the limited viewing field of HAADF images. Under this condition, the standard deviation of the chemical composition at the interface can be used as a quantitative measure of the interface structure, since the existence of island structures result in an increase in the standard deviation.

5.3.3 Quantitative evaluation of the QW and the interface

As a routine, HAADF images with atomic resolution are obatined for the four samples. After image normalization, the thickness of the imaged regions is determined via contrast simulations of GaAs as already explained in section 4.2. The images taken at regions with similar thicknesses are chosen and then further compared with each other via quantitative image evaluation. The Q-method as introduced in section 5.1 is applied to all images. After thickness correction, the indium composition is calculated and the indium composition map is plotted for all samples. Based on indium composition maps, the indium profiles of every (001) atomic plane across the (GaIn)As QWs as well as the corresponding standard deviation profiles for all samples are depicted in figure 5.18 and 5.19.

In addition, to find out the influences of the strain relaxation on HAADF imaging, a super cell containing (GaIn)As-to-GaAs interface is generated for the simulation (Simul 2). In order to simplify the computing work for simulation, only one contrast simulation is carried out, considering that all investigated regions have a thickness around 20 nm and the indium compositions in the QWs are also similar. The (GaIn)As part of the super cell has an mean indium composition of 11 %. The thickness of the super cell along the beam direction is 20 nm. After strain relaxation, the calculated HAADF image is shown in figure 5.20 (a). The same image evaluation process is carried out to the simulated image. The profile of the indium composition of every (001) atomic plane across the interface is plotted in figure 5.20 (b). The red shadow indicates the standard deviation of the indium composition of every atomic column in the (001) plane.

The interface abruptness and the chemical homogeneity of the QW for both experiment and simulation are evaluated with approaches introduced in section 5.1.5 and section 5.1.6, respectively. The detailed evaluation processes for experiment are not shown here any more. Instead, the acquired quantitative results for the four samples are summarized in table 5.4. With respect to simulation, the characterization of the interface with two methods is shown as an example in figure 5.20 (c) and the results are also presented in table 5.4. The analysis of the above results as well as the comparison between experiment and simulation will be discussed in the following sections in detail.

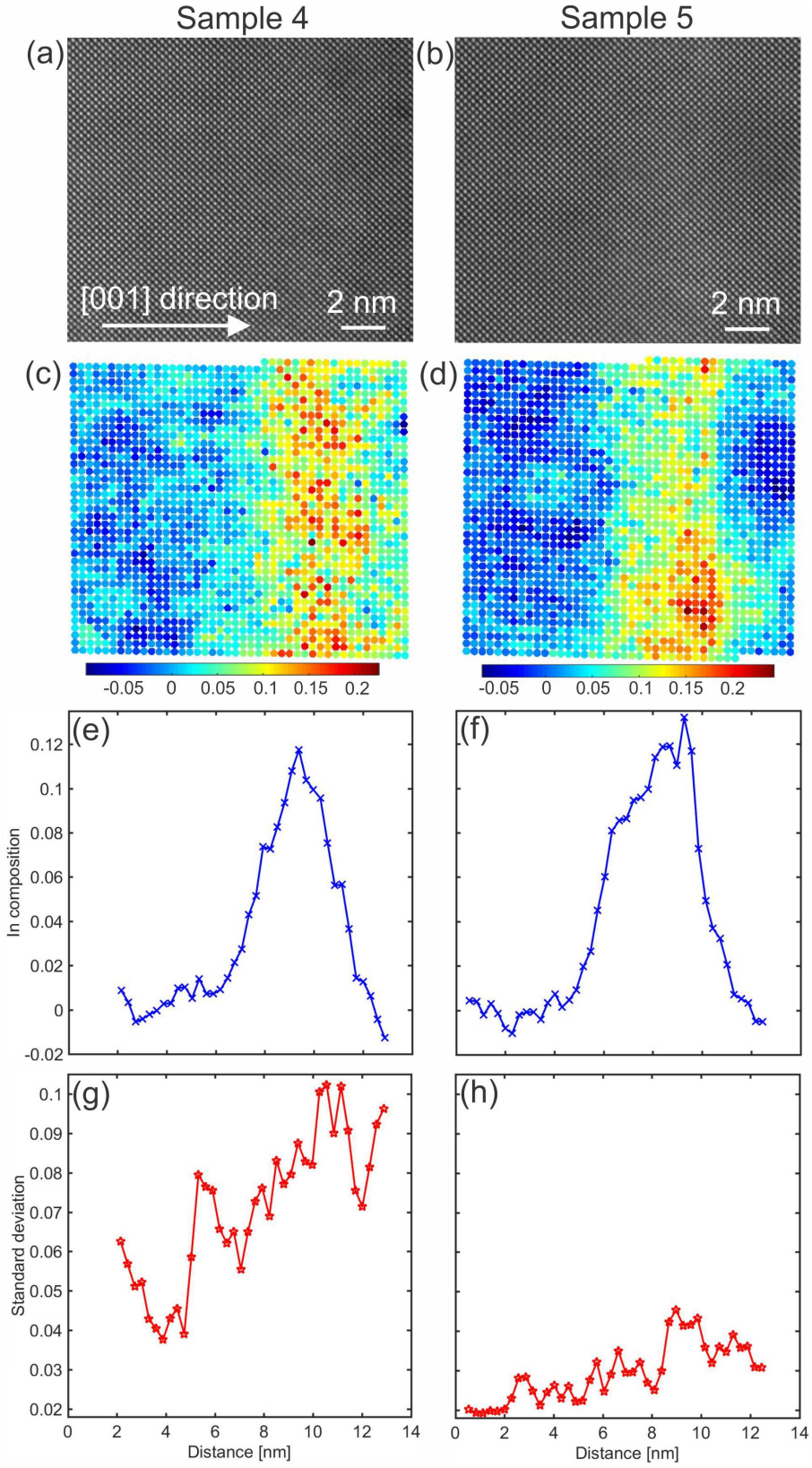

Figure 5.18: Original HAADF images of (a) sample 4 and (b) sample 5 as well as the indium composition maps of (c) sample 4 and (d) sample 5. The growth direction is marked by the arrow in (a). The average indium composition profiles of sample 4 and sample 5 along the growth direction are depicted in (e) and (f), respectively. The corresponding standard deviation profiles of sample 4 and sample 5 are plotted in (g) and (h), respectively.

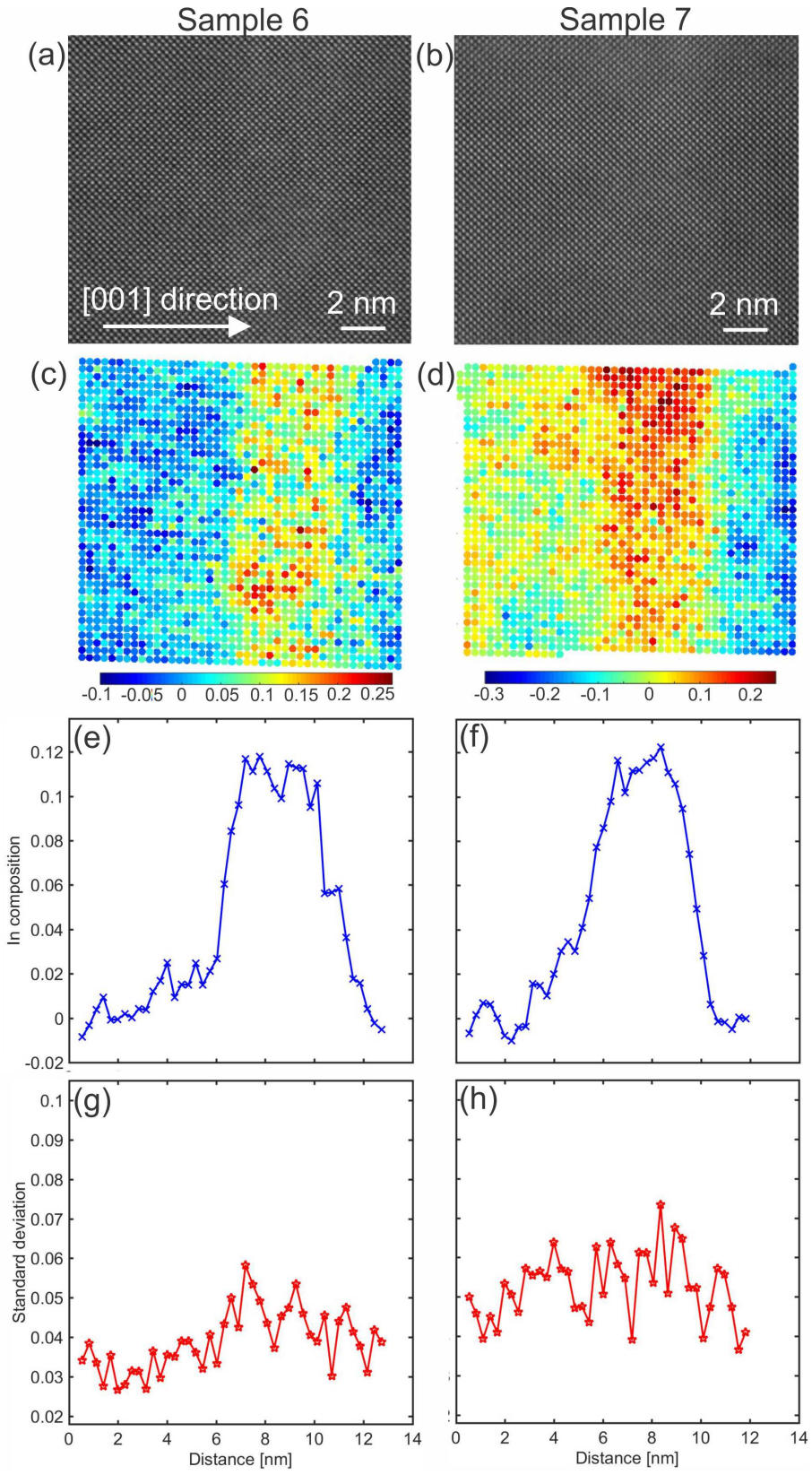

Figure 5.19: Original HAADF images of (a) sample 6 and (b) sample 7 as well as the indium composition maps of (c) sample 6 and (d) sample 7. The growth direction is marked by the arrow in (a). The average indium composition profiles of sample 6 and sample 7 along the growth direction are depicted in (e) and (f), respectively. The corresponding standard deviation profiles of sample 6 and sample 7 are plotted in (g) and (h), respectively.

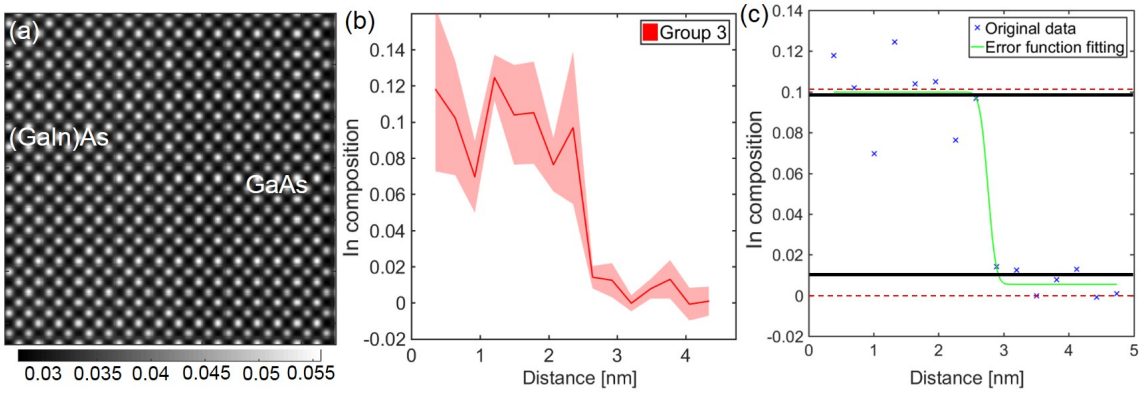

Figure 5.20: Simulation of (a) the (GaIn)As-to-GaAs interface. The profile of indium composition for group III atomic columns across the QW is plotted in (b) with the red shadow indicating the corresponding standard deviation of the indium composiiton of each atomic column in every (001) atomic plane. The 90/10 evaluation method and the error function fitting method are shown in (c).

Quantitative evaluation of the chemical homogeneity of the QW

As explained in section 5.1.6, the chemical homogeneity of the QW can be described by the stanard deviation. In this section, all chosen images have a thickness of around 20 nm as shown in table 5.4. Therefore, the influences of the thickness on the standard deviation for all samples should be similar. To determine the standard deviation caused by the chemical composition, the positions of both the QW and barrier are derived from the indium composition profiles, then the standard deviations of them are calculated from the corresponding standard deviation profiles. After that, the standard deviationy caused by the chemical distribution at the QWs are calculated through subtracting the standard deviation of the barrier from the standard deviation of the QW for all investigated samples. As expected, sample 4 with both growth and growth interruption at 625 °C have the largest standard deviation of 0.0849 whereas sample 7 with growth and growth interrupition at 525 °C shows the smallest standard deviation of 0.0331. For sample 5 with a standard deviation of 0.0356, grown at 625 °C and growth interrupted at 525 °C, and sample 6 with a standard deviation of 0.0345, grown at 525 °C and growth interrupted at 625 °C, the standard deviations are greatly reduced compared with sample 4 and are only slightly increased compared with sample 7. These facts point out that higher growth and growth interruption temperatures (625 °C) lead to higher standard deviation of chemical composition, and therefore a more heterogenerous chemical distribution. Besides this, either a growth or a growth interruption at lower temperature (525 °C) can make the chemical distribution much more homogeneous. The influence of either higher growth temperature or higher growth interruption temperature on the composition distribution is relatively small. These results are supported by the data in table 5.4.

Table 5.4: The summary of results from both experiment and simulation.

	Sample 4	Sample 5	Sample 6	Sample 7	Simul2
Thickness [nm]	20.6	22.8	23.2	18.5	20
σ_{qw}^{chem}	0.0723	0.0356	0.0345	0.0331	0.0264
Interface width [No. of layer]	6	5	6	4	4
K of top interface	0.899	1.26	0.840	1.40	7.20

In addition, the standard deviation caused by the composition fluctuation at the QW is also calculated with the same method for the simulation, in which the indium atoms are randomly distributed in the (GaIn)As region. Compared with the QW in sample 7 (the most homogeneous one) with a σ_{qw}^{chem} of 0.0331, the simulated sample has a σ_{qw}^{chem} of 0.0274. The difference is probably caused by the following facts. In MOVPE, besides the the growth temperature and growth interruption, the epitaxy growth is influenced by the ratio of group III to group V atoms, the ratio of gallium to indium atoms, chamber pressure, etc. During these processes, atomic diffusion can takes place and indium cluster can be formed. Considering these factors, we can assume that the indium distribution in sample 7 grown and growth interrupted at low temperature is quite homogeneous compared with Simul 2. With the growth interruption at a higher temperature, indium atoms can be diffused to form indium cluster. Therefore, sample 6 has a less homogenerous indium distribution than sample 7. High temperature growth and growth interruption lead to a heterogeneous indium distribution as shown in sample 4. If the growth interruption takes place, indium atoms could have the chance to redistribute themselves and therefore improve the chemical homogeneity. Considering the low temperature and the short interruption time in sample 5, the influences of the growth interruption on the chemical homogeneity should be small and sample 5 should have a high standard deviation similar to sample 4. However, sample 5 only presents a slightly larger standard deviation than sample 6. The especially low standard deviation of sample 5 might be caused by the statistical error or the sample preparation, since the result is based on only one image in a small region.

Generally speaking, the chemical homogeneity is mainly determined by the growth temperature and the growth interruption temperature has only minor influence on it. Low temperature growth has advantage over high temperature growth in producing a homogeneous QW.

Quantitative evaluation of the interface abruptness

The abruptness of the top interface for all samples are characterized with two different approaches. First the interface widths of all samples are investigated. Sample 4 and sample 6 have the widest interface with 6 group III atomic layers. The interface of sample 7 is the narrowest and only 4 group III atomic layers wide. The interface of sample

5 is inbetween with a widness of 5 group III atomic layers. These clearly point out the facts that the growth and growth interruption at high temperature lead to a wider (intermixing) interface as presented in sample 4. If the growth interruption occurs at low temperature, the interface becomes narrower as shown by sample 5. Low temperature growth and growth interruption produce a sharp interface as shown by sample 7. If the growth interruption takes place at low temperature, the interface turns into a quite wider one as presented in sample 6. The simulated (GaIn)As-to-GaAs interface, taking the strain relaxation into account, shows an interface width of 4 group III atomic layers. In reality, the interface could be wider due to the atomic diffusion at the interface. With a comparison between the experiment and simulation, the conclusion could be drawn that the interface of sample 7 is quite sharp and the other interfaces are intermixing.

With the applicaiton of the error function fitting apporach, similar conclusions are achieved. The K factors of sample 4 and sample 6 are 0.899 and 0.84, respectively, indicating an intermixing interface. The K factor of sample 6 is 1.26, showing a less intermixing interface than sample 4 and sample 6. Sample 7 has a K factor of 1.40, pointing out the sharpest interface. As already mentioned, the simulated interface should be sharper than the experimental ones, because atomic diffusion is not considered in the simulation. The simulated interface has a K factor of 7.20. Compared with the experimental samples, the extraordinarily larger K factor is partly caused by the non-linear dependence of K factor on the interface abruptness as mentioned in section 5.1.5. In addition, a close look at the error function fitting curve as shown in figure 5.20 (c) points out the fitting curve does not fit the theoretical conditions perfectly. As assumed in the super cell, the indium compositions in the GaAs region and (GaIn)As region are 0% and 11%, respectively, which are marked by the red broken lines in figure 5.20 (c). Obviously, the fitted curve deviates from such values, and therefore an error is introduced during the fitting process. Although the error function fitting approach provides a much accurate quantitative evaluation of the interface, the above fitting error can also be produced and influence the results. As a result, both evaluation approaches of the interface abruptness should be combined to achieve a more robust conclusion.

In summary, the growth and interruption at low temperature lead to a sharp interface whereas an intermixing interface is produced at high temperature. High interruption temperature can significantly change a sharp interface formed at low temperature into an intermixing one. The intermixing interface generated at high temperature can also be improved by a low temperature interruption.

6 Quantitative evaluation of the chemical sensitive interface of (GaIn)P grown on GaAs

In chapter 5, the Q-method applied to HAADF images was introduced to find out the influences of growth conditions on the chemical homogeneity of QW and the interface abruptness. However, this method is not valid for material systems with chemical sensitive backgrounds. Therefore, in this chapter a background intensity map subtraction (BIMS) method is presented with the application to a material system with chemical sensitive backgrounds. Section 6.1 presents the BIMS method with an example of (GaIn)P/GaAs structure to reveal the interfacial structure as well as the chemical composition. In section 6.2, the method is applied to evaluate interfaces with different growth conditins to optimize the growth process. The contents of sections 6.1 and 6.2 are mainly based on the paper [34]. Section 6.3 deals with the application of the method to reveal island structures.

6.1 Background intensity map subtraction (BIMS) method

6.1.1 Introduction to BIMS method

Before the introduction of BIMS method, it is necessary to understand the image background intensity. For HAADF STEM images with atomic resolution, two important intensities can be obtained, namely the intensities of the atomic columns and the diffusely scattered background intensities between neighboring atomic columns as mentioned in section 4.3. Hence, for a specific background position, the corresponding intensity is mainly determined by the neighboring atomic columns and can be also used to determine the chemical composition of the atomic columns, which, however, is not discussed in the present study. On the other hand, the image background intensity also influences the collected intensities of the neighboring atomic columns, as demonstrated by simulated results in figure 4.5. Therefore, it is of great importance to subtract the image backgound intensity for the quantitative evaluation, especially for the evaluation of internal interfaces with atomic resolution.

As mentioned in chapter 1, the column ratio mapping method [31], [32], taking into account the image background intensity, was put forword and successfully applied to AlAs/GaAs materials. However, it works only with materials, whose chemical composition changes on only one sublattice, and provides a deteriorated resolution. To overcome the

shortcomings of the above method, the BIMS approach is developed to evaluate HAADF STEM images with atomic resolution in both <001> and <110> orientations. Basically speaking, a background intensity map, which has exactly the same pixel as the original image, is first calculated from the atomically resolved HAADF images. Then an image without the influence of image background intensity can be obtained though a subtraction of the background intensity map from the original map. In this study, (GaIn)P/GaAs material system is chosen to demonstrate the approach. In respect to this material system, the chemical composition of both group III and group V sublattices change across the interface, and hence the column ratio mapping method can not be applied. In addition, the (GaIn)P/GaAs heterointerface can be designed as a lattice matched one, to avoid the influences of the strain relaxation of the thin TEM samples on HAADF imaging. These heterostructures can be fabricated with highly different growth conditions using MOVPE, to find out the correlation between growth conditions with interface morphologies. Since the heterointerface is composed of atoms with highly different atomic numbers, it is also a good example to study the influence of diffuse scattering on composition evaluations for HAADF images with atomic resolution. The evaluation method is explained in section 6.1.2 in detail.

6.1.2 Backgrond intensity map subtraction method

BIMS is based on the quantitative evaluation method of HAADF images, introduced in section 5.2.2. Compared to the former, BIMS has introduced the additional determination of image background positions and the calculation of the image background intensity map.

To better understand how it works, an examplary HAADF image is given in figure 6.1 (a). Obviously, atomic columns as well as the interface are clearly resolved. Both group III and group V atomic columns can be recognized in the GaAs region whereas group V atomic columns are invisible in the (GaIn)P region owing to the small atomic number of P. The average intensity profile of the whole image along the growth direction is plotted using a red curve as shown in figure 6.1 (a). On the right side of the curve in figure 6.1 (a) (GaAs region), group V (As) atomic columns lead to high intensity peaks while low intensity peaks belong to group III (Ga) atomic columns. The reduced intensity of the line profile between high and low peaks stands for image background intensities of GaAs. Due to the small atomic number of P, the image background intensity is greatly reduced from GaAs region to (GaIn)P region. The background intensity can significantly influence the peak intensity either positively or negatively. That is also the reason why the intensity of group III atomic column in GaAs region is slightly larger than that in (GaIn)P region. The calculated image background intensity map as shown in figure 6.1 (b), which is calculated from the original image (Figure 6.1 (a)) and normalized to the impinging beam, also supports the observed phenonenon. Because the image background intensity is determined by the average atomic number of investigated materials, (GaIn)P

and GaAs have distinct intensity difference as shown by the map. Also, the heterogeneous intensity distribution can be observed in both regions. In GaAs it is mainly caused by the surface roughness and the measurement error whereas it is contributed by the local heterogeneous In distribution in the (GaIn)P region.

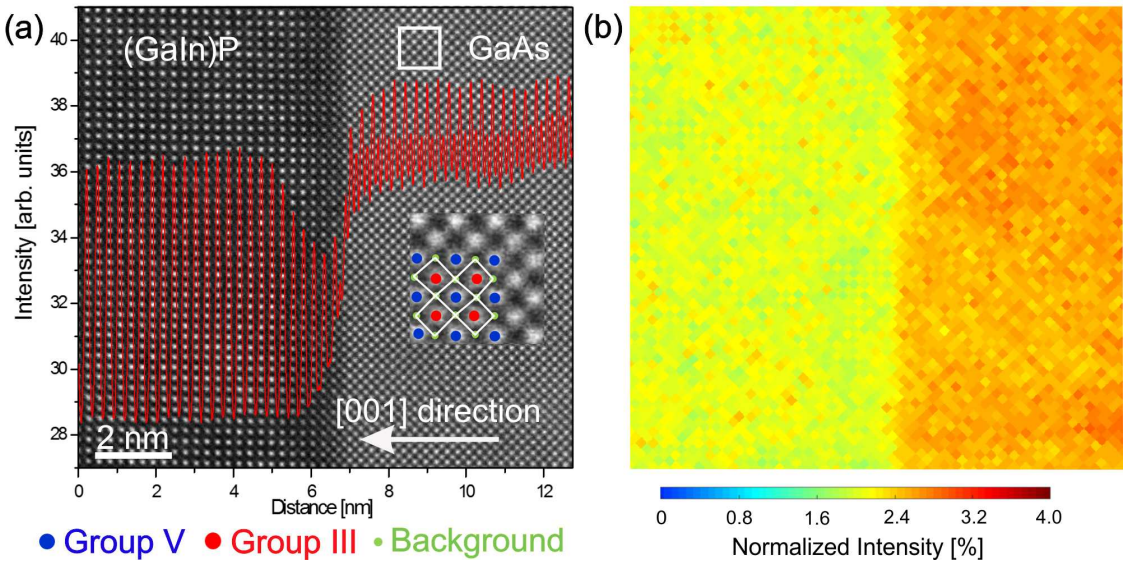

Figure 6.1: Exemplary HAADF image of (GaIn)P grown on GaAs viewed in [010] zone axis orientation. The growth direction is denoted by the white arrow in (a). The average intensity profile of the whole image along the growth direction is plotted overlaid to the original image in red line. The inset in (a) is a magnified part chosen by the white square in GaAs region in (a) with the overlay of a schematic illustration of one GaAs unit cell. The blue dots indicate the group V atomic column positions, whereas the red dots denote the group III atomic column positions. Five neighboring Voronoi cells are marked in the unit cell with white lines, and the green dots at their nodes represent the image background positions. (b) The calculated image background intensity map of (a) (in fractions of the impinging beam intensity.)

The example clearly demonstrates the influence of the image background intensity on atomic column intensities. Therefore, it is vital to determine the background intensity and subtract it from the original image. To realize the aim, the positions of all atomic columns are first determined using the Peak Pairs Analysis (PPA) software, and they are further separated from each other using a home-written Matlab program as group III and group V sublattices indicated by red dots and blue dots (Inset of figure 6.1 (a)), respectively. Then the image background positions can be decided according to positions of group III and group V sublattices with the Voronoi method [116]. For a set of atomic column positions acquired from a high resolution HAADF image, every atomic position can be used to generate a Voronoi cell as shown in the inset of figure 6.1 (a). The nodes of such Voronoi cells are termed as image background positions and are marked as green dots in the inset of figure 6.1 (a). Just like atomic column intensities,

the background intensity is also determined through an integration around background positions with a proper radius determined by the image magnification. In the current case, the investigated images have a magnification of 12 M and a radius of 38 pm, which corresponds to 3 pixels, is applied for the integration. In addition, the influence of the selected integrated radius on image background intensity has been investigated. The results show that the background intensity is rather stable as long as the integration does not cover any pixel from the atomic columns, as is supported by the simulated results. With image background positions, another set of Voronoi cells can be generated and cover the complete image. After such cells are filled with the corresponding background intensities, the image background intensity map is obtained again with Voronoi method as shown in Figure 6.1 (b).

Since the image background intensity map has exactly the same pixel size as the original image, it can be subtracted from the original image. Thus, the new image after subtraction is not influenced by the image background intensity. During this process, the wedge shape of the investigated region is fitted by a two dimensional plane function and the thickness gradient is further compensated using the thickness correction method introduced in section 5.1.3. With the application of thickness correction and background intensity subtraction, the new image can be applied for quantitative evaluation to derive the chemical composition map and reveal the interfacial features.

As already explained in section 5.2.2, a linear approximation can be made use of to describe the relationship between the collected atomic column intensity and the chemical composition. The In composition of group III atomic columns x_{III} can be determined by the measured column intensity I_m as follows

$$x_{III} = \frac{c_{XRD}(I_m - I_{Ga})}{I_{GaIn} - I_{Ga}} \tag{6.1}$$

where I_{Ga} is the average intensity of pure group III (Ga) atomic columns in the GaAs region. I_{GaIn} denotes the mean intensity in the (GaIn)P region. c_{XRD} is the determined mean In compositon in (GaIn)P region by HR-XRD. Similarly, the As composition of group V atomic columns x_{III} can be derived by

$$x_V = \frac{(I_m - I_P)}{I_{As} - I_P} \tag{6.2}$$

where I_P and I_{As} are the average intensity of group V atomic columns in (GaIn)P and GaAs regions, respectively. After chemical compositions for both group V and group III atomic columns are determined, the chemical composition map can also be drawn to show the interface.

To find out influences of the image background intensity on chemical composition maps, a comparison betweeen chemical composition maps without and with image background intensity subtraction is carried out. The calculated composition maps are shown in figure

6.2 (a)-(d). The color bar for group V sublattices denotes the As concentration, whereas the color bar for group III sublattices corresponds to the In concentration. To make the comparison between different maps straightforward, the same type of maps was alwayse plotted on the same color scale. From composition maps, the chemical composition is fluctuated in the pure regions, as is mainly caused by the TEM specimen surface roughness during sample preparation and the image noise. The As and In depth profiles in figures 6.2 (e) and (g) are derived from figures 6.2 (a) and (c), respectively. Similarily, the As and In depth profiles in figures 6.2 (f) and (h) are derived from figures 6.2 (b) and (d), respectively. For the group V sublattice, a comparison of composition maps (a and b) and depth profiles (e and f) shows that no obvious difference in the composition evaluation can be observed. On the other hand, significant differences are present for the composition evaluation at group III sublattice between c and d and also between g and h, especially at interface regions. Without subtraction of the image background intensity, the calculated In compositions at the interface are negative as shown in figure 6.2 (c) and (g), which is not reasonable. After image background intensity subtraction, it is obvious that reasonable In compositons are presented at the interface as shown in figure 6.2 (d) and (h). The influences of image background intensity on group III chemical compositions are removed. What causes these abnormal In compositons at the interface? A detailed look into the determination of the chemical composition gives a clue to the phenomenon. As mentioned, the determination of the chemical composition is based on the linear approximation expressed in equation 6.1. If the measured atomic column intensity I_m is out of the range of pure intensity of Ga atomic columns I_{Ga} and the intensity of mixed Ga and In atomic columns I_{GaIn}, the sign of the calculated In composition will be reversed. In the present case, intensities of group III atomic columns at the interface are strikingly reduced and smaller than both I_{Ga} and I_{GaIn} due to the influence of image background intensity as shown in figure 6.1. This is the reason why group III atomic columns in the example present the unreasonable In compositions.

In addition, the standard deviation of both As and In compositions (intensity) at every atomic column in every (001) atomic plane along the growth direction is calculated and plotted as the shaded area in figure 6.2 (e)-(h). Obviously, the larger the average atomic number, the larger the standard deviation value. For group V atomic columns, the standard deviation of the As region is larger than that of the P region. The standard deviation also increases with increasing thickness of the investigated region, due to a large measured intensity of more atoms. Besides, the standard deviation of In composition in (GaIn)P region is mainly caused by the inhomogeneous In distribution during the growth process.

As a result, it is a necessity to subtract the image background intensity for chemical sensitive interfaces to obtain reasonable results. Quantitative evaluation of the interface can be carried out and then the corresponding results can be correlated to the growth condition, to optimize growth parameters. This will be explained in section 6.2.

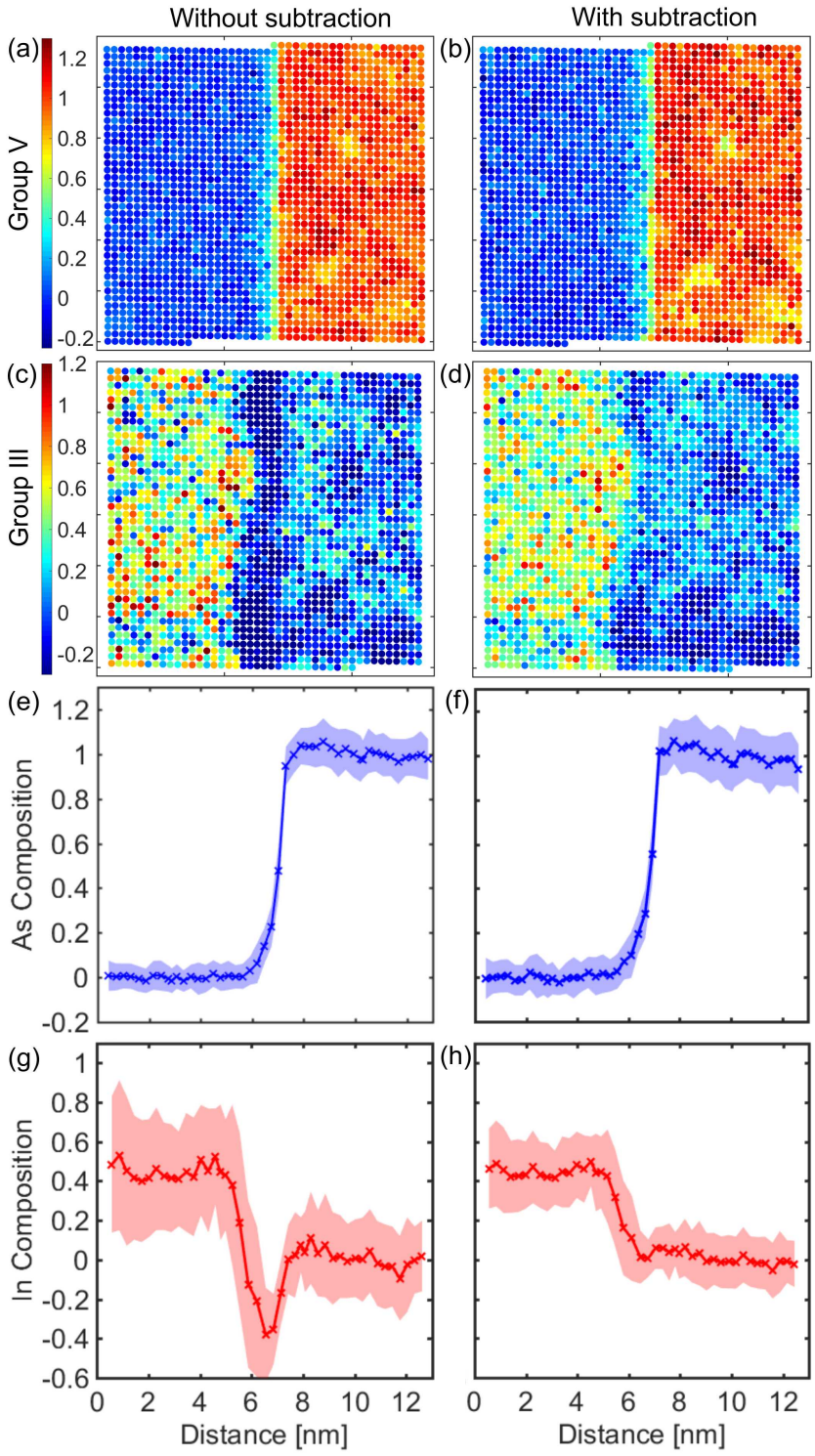

Figure 6.2: Chemical composition maps of (a) group V and (c) group III sublattice without background intensity subtraction together with (b) group V and(d) group III sublattice with background intensity subtraction. Profiles of the average As and In composition of every (001) atomic plane along the growth direction are plotted. Profiles (e) and (g) correspond to the composition maps of (a) and (c) without subtraction, respectively. Profiles (f) and (h) correspond to the composition maps of (b) and (d) with subtraction, respectively. The shaded area around profiles denotes the corresponding standard deviation among different atomic columns in each (001) atomic plane along the growth direction.

6.2 Evaluation of the heterostructure interface

6.2.1 Investigated (GaIn)P/GaAs material systems and the growth conditions

As mentioned in section 2.3.2, (GaIn)P/GaAs has drawn a lot of attention for the promising applications in electronic and optoelectronic industries. The performances of such devices are mainly determined by the control of (GaIn)P/GaAs interfaces.

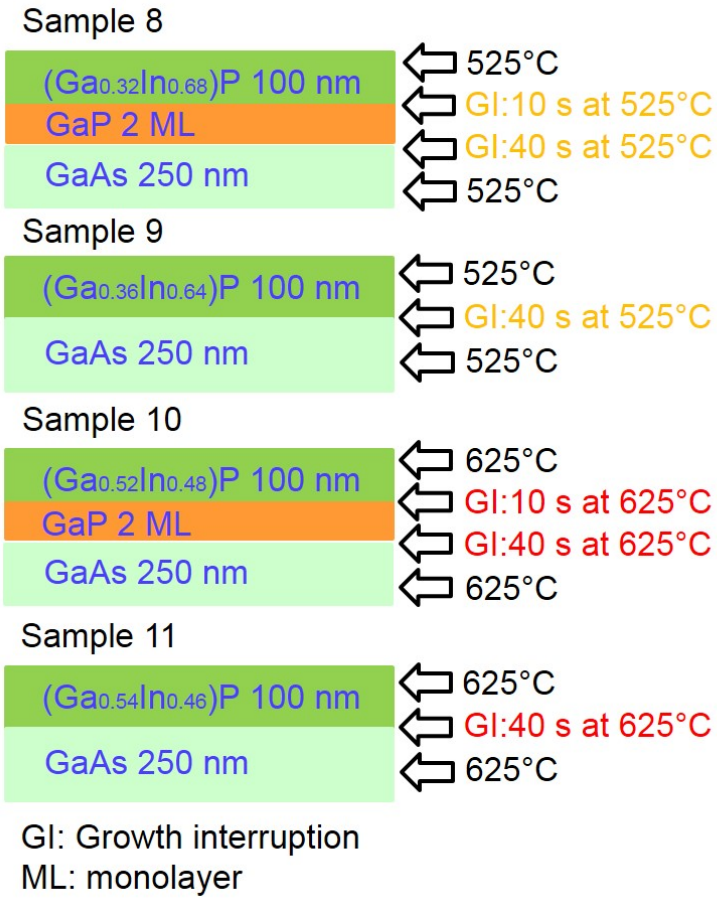

Figure 6.3: Schematic layer structures of investigated (GaIn)P/GaAs material systems. The growth temperature, growth interruption (GI) time together with the average In chemical composition of (GaIn)P layers determined using HR-XRD are listed.

To better understand and optimize the growth process, ternary (GaIn)P layers were grown on a 250 nm thick GaAs buffer layer, which is grown on (001) GaAs substrate using MOVPE under different growth conditions. All (GaIn)P layers have a thickness of around 100 nm. Different growth interruption times of 10 s and 40 s were applied to the GaAs-to-(GaIn)P interface at temperatures of 525 °C and 625 °C, respectively. Besides the growth temperature and growth interruption time, GaP interlayers were also introduced at the interface in order to find out its influences on the interface morphology.

The growth interruption time between the (GaIn)P layer and the GaAs buffer layer is 40 s for all samples with different growth temperatures. If a GaP interlayer with a width of two monolayers was applied at the interface, the growth interruption between the GaP interlayer and the GaAs buffer layer was considered. After the growth of GaP interlayers, a growth interruption time of 10 s was introduced. The In composition of the (GaIn)P layers was determined by HR-XRD and dynamical simulations. Theoretically, the In composition of the lattice-matched (GaIn)P/GaAs interface without strain should be 52 %. However, the actual value of the In composition of (GaIn)P layers is slightly deviated from the theoretical one, which is caused by different growth conditions (such as temperature, and so on). Also the fact points out the existance of strain at the investigated interfaces. The schematic illustration of the layer structure as well as the In composition of (GaIn)P layers is shown in figure 6.3. The related growth parameters such as growth temperature, growth interruption time and the introduction of GaP interlayer are also given in this figure.

6.2.2 Interface morphology under different growth conditions

In this section, with the introduced BIMS approach, (Ga,In)P/GaAs internal interfaces with different growth conditions are quantitatively evaluated and compared with each other. In order to obtain reasonable and reliable results, the comparison between different internal interfaces should take place at carefully selected regions. One should pay special attention to the so-called cross talk between neighboring atomic columns, which can greatly influence the evaluated result. It is mainly determined by investigated materials and STEM settings. In order to minimize the influences of the cross talk, the investigated regions should have a thickness less than 40 nm, which is already proved by figure 5.4. In addition, interfacial features can be smeared out at thick regions due to projection effects, which makes it impossible to characterize interfacial structures. On the other hand, for TEM samples less than 10 nm thick, the scattered intensity from amorphous layers can reach a large amount of the total scattered intensity of the region, and thus significantly influence results. Usually, amorphous layers are generated on both side of the sample surface during the sample preparation process. To apply the statistical evaluation, the compared regions between different samples should have not only similar thickness but also similar field of view. The thickness of the investigated region can be determined through the comparison with contrast simulation.

For the four samples investigated in this section, HAADF images with atomic resolution are acquired with the same magnification to make sure that they all have the same field of view. With the routine evaluation process, all normalized images go through the thickness correction and image background intensity subtraction. After that, chemical composition maps for both group V and group III sublattices are calculated. Since the quantitative evaluation of HAADF images has been already explained in detail in section 5.2.2, the

intermediate results are not shown here any more. For every sample, chemical composition maps for both group V and group III sublattices as well as the corresponding depth profiles are presented. Results of sample 8 (thickness $t = 34$ nm) and sample 9 (thickness $t = 32$ nm) grown at 525 °C are shown in figure 6.4 whereas results of sample 10 (thickness $t = 20$ nm) and sample 11 (thickness $t = 18$ nm) grown at 625 °C are shown in figure 6.5. Both As and In chemical compositions are represented by the color bar. All group V composition maps share the same color bar and so do group III composition maps, to make the composition much straightforward. In figures 6.4 and 6.5, composition maps for group V sublattice are shown in (a) an (b) while composition maps for group III sublattice are shown in (c) and (d), respectively. Below the composition maps, depth profiles of the average As composition of every (001) atomic plane for group V are plotted in (e) and (f). The shaded area around the profile indicates the corresponding standard deviation of the composition (intensity) of every (001) atomic plane, respectively. Similarily, the depth profiles of the mean In composition with the standard deviation are shown in (i) and (j). The profiles were calculated by averaging over the whole field of HAADF images, i.e. a width of around 10 nm. Since the standard deviation can be used as a quantitative measure of the interface structure, the standard deviation of the chemical composition (intensity) of group V sublattice in every (001) atomic plane along the growth direction is also plotted in (g) and (h) for clarity as a separate graph. The same representation does not make sense for group III sublattice, because the large standard deviation in the (GaIn)P region makes the feature at the interface not as clear as that in group V sublattice. This is mainly contributed by the inhomogeneous In distribution, surface roughness and also detector noise.

Besides the already mentioned factors, the same criteria should also be applied for the quantitative evaluation to make a fair comparison between different interfaces. Here, the 90/10 evaluation approach and the error function fitting approach as introduced in section 5.1.5 are made use of. The black lines in the composition profiles in figures 6.4 and 6.5 mark the interface width of the investigated interface. The widths of the respective interfaces, counted as the number of atomic layers of either group III or group V sublattice, can be easily determined and are summarized in table 6.1 for the four samples. It is worth pointing out that the distance between two neighboring atomic layers is half of the unit cell in this nomenclature, since group V and group III sublattices are seperated from each other and are treated individually. If interfaces of both group V and group III are not located at exactly the same position, a new parameter is needed to describe the distance between two depth profiles. Here, this distance is defined as the number of atomic layers from 90 % of the total In concentration for group III to 90 % of the total As concentration for group V. This parameter is termed as 'Distance 90 % G-III to 90 % G-V' in table 6.1 and the corresponding results are also given. Obviously, the disadvantage of the approach is the low accuracy of only ± 1 atomic layer, determined by the crystal structure.

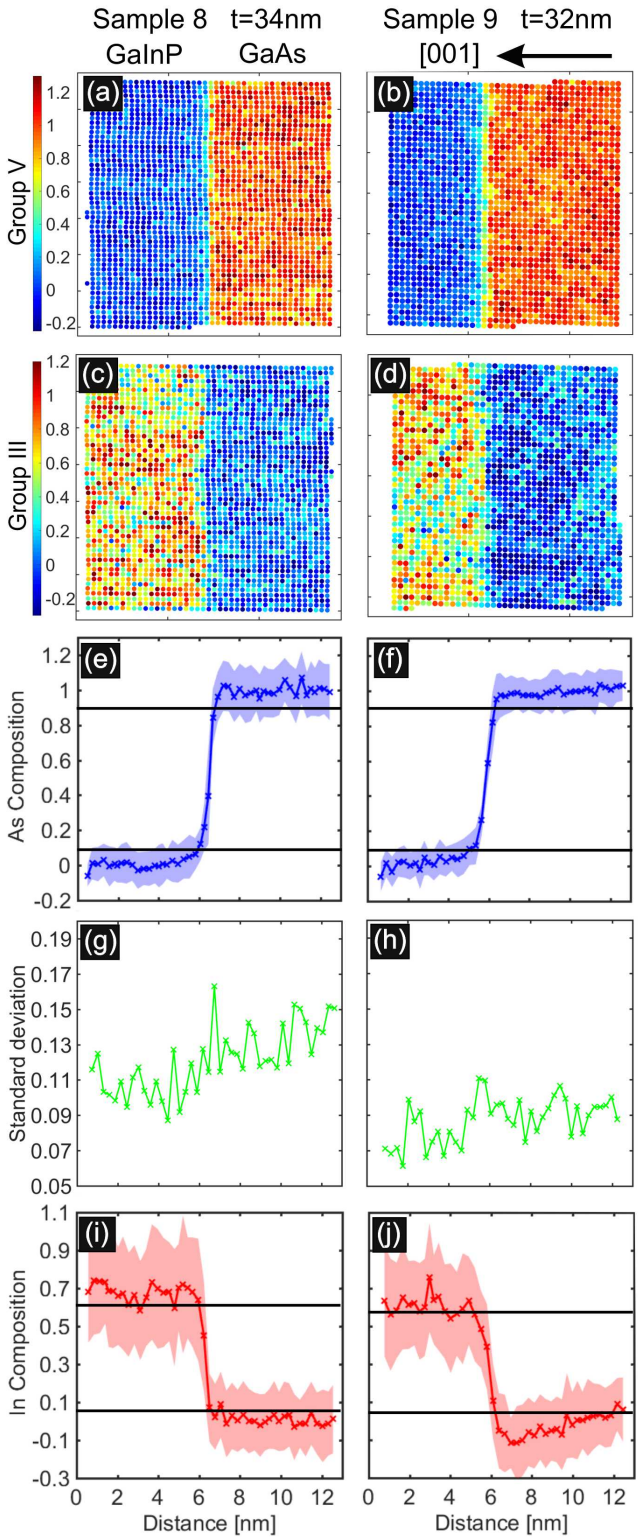

Figure 6.4: Chemical composition maps of group V (a) sample 8, (b) sample 9, of group III sublattices (c) sample 8, (d) sample 9. The TEM specimen thicknesses are given for each sample. The growth direction is marked by the arrow on top of (b). The profiles of the average As and In composition of each (001) atomic plane along the growth direction are shown in (e) and (f) and (i) and (j), respectively. The shaded areas around the profiles are the standard deviation of the intensity (composition) along the interface for each point. For clarity, the standard deviation profiles of the group V sublattice are also plotted in separate figures (g and h).

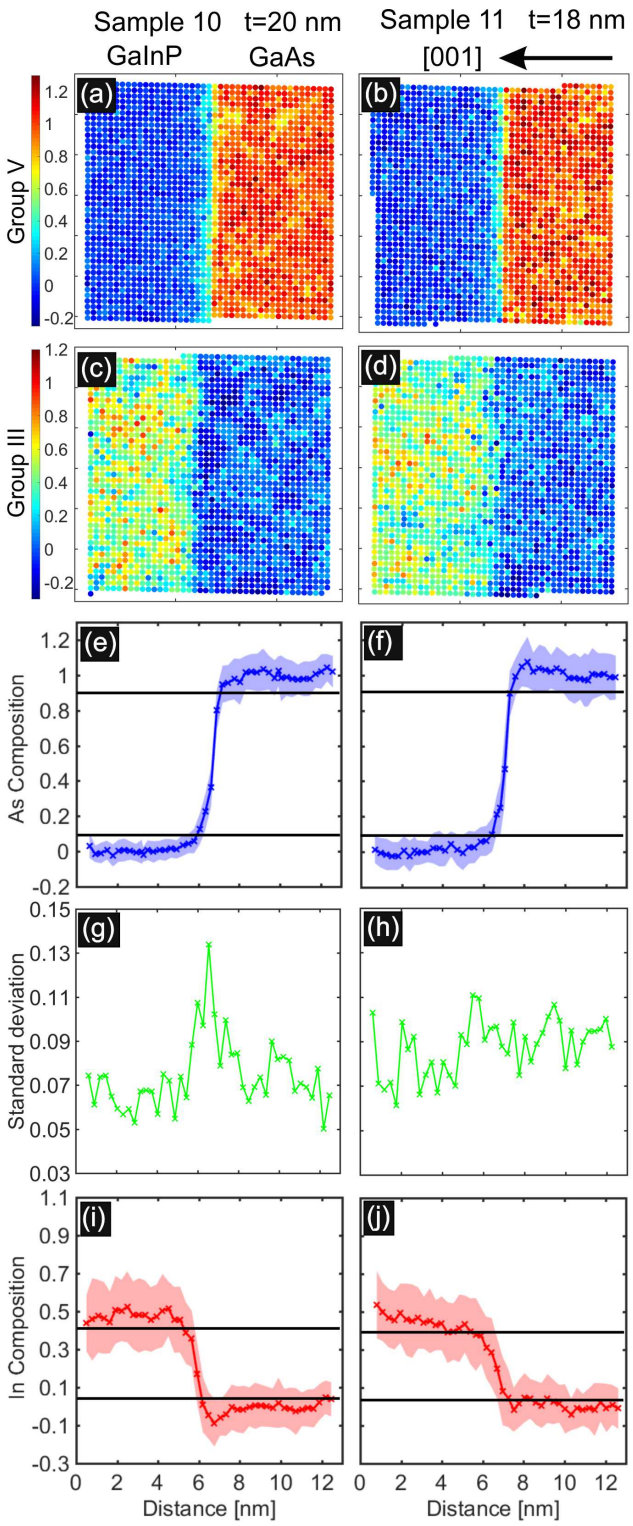

Figure 6.5: Chemical composition maps of group V (a) sample 10, (b) sample 11, of group III sublattices (c) sample 10, (d) sample 11. The TEM specimen thicknesses are given for each sample. The growth direction is marked by the arrow on top of (b). The profiles of the average As and In composition of each (001) atomic plane along the growth direction are shown in (e) and (f) and (i) and (j), respectively. The shaded areas around the profiles are the standard deviation of the intensity (composition) along the interface for each point. For clarity, the standard deviation profiles of the group V sublattice are also plotted in separate figures (g and h).

Another possibility to characterize the interface abruptness with much more accuracy is the error function fitting approach. With this method, parameter K, describing the interface abruptness, as well as parameter C, defining the position of the chemical composition transition (interface position), can be obtained by fitting the error function to depth profiles of both sublattices. Besides, ΔC, describing the distance of the transition positions between group III and group V depth profiles, can also be determined. The K factors for both group V and group III interfaces together with ΔC are summarized for four samples in table 6.1. To better understand the distance of the transition positions between group V and group III, a pair of error function fitting curves for both group V and group III sublattices are given in figure 6.6. As shown in the figure, the original composition data points are denoted by the red (group III) and blue (group V) crosses. The error function fitting curves are plotted in red (group III) and blue (group V) lines. For each fitting, the interface position C is marked by the black vertical broken line as the corresponding position of composition transition in the figure. Another advantage of error function fitting approach lies in the fact that parameters K and C are independent from each other, while a broader composition transition will also lead to a wider interface with the 90/10 evaluation method. For comparison, the positions of 90 % of both the total In composition (group III) and total As composition (group V) are indicated by red and blue broken lines, respectively. From the examplary plotting, obviously ΔC is the distance from 50 % G-III to 50 % G-V and is alwayse smaller than distance 90 % G-III to 90 % G-V.

Table 6.1: Quantitative evaluation of the abruptness of the composition gradient of both sublattices and for the width of the interface for samples 8-11.

Sample	8	9	10	11
90/10 G-III [atomic layer]	2	4	3	7
90/10 G-V [atomic layer]	4	5	4	5
Distance 90 % G-III to 90 % G-V [atomic layer]	3	4	6	7
K G-III [nm^{-1}]	3.72	2.18	2.36	1.10
K G-V [nm^{-1}]	2.44	2.01	1.92	2.29
ΔC [nm]	0.206	0.031	0.859	0.504

The differences of abruptness and width between investigated interfaces are quite distinct. Now the interfacial features as well as correlated growth conditions will be discussed to find out influences of different parameters on the interface morphology. For the results obtained from error function fitting approach, a larger k denotes an abrupter interface whereas a smaller ΔC indicates a narrower interface. For samples grown at 525 °C, the main difference between sample 8 and sample 9 lies in the existance of the GaP interlayer, ignoring the minor In compositon difference of (GaIn)P layers. With the introduction of GaP interlayer in sample 8, the K factors of both group V and group III interfaces are larger than those of corresponding interfaces in sample 9. It means that more abrupt

interfaces can be obtained. On the other hand, sample 8 has also a larger ΔC than sample 9. However, this points out that the introduction of a GaP interlayer leads to an increased width of the interface. The introduction of the GaP interlayer has a significant positive effect on the abruptness of the interface, especially on the interface of the group III sublattice. If sample 10 and sample 11 grown at 625 °C under otherwise unchanged growth conditions are taken into consideration, similar conclusions can be drawn. The group III composition profile in sample 10 has a much sharper interface with the introduction of a GaP interlayer. At the same time, a much wider composition transition region from GaAs to (Ga,In)P is formed in sample 10. All interfaces characterized with the 90/10 evaluation method basically show the same results. However, the inaccuracy of this method is still the main disadvantage, especially for the comparison between sharp interfaces. Under this condition, this approach is probably not valid any more, since the interface width is only counted as multiples of a monolayer. Still it is worth emphasizing that no approach is perfect as already explained in section 5.3.3 and that results obtained from both approaches should be considered together to draw a reasonable conclusion.

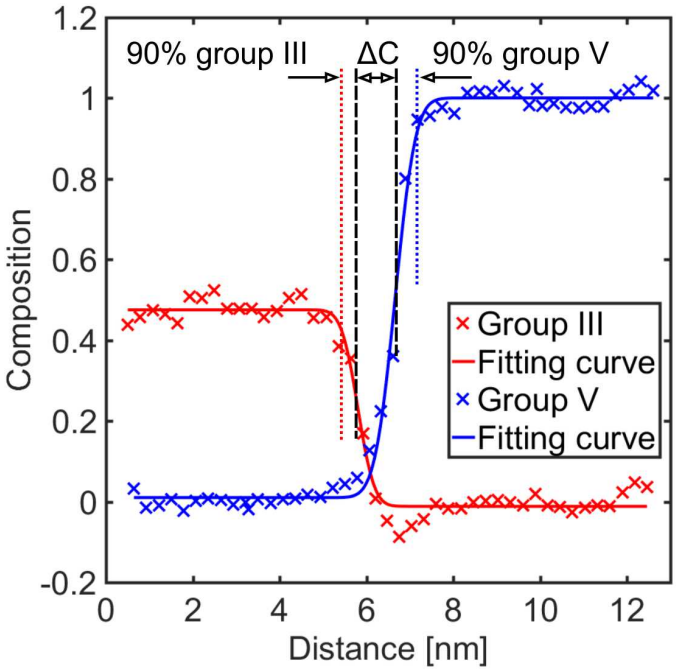

Figure 6.6: Error function fitting to the group V and group III depth profiles of sample 10. The distance ΔC between two transition positions of group V and group III depth profiles are marked by the vertical black lines. As a comparison, the distance from 90 % group III to 90 % group V is also marked in the plot by red and blue vertical lines, respecctively.

A comparison between samples grown at 525 °C and samples grown at 625 °C should be carried out carefully, since investigated regions of different samples do not share the same thickness. From table 6.1, the results based on both interface evaluation approaches point towards the advantage of low temperature growth at 525 °C over high temperature

growth at 625 °C in producing a sharp interface. Obviously, the interface widths of both group V and group III profiles as well as the distance 90 % G-III to 90 % G-V are smaller at low growth temperature. The reason lies in the reduced thermal diffusion at lower temperature. Higher temperature provides more energy to activate the atomic thermal diffusion. In addition, sample 10 has the largest ΔC of 0.859 nm as shown in table 6.1. Also, a close look at group V and group III depth profiles of sample 10 plotted in figure 6.6 shows that the zero-As plateau of group V profile and zero-In plateau of group III profile is connected. It means that in this region only GaP exists. Otherwise a mixture of (Ga,In)/(P,As) can be formed if such two plateaus are obviously apart from each other. So sample 10 grown at 625 °C with a GaP interlayer presents a GaP-like interface whereas sample 8, 9 and 11 have (Ga,In)/(P,As)-like interfaces.

The standard deviation of the chemical composition (intensity) can be considered as a measure of the roughness of the interface. Sample 8, 10, and 11 show an obviously increased standard deviation at the interface while this increased standard deviation at the interface can not be observed for sample 9. For sample 8 and 10 with the introduction of a GaP interlayer, probably due to the memory effect [5] of As atoms, a mixture of P and As is formed at the interface and therefore leads to an increased standard deviation at the interface. For sample 11 grown at 625 °C without GaP interlayer, it is likey that the existance of the microscopic island structure has caused this high standard deviation at the interface, which will be dealed with in detail in section 6.3. The small standard deviation at the interface in sample 9, grown at 525 °C without the GaP interlayer, indicates that there are no obvious interfacial structures. This sample also presents the smallest (almost negligible) distance of the composition transition between group V and group III profiles (ΔC = 0.031 nm).

In short summary, based on the above quantitative analysis of the interfaces under different growth conditions, the compound semiconductor clearly presents a sharper heterointerface fabricated at a growth temeprature of 525 °C compared to 625 °C. The introduction of a GaP interlayer can additionally improve the abruptness of the heterointerface, as verified by the comparison between different samples. At the same time, the GaP interlayer also leads to an increased separation between the interested constituent QW and the barrier.

6.3 Characterization of the microscopic island structure

In the previous section, the BIMS method is applied to find out the influences of growth conditions on the heterointerface of (GaIn)P grown on GaAs. In this section, sample 9 and sample 11, without the introduction of a GaP interlayer, are further made use of to demonstrate the evaluation of the island structure. To realize this aim, HAADF images with similar thickness and field of view are carefully selected to make the comparison between different images reasonable and reliable. After the thickness of the investigated regions are determined, regions with a proper thickness are chosen to satisfy the requirements for analysis as explained in section 6.2.2.

As shown in figure 6.7, the investigated regions have a thickness of 32 nm and 34 nm for sample 9 and sample 11, respectively. From figure 6.7 (a) and (b), both interfaces and individual atomic columns can be clearly resolved from original images, which are not shown in section 6.2. Since the image contrast is determined by the average atomic number, group III and group V atomic columns have similar brightness in GaAs region whereas in (GaIn)P region group V atomic columns disappear. Therefore, the interface can be identified by the appearance of group V atomic columns in this section. As a routine, chemical composition maps of In for group III and As for group V were calculated to quantitatively analyze the interface. Based on these maps, which are not shown here any more, the profiles of the average In and As composition of every (001) atomic plane along the growth direction are again plotted in figure 6.7 (c)-(f), respectively. The shaded area around the profiles again indicates the standard deviation of the intensity (composition) of each [010] atomic column in (001) atomic plane. Also, these standard composition deviation profiles of both In and As are plotted in figure 6.7 (g)-(h). As already mentioned earlier, the standard deviation can be referred to as a reflection of the interface morphologies (i.e. roughness, size and distribution of the islands at the interface). For pure atomic columns, the standard deviation is mainly caused by the measurement error and the surface roughness.

Obviously, the standard deviations of GaIn regions (marked as red pentagram in figure 6.7 (g)-(h)) are higher than those of Ga regions for both sample 9 and sample 11, which is due to the heterogeneous distribution of In in Ga atomic sites. This also explains why standard deviation profiles of group III at the interface are not as featured as those of group V. Therefore, in the following part we mainly focus on the standard deviation of group V to investigate the interface. In figure 6.7 (h) the standard deviation profile for group V clearly exhibits a pronounced peak at the interface for sample 11. This peak implies the existence of some interfacial structures, which, however, can be concealed because of projection effects in the thick TEM specimen.

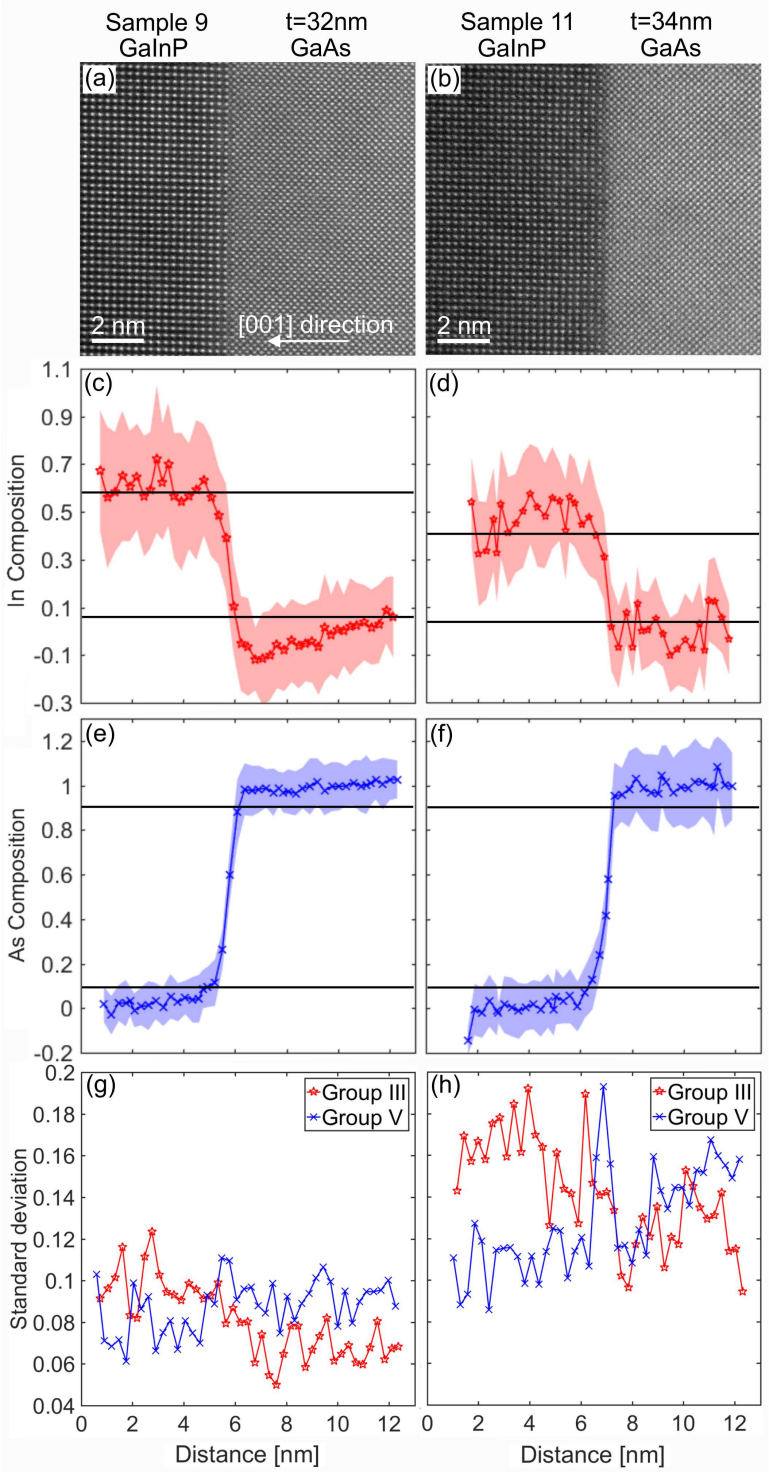

Figure 6.7: HAADF STEM images of (a) sample 9 grown at 525 °C and (b) sample 11 grown at 625 °C in [010] zone axis orientation. The TEM specimen thickness is given for both samples. The growth direction is indicated by the arrow in (a). The profiles of the average In and As composition of each (001) atomic plane along the growth direction are shown in (c) and (d) and (e) and (f), respectively. The shaded areas around the profiles are the standard deviation of the intensity (composition) along the interface for each point. The black lines in (c)-(f) indicate the compositions of 10-90 % of bulk regions and define the interface region. For clarity, the standard deviation profiles of group III and V sublattices are also plotted in (g) and (h) for sample 9 and sample 11, respectively.

To find out interfacial structures hidden in figure 6.7, the investigation of sample 11 is focused on regions with a smaller thickness. In fact, the interfacial structure can be identified as the microscopic island with a height of one group III/V atomic layer. The detailed structural information can be observed in the normalized STEM image (Figure 6.8 (a)), where atomic column intensities scale to chemical compositions. To better reveal the composition difference at the interface, the chemical composition map of group V (As) is also shown in 6.8 (b). The profiles of the averaged In and As compositions are plotted in figure 6.8 (b)-(c). The shaded area around the profiles indicates the corresponding standard deviations. The standard deviation profile of the compositions (intensities) for group V (blue cross) is plotted in figure 6.8 (e). From the curve, the existence of an even more pronounced peak at the interface (compared with figure 6.7 (h)), can shed some light on the issue. This peak can be caused either by several nanometer sized islands or by the border of one microscopic island (GaAs). With a close look we can notice that there is an intensity jump at the interface in group V sublattice. A better observation of the intensity change can be found in the inset of figure 6.8 (a), which is a magnified image of the region inside the white rectangle. Besides, the chemical composition change of As at the interface also supports the existance of the island structure as shown in figure 6.8 (b).

Therefore, it is convincing that the high standard deviation at the interface is mainly caused by the border of one microscopic island. To further prove the existence of this microscopic island, indicated in figure 6.8 (a), this image is divided into section 1 and section 2 (marked on the left side of the original image) by a white broken line at exactly the intensity jumping position. Then, standard deviation profiles of group V sublattice for both sections are plotted in figure 6.8 (e). Obviously, the extremely high standard deviation peak is gone and only small standard deviation peaks are observed at the interface for both sections, which points to the fact that a microscopic island with a height of only one group V monolayer exists in the current image. On the other hand, if several nano-sized islands are present in the image, the extremely high standard deviation at the interface will not be significantly influenced. Only if a step caused by a microscopic island is situated at the marked position in the image, the standard deviation of both sections could be strikingly lowered at the interface.

To show how the microscopic island develops at the interface, the group V (001) atomic planes are indexed by numbers from 1 to 7 as shown below the inset in figure 6.8 (a). The profiles of As composition (intensity) for all marked atomic planes (1-7) are plotted in three dimensions in figure 6.9, where the evolution of the island structure from GaAs to (GaIn)P is clearly presented. For atomic planes 1 and 2, which are invisible in the (GaIn)P region, the As concentration vibrates around zero whereas the As composition of plane 6 and 7 in the GaAs region fluctuates around 1. In between the chemical composition change is quite distinct, illustrating the development of the island structure at the interface, especially in atomic plane 4.

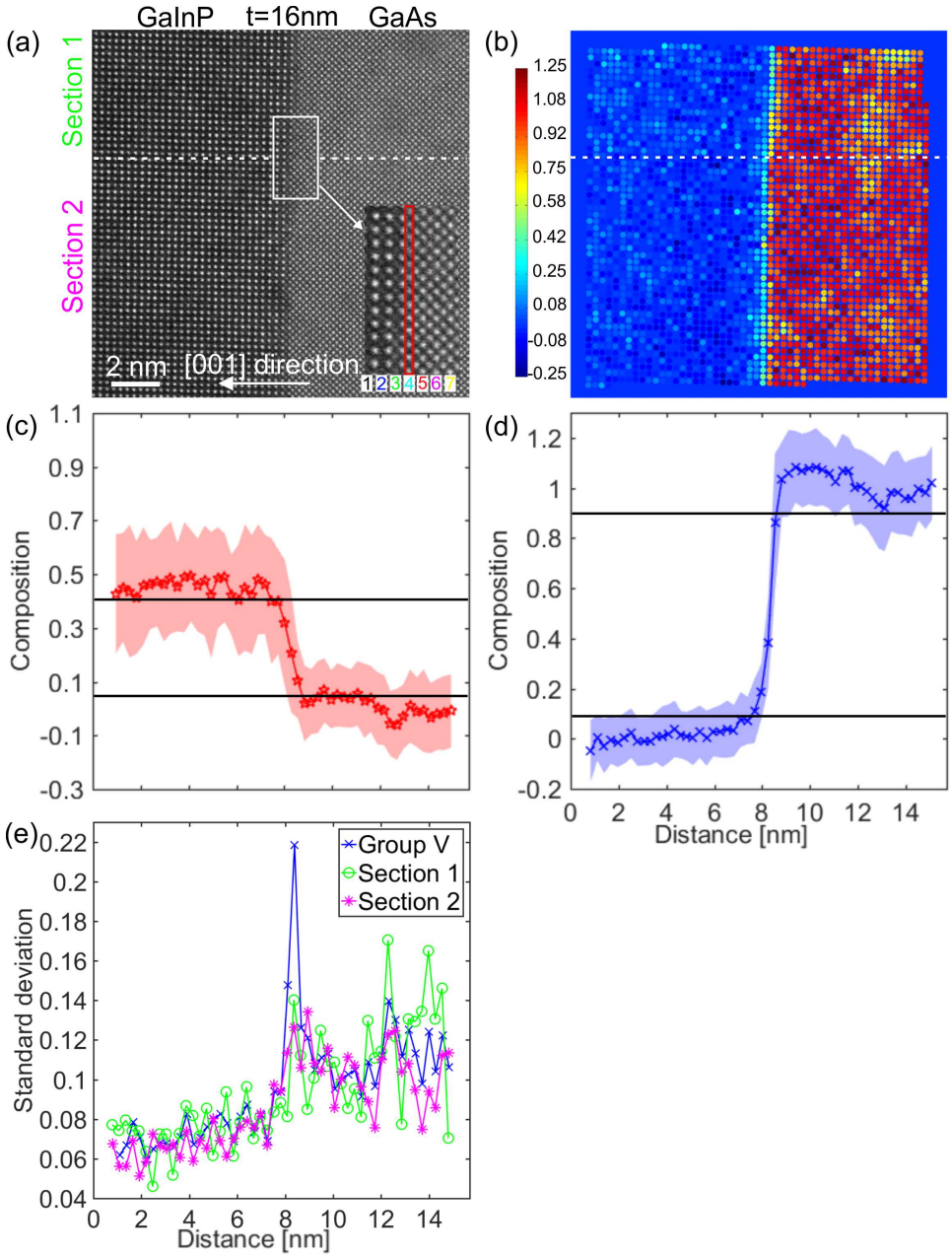

Figure 6.8: HAADF image of (a) sample 11 on a thin region in [010] zone axis orientation. The white broken line denotes the position of the border of one microscopic island at the interface and separates the image into section 1 and section 2 as marked on the left side of the image. The inset is a magnified image of the region chosen by the white rectangle. The group V atomic plane chosen by the red rectangle in the inset shows the border of one microscopic island along the interface. Also, all group V atomic planes in the insets are marked by numbers under the inset, the corresponding profiles are plotted in figure 6.9. To better observe the border of the island, the corresponding As composition map is plotted in (b) and the border of the island is also marked by the white broken line. The profiles of the average In and As composition of each (001) atomic plane along the growth direction are shown in (c) and (d), respectively. The shaded areas around the profiles are the standard deviation of the intensity (composition) along the interface for each point. The black lines in (c) and (d) indicate the compositions of 10/90 % of the bulk regions and define the interface region. For clarity, the standard deviation profiles of the As composition (intensity) of every [010] atomic column in each (001) atomic plane are plotted in (e) for the group V of the whole image (blue cross), section 1 (green circle) and section 2 (magenta asterisk), respectively.

The microscopic island structure can lead to a distinct increase of the standard deviation at the interface. To quantitatively compare the standard deviation changes at the interface with and without island structure, the mean standard deviations at interfaces $\sigma_{interface}$ and bulk regions σ_{bulk} as well as the corresponding relative changes $\Delta\sigma/\sigma_{bulk}$ ($\Delta\sigma$=$|\sigma_{interface}$ - $\sigma_{bulk}|$) in percent are calculated and listed for all samples and sections in table 6.2. Here, the interface width is defined with the 90/10 evaluation method as the region, where the respective compositions (intensities) change between 10 and 90 % of their bulk values. As shown in figure 6.7 and 6.8, the interface width is marked by two black lines in the profile plots for both group III and group V sublattices, respectively. Then, the mean standard deviation of the interface region can be calculated. For sample 9 grown at 525 °C without interface structures, the standard deviation at the interface is increased by 15.9 %. For sample 11 grown at 625 °C with microscopic islands, a rise of 25.3 % in the standard deviation at the interface is observed. If projection effects are minimized by investigating a thinner region, the increase in the standard deviation at the interface can be as high as 68.3 % as shown by sample 11 with a thickness of 16 nm. After the image (Figure 6.8 (a)) is separated into section 1 without interfacial structure and section 2 with the GaAs microscopic island, section 1 has a comparable standard deviation jump (12.4 %) at the interface as sample 9 whereas section 2 exhibits a relatively higher increase at the interface in standard deviation because of the island structure.

To better understand the heterointerface of (GaIn)P grown on GaAs, contrast simulations of an abrupt (GaIn)P/GaAs interface are implemented. In order to compare with experiment, three super cells are generated as the input for three simulations (Simul 3, Simul 4 and Simul 5). Simul 3 has an indium concentration of 64 % and a thickness of 32

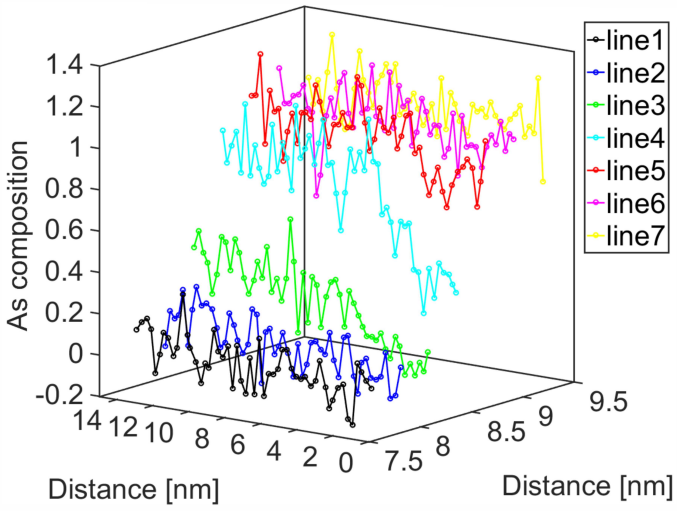

Figure 6.9: Composition profiles of the As composition (intensity) of group V atomic planes marked in the inset in figure 6.8.

Table 6.2: The mean standard deviation of As composition (intensity) for group V sublattice of (001) atomic plane at both interfaces and bulk regions.

	Thickness [nm]	Mean $\sigma_{interface}$	Mean σ_{bulk}	$\Delta\sigma/\sigma_{bulk}$ [%]
Sample 9	32	0.0992	0.0855	15.9
Sample 11	34	0.156	0.125	25.3
Sample 11	15	0.153	0.0908	68.3
Section 1	15	0.105	0.0932	12.4
Section 2	15	0.120	0.0840	42.9

nm, which corresponds to Sample 9 in figure 6.7. The indium composition of Simul 4 and Simul 5 is 46 % and the thickness is 15 nm and 34 nm, respectively, corresponding to two investigated regions of sample 11. Considering the small strain existing at the investigated interfaces, all generated super cells are relaxed with the COMSOL Multiphysics®suite using periodic boundary conditions. From simulated images shown in figure 6.10 (a)-(c), all interfaces are quite sharp at different thicknesses. Then, the profiles of indium composition for group III and arsenic composition for group V are plotted in figure 6.10 (d)-(i). The black lines plotted in composition profiles determine the interface width. The shaded areas around the profiles represent the standard deviation of the composition (intensity).

The quantitative evaluation of different interfaces is again carried out with the mentioned 90/10 evaluation method and the error function fitting method introduced in section 5.1.5. Considering the inhomogeneous In distribution in (GaIn)P region, only the interface of the group V sublattice is evaluated in this study. The quantitative evaluation results of all investigated interfaces are summarized and listed in table 6.3. To find out the influences of the microscopic island structure on the interface morphology, the interface at regions without microscopic islands is also characterized for sample 11 and corresponding average results are also listed in table 6.3.

Table 6.3: Quantitative evaluation of the group V interface for both experimental and simulated images with different thicknesses at different positions.

	Thickness [nm]	Position	90/10 Group V [atomic layer]	K [nm^{-1}]
Sample 9	32	No island	5	2.01
Sample 11	34	Island	4	2.28
Sample 11	15	Island	4	2.29
Sample 11	14	No island	3	2.74
Simul 3	32	No island	0	8.54
Simul 4	34	No island	0	9.09
Simul 5	15	No island	0	11.3

It is clear that sample 11 grown at 625 °C has a narrower (abrupter) interface than that grown at 525 °C (sample 9) characterized with the 90/10 evaluation method. Besides, the interface of sample 11 is even narrower without the microscopic island, with a width of only 3 atomic layers. It means that the formation of microscopic islands deteriorates the

quality of interface and therefore leads to a mixing interface. The same conclusion can be arrived at using the error function fitting method. A larger K from sample 11 indicates a steep interface compared with sample 9. Also, the interface becomes much more abrupt without microscopic islands.

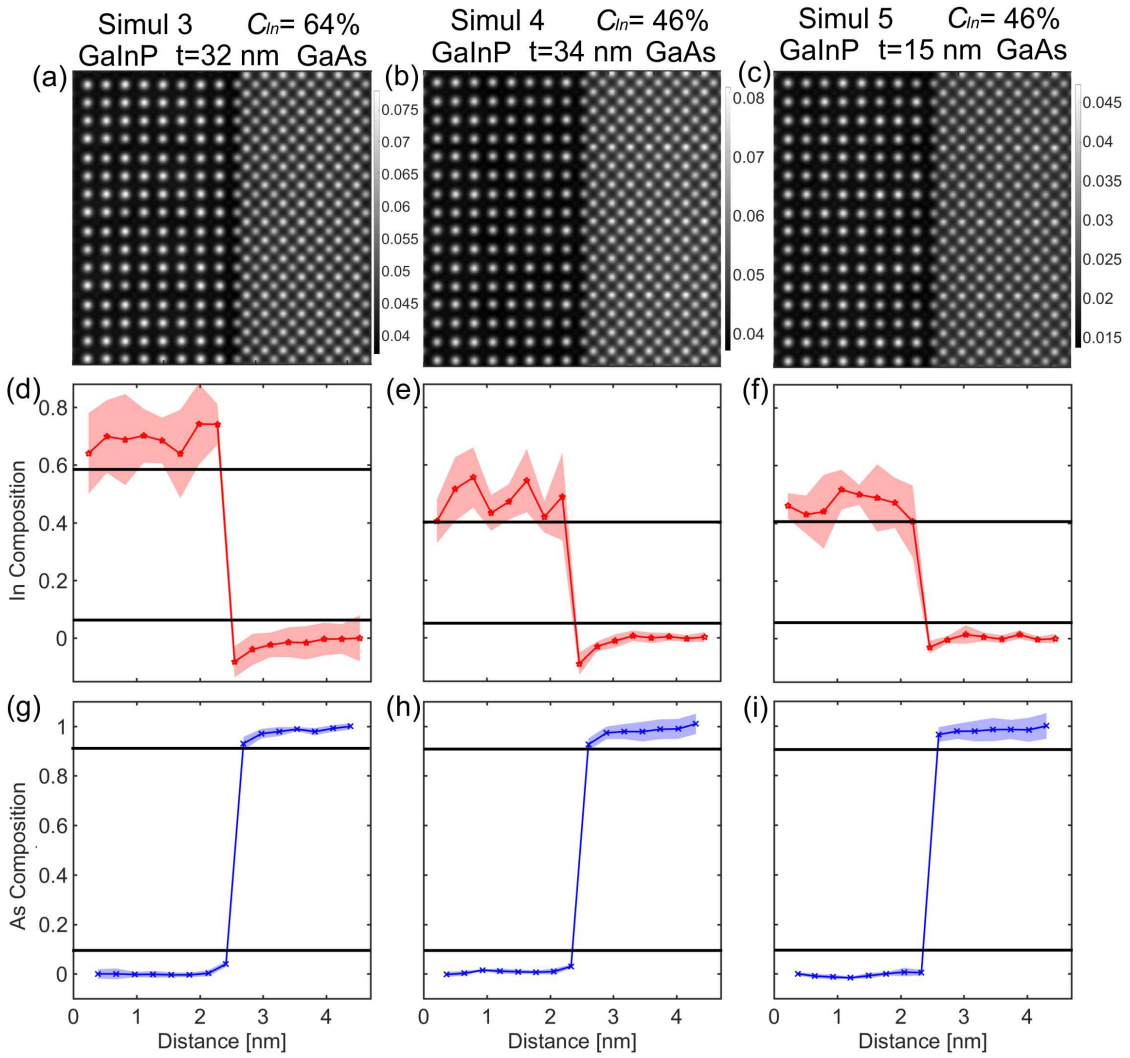

Figure 6.10: Simulated images of (Ga,In)P/GaAs abrupt interfaces with a thickness of (a) 32 nm, (b) 34 nm and (c)15 nm, respectively. The corresponding In concentration is also marked on top of the image. The profiles of the average In and As composition of each (001) atomic plane along the growth direction are shown in (d)-(f) and (g)-(i), respectively. The shaded areas around the profiles are the standard deviation of the intensity (composition) along the interface for each point.

On the other hand, simulated samples all have the same interface width (0 atomic layer) with the 90/10 evaluation method. Obviously, the simulated interfaces show no obvious difference and much abrupter than those of experimental samples. With the error function fitting method, which is quite accurate compared with the former, all

simulated interfaces have a larger K factor than that of the experimental ones and they show the same trend as the experimental ones. Simul 4 with 46 % indium composition has a sharper interface than that of Simul 3 with an indium composition of 64 %. With a decreased thickness, Simul 5 presents a much abrupter interface than that of Simul 4. Compared with the K factors determined in experiment, the K factors obtained from simulation present a larger difference among Simul 3, Simul 4 and Simul 5, which is caused by the non-linear dependence of K factor on the interface abruptness as mentioned in section 5.1.5. The large deviation between experiment and simulation is probably caused by the following factors. First and also the most important one, super cells containing the corresponding heterointerfaces used for simulation are generated taking into account only the strain relaxation. Thermal atomic diffusion at the interface is not included in the simulation. Considering the applied complicated growth conditions, the thermal diffusion, however, can lead to a significantly intermixing interface. Second, memory effects happened during the epitaxy growth can also make the interface more intermixing. Third, as mentioned previously, both evaluation approaches of the interface are not perfect and have their drawbacks, which can further enlarge the discrepancy between the theory and the experiment.

In conclusion, BIMS method can effectitvely correct the influences from the image background intensity, reveal the chemical sensitive interface and determine the island structure at the interface for further quantitative evaluation.

7 Summary and Outlook

This chapter summarizes the key results of the contrast simulations, as well as findings of the two quantitative evaluation methods for HAADF images, applied to two different material systems. If, on one hand, the investigated material systems, like (GaIn)As/GaAs, have similar average atomic numbers across the interface for both sublattices , the influences of background intensities from different regions on sublattice intensities can be neglected. This kind of material systems is therefore considered to have non-chemically sensitive backgrounds. If, on the other hand, atomic numbers across the interface are significantly different on one of the sublattices (e.g. (GaIn)P/GaAs), background intensities from different sides of the interface can greatly influence the sublattice intensities. Hence, this kind of material systems is thought to have chemically sensitive backgrounds. Furthermore, for (GaIn)As/GaAs material systems, Q-method is applied to investigate the influences of different growth conditions on both the composition homogeneity and the interface abruptness. With respect to the (GaIn)P/GaAs material systems, the BIMS method is introduced for evaluation of the heterointerface and island structures occurring there.

7.1 Summary

In order to understand the principles of HAADF imaging and also to implement the contrast simulations efficiently and effectively, simulations about HAADF imaging are carried out. The results clearly show that TDS can significantly influence the collected intensity at the detector. In order to include TDS during the simulation in this study, frozen phonon approach can be applied. Frozen phonon considers TDS through averaging HAADF images calculated from different atom configurations. To save computing time and resources, the influences of the number of phonon configurations on simulated image intensities are investigated. It is proven that 15 phonon configurations is enough to provide a robust result for the multi slice simulation within a reasonable computing time. In addition, intensities of group III and group V atomic columns together with background positions for GaAa, GaP, $(Ga_{0.5}In_{0.5})P$ are calculated to investigate the origin of background intensity and its influences on individual sublattice intensities.

Two quantitative evaluation methods, namely Q-method and BIMS, are introduced in this study. They have been successfully applied to characterize material systems with

both the non-chemically sensitive background and the chemically sensitive background, respectively.

With respect to the (GaIn)As/GaAs material systems with non-chemically sensitive backgrounds, Q-method is applied. To obtain trustable results, a 2-dimensional thickness gradient correction is performed, and the influences of factors (such as cross talk, strain relaxation, projection effect), which can significantly affect the characterization, are also discussed. To make fair comparisons between different samples, two criteria to determine the interface abruptness, namely 90/10 evaluation approach and error function fitting approach, are given and applied for all the samples investigated in the current study. In addition, the chemical homogeneity of the QW is also introduced as a characteristic for evaluation. Followed by the introduction of these fundamental properties, the influences of growth conditions, like growth temperature, growth interruption temperature and time, on the chemical composition and on the interface abruptness are investigated.

For samples with the same growth and growth interruption temperature, it can be stated that the growth temperature of (GaIn)As can strikingly influence the indium distribution at both the QW and the interface. Growth at 625 °C leads to an inhomogeneous indium distribution at the QW as well as an intermixed interface. Meanwhile, the application of growth interruptions can significantly homogenize the indium distribution at both the QW and the interface. Through the comparison with simulations, the bottom interfaces of (GaIn)As grown on GaAs are shown to be abrupt. Therefore, for samples with different growth and growth interruption temperatures, only the top interfaces of (GaIn)As are investigated. Besides the above mentioned results, it can be concluded that an abrupt interface, generated at low temperature (525 °C), can be easily degenerated into an intermixing interface with a high interruption temperature of 625 °C. Similarly, an intermixed interface, formed at 625 °C, can also be improved by growth interruption at 525 °C.

With respect to the (GaIn)P/GaAs material systems with chemically sensitive backgrounds, the above mentioned method can not be applied any more. As a result, BIMS, based on Q-method, is developed. The image background intensity and its influences on quantitative evaluation of the chemical composition are presented. It is found that the chemical composition characterization across the interface is impossible, if the image background intensity is not subtracted from the original image. With this method, the atomic resolution after background intensity subtraction can be kept for further evaluation. As expected, composition depth profiles and interface morphology strongly depend on the growth conditions. A reduction of the growth temperature from 625 °C to 525 °C can lead to a more abrupt heterointerface. The introduction of a GaP interlayer can improve the interface morphology. Nonetheless, this interlayer also results in an increased separation between the constituent QW and the barrier. With this method, the existence of an island-like structure at the interface can be shown and analyzed quantitatively.

7.2 Outlook

In the current study, the determination of the chemical composition map is based on a linear assumption between the collected intensity of the atomic column and its chemical concentration. Although the quantitative evaluation of the interface morphology and chemical homogeneity of the QW is hardly influenced by the assumption, it is still of great importance to derive the exact chemical composition of each atomic column, especially at the interface, in order to better control the lattice constant and the band gap. To aid these processes, a massive number of simulations of (GaIn)As super cells with different indium compositions needs to be carried out. Then a five-dimensional database can be created, which is composed of x, y, z space dimensions, one compositional dimension as well as one dimension of the collection angle covering both high and low angle ranges. Based on the database, the relationship between the sublattice intensity and the corresponding chemical composition can be derived and applied for the calculation of the chemical composition of individual atomic columns with great accuracy. In this study, only electron signals from high angles are made use of to carry out the quantitative evaluation. With the database, electrons scattered at low angles can also be used for the analysis.

It is found that the image background intensity can significantly influence the quantitative evaluation of chemical composition maps. In fact, the image background intensity can also be used to determine the local sample thickness and the chemical composition of corresponding atomic columns, since it depends on both the thickness and the average atomic number of the crystal. Therefore, the calculated background intensity map in this study can be converted into a thickness map or a chemical composition map. To fulfill the purpose, background intensities of experimental images needs to be compared with those of the five-dimensional database. Then, a thickness map or a chemical composition map can be derived.

8 Zusammenfassung und Ausblick

In diesem Kapitel werden die wichtigsten Ergebnisse der Kontrastsimulation sowie die beiden quantitativen Auswertungsmethoden von HAADF-Bildern, die auf zwei verschiedene Materialsysteme angewendet werden, zusammengefasst. Wenn einerseits die untersuchten Materialsysteme wie (GaIn)As/GaAs für beide Untergitter über die Grenzfläche ähnliche mittlere Atomzahlen aufweisen, können die Einflüsse von Hintergrundintensitäten aus verschiedenen Regionen auf Untergitterintensitäten ignoriert werden. Für diese Art von Materialsystem wird daher die Hintergrundintensität nicht von der chemischen Komposition beeinflusst. Wenn andererseits die Atomzahlen über die Grenzfläche signifikant unterschiedlich sind (z.B. (GaIn)P/GaAs), können Hintergrundintensitäten von verschiedenen Seiten der Grenzfläche die Untergitterintensitäten stark beeinflussen. Für diese Art von Materialsystem wird der Hintergründe von die Komposition beeinflusst. Für (GaIn)As/GaAs-Materialsysteme wird eine Q-Methode angewendet, um die Einflüsse unterschiedlicher Wachstumsbedingungen sowohl auf die chemische Homogenität als auch auf Rauigkeit der Grenzflächen zu untersuchen. In Bezug auf die (GaIn)P/GaAs-Materialsysteme wird BIMS zur Auswertung der Heterointerface- und Inselstrukturen an der Grenzfläche eingeführt.

8.1 Zusammenfassung

Um die Prinzipien der HAADF-Bildgebung zu verstehen und um die Kontrastsimulationen effizient und effektiv umzusetzen, werden Simulationen der HAADF-Bildgebung durchgeführt. Die Ergebnisse zeigen deutlich, dass TDS die gesammelte Intensität am Detektor signifikant beeinflussen kann. Um TDS während der Simulation in diese Studie einzubeziehen, kann die ”frozen-phonon” Methode angewendet werden. Dieses Modell betrachtet TDS durch Mittelung der HAADF-Bilder, die aus verschiedenen Atomkonfigurationen berechnet wurden. Um Rechenzeit und Ressourcen zu sparen, werden die Einflüsse der Anzahl der Phonon-konfigurationen auf simulierte Bildintensitäten untersucht. Es wird gezeigt, dass 15 Phonon-Konfigurationen ausreichen, um ein robustes Ergebnis für die ”multi-slice” Simulation innerhalb einer vernünftigen Rechenzeit zu liefern. Darüber hinaus werden die Intensitäten der Atomsäulen der Gruppe III und der Gruppe V zusammen mit den Hintergrundpositionen für GaAa, GaP, $(Ga_{0,5}In_{0,5})P$ berechnet, um den Ursprung der Hintergrundintensität und ihre Einflüsse auf einzelne Untergitterintensitäten zu untersuchen.

In dieser Studie werden zwei quantitative Auswertungsmethoden, nämlich Q-Methode und BIMS, eingeführt. Sie werden erfolgreich angewendet, um Materialsysteme sowohl mit dem nicht chemisch sensitiven Hintergrund als auch mit dem chemisch sensitiven Hintergrund zu charakterisieren.

In Bezug auf die (GaIn)As/GaAs-Materialsysteme mit nicht von der Komposition abhängige Hintergründen wird die Q-Methode angewendet. Um vernünftige Ergebnisse zu erzielen, wird eine zweidimensionale Dickengradientenkorrektur durchgeführt und die Einflüsse der Faktoren (wie "cross talk", Spannungsrelaxation, Projektionseffekt), die die Charakterisierung erheblich beeinträchtigen können, werden ebenfalls diskutiert. Um einen fairen Vergleich zwischen verschiedenen Stichproben herzustellen, werden zwei Kriterien zur Bestimmung der Rauigkeit der Grenzflächen, nämlich die 90/10-Auswertungs-Methode und Fehlerfunktion Fit Methode, für alle in der aktuellen Studie untersuchten Proben angewendet. Darüber hinaus wird die chemische Homogenität des QW als Merkmal für die Auswertung eingeführt. Gefolgt von der Einführung dieser fundamentalen Eigenschaften werden die Einflüsse von Wachstumsbedingungen wie Wachstumstemperatur, Wachstumsunterbrechungstemperatur und -zeit auf die chemische Zusammensetzung und auf die Grenzflächenablauf untersucht.

Bei Proben mit der gleichen Wachstums- und Wachstumsunterbrechungstemperatur, kann festgestellt werden, dass die Wachstumstemperatur von (GaIn)As die Indium-Verteilung sowohl im QW als auch an der Grenzfläche auffallend beeinflussen kann. Das Wachstum bei 625 °C führt zu einer inhomogenen Indium-Verteilung im QW sowie einer vermischten Grenzfläche. Die Anwendung der Wachstumsunterbrechungen kann die Indium-Verteilung sowohl im QW als auch an der Grenzfläche signifikant homogenisieren. Durch den Vergleich mit Simulationen wird gezeigt, dass die unteren Grenzflächen von (GaIn)As auf GaAs abrupt sind. Daher werden bei Proben mit unterschiedlichen Wachstums- und Wachstumsunterbrechungstemperaturen nur die oberen Grenzflächen von (GaIn)As untersucht. Neben den oben erwähnten Ergebnissen kann man darauf schlieSSen, dass eine abrupte Grenzfläche, die bei niedriger Temperatur (525 °C) erzeugt wird, mit einer hohen Unterbrechungstemperatur von 625 °C leicht zu einer vermischten Grenzfläche wird. Ähnlich kann eine vermischte Grenzfläche, die bei 625 °C gebildet wird, auch durch Wachstumsunterbrechung bei 525 °C verbessert werden.

In Bezug auf die (GaIn)P/GaAs-Materialsysteme mit Komposition abhängige Hintergründen kann das erwähnte Verfahren nicht mehr angewendet werden. Daher wird BIMS, basierend auf Q-Methode, entwickelt. Die Bildhintergrundintensität und ihre Einflüsse auf die quantitative Auswertung des chemischen Komposition werden eingeführt. Es wird festgestellt, dass die Bestimmung der chemischen Komposition über die Grenzfläche unmöglich ist, wenn die Bildhintergrundintensität nicht von dem Originalbild subtrahiert wird. Mit dieser Methode kann die atomare Auflösung nach der Hintergrundintensitäts-Subtraktion zur weiteren Auswertung beibehalten werden. Wie erwartet, hängen Kompositionstiefenprofile und Grenzflächenmorphologie stark von den Wachstumsbedingun-

gen ab. Eine Verringerung der Wachstumstemperatur von 625 °C auf 525 °C kann zu eine abrupten Heterogrenzfläche führen. Die Einführung einer GaP-Zwischenschicht kann die Grenzflächenmorphologie verbessern. Trotzdem führt diese Zwischenschicht auch zu einer erhöhten Trennung zwischen dem konstituierenden QW und der Barriere. Mit dieser Methode kann die Existenz einer inselförmigen Struktur an der Grenzflächen gezeigt und quantitativ analysiert werden.

8.2 Ausblick

In der aktuellen Studie basiert die Bestimmung der chemischen Kompositions auf der Annahme dass zwischen der integrierten Intensität der Atomsäulen und ihrer chemischen Komposition eine linear Beziehung besteht. Obwohl die quantitative Auswertung der Grenzflächenmorphologie und der chemischen Homogenität des QW kaum von dieser Annahme beeinflusst wird, ist es immer noch sehr wichtig, die genaue chemische Komposition jeder Atomsäule, insbesondere an der Grenzfläche, abzuleiten, um die Gitterkonstante und die Bandlücke besser kontrollieren zu können. Um dies zu unterstützen, muss eine große Anzahl von Simulationen von (GaIn)As-Superzellen mit unterschiedlichen Indium Gehalt durchgeführt werden. Dann kann eine fünfdimensionale Datenbank erstellt werden, die aus den Raumdimensionen x, y, z, der Komposition Dimension sowie der Dimension des Detektorwinkels besteht, die sowohl hohe als auch niedrige Winkelbereiche abdeckt. Basierend auf der Datenbank kann die Beziehung zwischen der Untergitterintensität und der entsprechenden chemischen Komposition abgeleitet und für die Berechnung der chemischen Komposition einzelner Atomsäule mit groSSer Genauigkeit angewendet werden. In dieser Studie werden nur Elektronensignale unter hohen Winkeln verwendet, um die quantitative Auswertung durchzuführen. Mit der Datenbank können auch Elektronen, die in niedrige Winkeln gestreut werden, für die Analyse verwendet werden.

Es wird festgestellt, dass die Bildhintergrundintensität die quantitative Bewertung der chemischen Kompositions signifikant beeinflussen kann. Tatsächlich kann die Bildhintergrundintensität auch verwendet werden, um die lokale Probendicke und die chemische Komposition der entsprechenden Atomsäulen zu bestimmen, da sie sowohl von der Dicke als auch von der durchschnittlichen Atomzahl des Kristalls abhängt. Daher kann die berechnete Hintergrundintensitätskarte in dieser Studie in eine Dickenkarte oder eine Kompositionskarte umgewandelt werden. Um dies zu erreichen, müssen Hintergrundintensitäten der experimentellen Bilder mit denen der fünfdimensionalen Datenbank verglichen werden. Dann kann eine Dickenkarte oder eine Kompositionskarte abgeleitet werden.

References

[1] J. Kilby, *Miniaturized electronic circuits*, US 3138743, (filed Feb 1959), 1964.

[2] R. Noyce, *Semiconductor device-and-lead structure*, US 2981877, (filed Jul 1959), 1961.

[3] 'The Nobel Prize in physics 2014', *Nobel Media AB 2014. Web.19*, 2016.

[4] H. Kroemer, 'Quasi-electric fields and band offsets: Teaching electrons new tricks', *Nobel Lecture*, 2000.

[5] O. Schuler, O. Dehaese, X. Wallart, and F. Mollot, 'A study of gainp/gaas interfaces: Metallurgical coupling of successive quantum wells', *Superlattices and Microstructures*, vol. 23, no. 2, 1998.

[6] S. Dhellemmes, S. godey, A. Wilk, X. Wallart, and F. Mollot, *J. Cryst. Growth 278, 564*, 2005.

[7] K. Uchida, K. Satoh, K. Asano, A. Koizumi, and S. Nozaki, *J. Cryst. Growth 370, 136*, 2013.

[8] Y. Fujiwara, Y. Nonogaki, R. Oga, A. Koizumi, and Y. Takeda, *Appl. Surf. Sci.*, vol. 216, no. 564, 2003.

[9] A. Lankinen, L. Knuuttila, P. Kostamo, T. Tuomi, H. Lipsanen, P. Mcnally, and L. OReilly, *J. Cryst. Growth 311, 4619*, 2009.

[10] O. Dwhaese, X. Wallart, O. Schuler, and F. Mollot, *Appl. Surf. Sci. 123-124, 523*, 1998.

[11] M. Lopez-Escalante, M. Gabas, I. Garcia, E. Barrigon, I. Rey-Stolle, C. Algora, S.Palanco, and J. Ramos-Barrado, *Appl. Surf. Sci.360, 477*, 2016.

[12] S. Müller, J. Weyher, R. Dian, and W. Jantz, 'Progress in the layer thickness determination of algaas/gaas heterostructures using selective etching and afm imaging of the (110) cleavage planes', *Materials Science and Engineering: B*, vol. 44, no. 1, pp. 96 –100, 1997.

[13] X. Wang, Z. Niu, S. Feng, and Z. Miao, '1.35m photoluminescence from in0.5ga0.5as/gaas islands grown by molecular beam epitaxy via cycled (inas)1/(gaas)1 monolayer deposition', *Journal of Crystal Growth*, vol. 220, no. 1, pp. 16 –22, 2000.

[14] S. Thoma and H. Cerva, 'New methods for qualitative and quantitative analysis of the gaas/algaas interface by high-resolution electron microscopy', *Ultramicroscopy*, vol. 38, pp. 265–289, 1991.

[15] Y. Wang, Z. Wang, T. Brown, A. Brown, and G. May, *Thin Solid Films*, vol. 397, no. 162, 2001.

[16] J. Seo and X.-L. Wang, *J. Cryst Growth*, vol. 324, no. 73, 2011.

[17] G. Kothleitner, M. Neish, N. Lugg, S. Findlay, W. Grogger, F. Hofer, and L. Allen, 'Quantitative elemental mapping at atomic resolution using x-ray spectroscopy', *Phys. Rev. Lett.*, vol. 112, no. 085501, 2014.

[18] K. Leifer, P. Buffat, P. Stadelmann, and E. Kapon, 'Theoretical and experimental limits of the analysis of iii/v semiconductors using eels', *Micro*, vol. 31, pp. 411–427, 2000.

[19] K. Kimoto, T. Asaka, T. Nagai, M. Saito, Y. Matsui, and K. Ishizuka, 'Element-selective imaging of atomic columns in a crystal using stem and eels', *Nature*, vol. 450, pp. 702–704, 2007.

[20] S. J. Pennycook and D. Jesson, 'High-resolution incoherent imaging of crystals', *Phys. Rev. Lett.*, vol. 64, no. 938, 1990.

[21] S. Pennycook and D. Jesson, 'High-resolution z-contrast imaging of crystals', *Ultramicroscopy*, vol. 37, no. 1-4, pp. 14–38, Aug. 1991.

[22] P. Nellist and S. Pennycook, *Scanning Microsc.*, vol. 11, no. 81, 1997.

[23] T. Grieb, K. Müller, R. Fritz, M. Schowalter, N. Neugebohrn, N. Knaub, K. Volz, and A. Rosenauer, 'Determination of the chemical composition of ganas using stem haadf imaging and stem strain state analysis.', *Ultramicroscopy*, vol. 117, pp. 15–23, 2012.

[24] S. V. Aert, J. Verbeeck, R. Erni, S. Bals, M. Luysberg, D. V. Dyck, and G. V. Tendeloo, 'Quantitative atomic resolution mapping using high-angle annular dark field scanning transmission electron microscopy.', *Ultramicroscopy*, vol. 109, pp. 1236–1244, 2009.

[25] A. Rosenauer, T. Mehrtens, K. Müller, K. Gries, M. Schowalter, V. Satyam, S. Bley, C. Tessarek, D. Hommel, K. Sebald, M. Seyfried, J. Gutowski, A. Avramescu, K. Engl, and S. Lutgen, 'Composition mapping in ingan by scanning transmission electron microscopy.', *Ultramicroscopy*, vol. 111, pp. 1316–1327, 2011.

[26] G. Martinez, A. Rosenauer, A. D. Backer, J. Verbeeck, and S. V. Aert, 'Quantitative composition determination at the atomic level using model-based high-angle annular dark field scanning transmission electron microscopy', *Ultramicroscopy*, vol. 137, pp. 12–19, 2014.

[27] A. Rosenauer, K. Gries, K. Müller, A. Pretorius, M. Schowalter, A. Avramescu, K. Engl, and S. Lutgen, *Ultramicroscopy*, vol. 109, no. 1171, 2009.

[28] J. Lebeau, S. Findlay, L. Allen, and S. Stemmer, *Phys. Rev. Lett.*, vol. 100, no. 206101, 2008.

[29] H. Han, A. Beyer, K. Jandieri, K. Gries, L. Duschek, W. Stolz, and K. Volz, 'Quantitative characterization of the interface roughness of (GaIn) As quantum wells by high resolution STEM', *Micron*, vol. 79, pp. 1–7, 2015.

[30] D. O. Klenov and S. Stemmer, 'Contributions to the contrast in experimental high-angle annular dark-field images', *Ultramicroscopy*, vol. 106, pp. 889–901, 2006.

[31] P. D. Robb and A. J. Craven, 'Column ratio mapping : A processing technique for atomic resolution high-angle annular dark-field (HAADF) images', *Ultramicroscopy*, vol. 109, pp. 61–69, 2008.

[32] P. D. Robb, M. Finnie, P. Longo, and A. J. Craven, 'Experimental evaluation of interfaces using atomic-resolution high angle annular dark field (HAADF) imaging', *Ultramicroscopy*, vol. 114, pp. 11–19, 2012.

[33] Y. Kotaka, *Ultramicroscopy*, vol. 110, no. 555, 2010.

[34] H. Han, A. Beyer, J. Belz, A. König, W. Stolz, K. Volz, W. Stolz, and K. Volz, 'Quantitative atomic resolution at interfaces : Subtraction of the background in STEM images with the example of (Ga , In) P / GaAs structures Quantitative atomic resolution at interfaces : Subtraction of the background in STEM images with the example of (Ga , In) P / GaAs structures', vol. 025301, 2017.

[35] G. Gottstein, *Physical Foundations of Materials Science*. Springer-Verlag Berlin Heidelberg GmbH, 2004.

[36] S. H. Simon, *Oxford Solid State Basics*, 114. Oxford, 2013.

[37] R. Gross and A. Marx, *Festkörperphysik*. De Gruyter, 2014, vol. ch. 1.1.1.1.

[38] . [Online]. Available: `URL : http : / / learn . crystallography . org . uk / learn - crystallography/what-is-a-crystal/ . Accessed16.08.2016`.

[39] D. Williams and C. Carter, *Transmission Electron Microscopy*, 2st. Springer, 2009.

[40] E. Rutherford, 'The scattering of and particles by matter and the structure of the atom', *Phil. Mag.*, vol. 21, pp. 669–688, 1911.

[41] N. Knaub, 'Structural analysis of dilute bismide alloys by means of high resolution scanning transmission electron microscopy', PhD thesis, 2016.

[42] J. Spence, *High-Resolution Transmission Electron Microscopy, third ed.* Oxford University Press, 2003.

[43] L. Allen, S. Findlay, M. Oxley, and C. Rossouw, *Ultramicroscopy*, vol. 96, no. 47, 2003.

[44] C. Dwyer and J. Etheridge, *Ultramicroscopy*, vol. 96, no. 343, 2003.

[45] J. Goldstein, J. Costley, G. Lorimer, and S. Reed, *SEM*, no. 315, 1977.

[46] R. F. Ã. Egerton, 'Limits to the spatial , energy and momentum resolution of electron energy-loss spectroscopy', vol. 107, pp. 575–586, 2007.

[47] J. Spence, *Experimental High-Resolution Electron Microscopy*. OUP, New York, 1988.

[48] R. Glaisher, A. Spargo, and D. Smith, 'A systematic analysis of hrem imaging of elemental semiconductors', *Ultramicroscopy*, vol. 27, pp. 35–52, 1989.

[49] L. Rayleigh, 'On the theory of optical images with special reference to the microscope', *Phil. Mag.*, vol. 42, pp. 167–195, 1896.

[50] P. D. Nellist, *The Principles and Interpretation of Annular Dark-Field Z-Contrast Imaging*. 2008, vol. 113, pp. 147–203, ISBN: 0120147556.

[51] G. Tatlock, 'Aberration-Corrected Analytical Transmission Electron Microscopy', in, R. Brydson, Ed. Wiley, 2011, ch. 2 - Introduction to Electron optics, pp. 21–38.

[52] T. Wegele, 'Microstructural characterization of dilute n-containing semiconductor alloys and heterostructures by scanning transmission electron microscopy', PhD thesis, Philipps-Universität Marburg, 2016.

[53] A. Bleloch and Q. Ramasse, 'Aberration-Corrected Analytical Transmission Electron Microscopy', in, R. Brydson, Ed. Wiley, 2011, ch. 4 - Lens Aberrations: Diagnosis and Correction, pp. 55–89.

[54] H. Ibach and H. Lüth, *Solid State Physics: An Introduction to Principles of Materials Science*. Springer, 2009.

[55] P. Hofmann, *Solid State Physics: An Introduction*. WILEY-VCH, 2002.

[56] R. Loudon, *The Quantum Theory of Light, Third Edition*. University Press Oxford, 2000.

[57] M. Scully and M. Zubairy, *Quantum Optics*. University Press, Cambridge, 1997.

[58] A. Ott, 'Structural characterization of antimonide-based metamorphic buffer layers on (001) silicon substrate', PhD thesis, Philipps- Universität Marburg, 2016.

[59] S. Mokkapati and C. Jagadish, 'III-V compound SC for optoelectronic devices', *Materials Today*, vol. 12, no. 4, pp. 22–32, 2009.

[60] L. Vegard, 'Die konstitution der mischkristalle und die raumfüllung der atome', *Zeitschrift für Physik*, vol. 5, pp. 17–26, 1921.

[61] S. Adachi, 'Gaas, alas, and alxga1xas: Material parameters for use in research and device applications', *Journal of Applied Physics*, vol. 58, 1985.

[62] L. Wilson, D. Mowbray, M. Skolnick, D. Peggs, G. Rees, J. David, R. Grey, G. Hill, and M. Pate, 'Electrical and optical bistability in [111] gainasgaas piezo-electric quantum wells', *Superlattices and Microstructures*, vol. 21, no. 1, pp. 113 –118, 1997.

[63] N Nishiyama, M Arai, S Shinada, T Miyamoto, F Koyama, and K Iga, 'Growth and optical properties of highly strained gainas/gaas quantum wells on (311)b gaas by mocvd', *Journal of Crystal Growth*, vol. 221, no. 1, pp. 530 –534, 2000, Proc Tenth Int Conf Metalorganic Vapor Phase Epitaxy.

[64] D Schlenker, T Miyamoto, Z. Chen, M Kawaguchi, T Kondo, E Gouardes, F Koyama, and K Iga, 'Critical layer thickness of 1.2-m highly strained gainas/gaas quantum wells', *Journal of Crystal Growth*, vol. 221, no. 1, pp. 503 –508, 2000, Proc Tenth Int Conf Metalorganic Vapor Phase Epitaxy.

[65] T. Pearsall and J. Hirtz, *J. Cryst. Growth*, vol. 54, pp. 127–131, 1981.

[66] S. Wu, Z. Huang, Y. Liu, Q. Huang, W. Guo, and Y. Cao, 'The effects of indium segregation on the valence band structure and optical gain of gainas/gaas quantum wells', *Physica E: Low-dimensional Systems and Nanostructures*, vol. 41, no. 9, pp. 1656 –1660, 2009.

[67] K. Yamaguchi, T. Okada, and F. Hiwatashi, 'Analysis of indium surface segregation in molecular beam epitaxy of InGaAs / GaAs quantum wells', vol. 18, pp. 700–704, 1997.

[68] S Martini, J. E. Manzoli, and A. A. Quivy, 'Study of the influence of indium segregation on the optical properties of InGaAs/GaAs quantum wells via split-operator method', pp. 277–283, 2010.

[69] T. Kitatani, Y. Yazawa, S. Watahiki, K. Tamura, J. Minemura, and T. Warabisako, 'Optimal growth procedure of gainp/gaas heterostructure for high-efficiency solar cells', *Solar Energy Materials and Solar Cells*, vol. 50, pp. 221–227, 1998.

[70] M. di Forte-Poisson, S. Bernard, L. Teisseire, C. Brylinski, S. Cassette, and J. di Persio, 'Low tensile strain gainas:uid/gaas:c superlattice heterostructures grown by lp mocvd: Application to gainp/gaas heterojunction bipolar transistor base layer', *Journal of Crystal Growth*, vol. 221, pp. 717 –721, 2000.

[71] A. Moto, S. Tanaka, T. Tanabe, and S. Takagishi, 'Gainp/gaas and mechanically stacked gainas solar cells grown by mocvd using tbas and tbp as v-precursors', *Solar Energy Materials and Solar Cells*, vol. 66, pp. 585 –592, 2001.

[72] J. Olson, R. Ahrenkiel, D. Dunlavy, B. Keyes, and A. Kibbler, *Appl. Phys. Lett.*, vol. 55, no. 1208, 1989.

[73] H. Kamei and H. hayashi, *J. Cryst. Growth*, vol. 107, no. 567, 1991.

[74] A. Clawson, T. Vu, S. Pappert, and C. Hanson, *J. Cryst. Growth*, vol. 124, no. 536, 1992.

[75] J. Wittgreffe, M. Yates, S. Perrin, and P. Spurdens, *J. Cryst. Growth*, vol. 130, no. 51, 1993.

[76] T. Anan, S. Sugou, K. Nishi, and T. Ichihashi, *Appl. Phys. Lett.*, vol. 63, no. 1047, 1993.

[77] K. Werner, 'Chemical vapor deposition and physical characterization of gallium and carbon- related structures on si (001) and gap/si templates for the growth of graphene layers', PhD thesis, Philipps-Universität Marburg, 2015.

[78] G. Stringfellow, *Organometallic vapor-phase epitaxy: theory and practice*. Academic Press, 2 edition, 1998.

[79] P. Ludewig, 'Growth and characterization of dilute bismide gaas based alloys for high efficiency infra red laser diodes', PhD thesis, Philipps-Universität Marburg, 2014.

[80] C. Hutchinson, R. Hackenberg, and G. Shiflet, 'A comparison of eds microanalysis in fib-prepared and electropolished tem thin foils', *Ultramicroscopy*, vol. 94, no. 1, pp. 37 –48, 2003.

[81] P. Voyles, J. Grazul, and D. Muller, 'Imaging individual atoms inside crystals with adf-stem', *Ultramicroscopy*, vol. 96, no. 34, pp. 251 –273, 2003, Proceedings of the International Workshop on Strategies and Advances in Atomic Level Spectroscopy and Analysis.

[82] L. Dieterle, B. Butz, and E. Müller, 'Optimized ar+ -ion milling procedure for tem cross-section sample preparation', *Ultramicroscopy*, vol. 111, pp. 1636–1644, 2011.

[83] J. T. Armstrong, P. Mcswiggen, and C. Nielsen, 'A thermal field-emission electron probe microanalyzer for improved analytical spatial resolution', vol. 3, no. 17, pp. 17–20, 2013.

[84] P. Nellist, 'The Principles of STEM Imaging', no. i, pp. 91–116, 2011.

[85] J. Cowley, 'Image contrast in a transmission scanning electron microscope', *Appl. Phys. Lett*, vol. 15, pp. 58–59, 1969.

[86] A. Graven, 'Aberration-Corrected Analytical Transmission Electron Microscopy', in, R. Brydson, Ed. Wiley, 2011, ch. 6 - Details of STEM, pp. 111–162.

[87] R. Egerton, 'Electron energy-loss spectroscopy in the TEM', vol. 72, 2009.

[88] P. Hartel, H. Rose, and C. Dinges, 'Conditions and reasons for incoherent imaging in stem', *Ultramicroscopy*, 1996.

[89] L. Jones, H. Yang, T. J. Pennycook, M. S. J. Marshall, S. Van Aert, N. D. Browning, M. Castell, and P. D. Nellist, 'Smart Aligna new tool for robust non-rigid registration of scanning microscope data', *Advanced Structural and Chemical Imaging*, vol. 1, p. 1, 2015.

[90] D. He and Z. Li, 'A practical approach to quantify the adf detector in stem', *J. Phys.: Conf. Ser.*, vol. 522, p. 012 017, 2014.

[91] J. Lebeau and S. Stemmer, *Ultramicroscopy*, vol. 108, p. 1653, 2008.

[92] J. Cowley and A. Moodie, 'The scattering of electrons by atoms and crystals. i, a new theoretical approach.', *Acta Cryst.*, vol. 10, pp. 609–619, 1957.

[93] P. Goodman and A. Moodie, 'Numerical evaluation of n-beam wave functions in electron scattering by the multislice method', *Acta Cryst.*, vol. A30, pp. 280–290, 1974.

[94] K. Ishizuka and N. Uyeda, 'A new theoretical and practical approach to the multislice method', *Acta Cryst.*, vol. A33, pp. 740–749, 1977.

[95] J. O. Oelerich, L. Duschek, J. Belz, A. Beyer, S. D. Baranovskii, and K. Volz, 'Ultramicroscopy STEMsalabim : A high-performance computing cluster friendly code for scanning transmission electron microscopy image simulations of thin specimens', *Ultramicroscopy*, vol. 177, pp. 91–96, 2017.

[96] E. J. Kirkland, *Advanced Computing in Electron Microscopy*. Springer, 2010.

[97] C. Fanidis, D. V. Dyck, and J. V. Landuyt, 'Inelastic scattering of high-energy electrons in a crystal in thermal equilibrium with the environment, i. theoretical framework', *Ultramicroscoopy*, vol. 41, pp. 55–64, 1992.

[98] C. Fanidis, D. V. Dyck, and J. V. Landuyt, 'Inelastic scattering of high-energy electrons in a crystal in thermal equilibrium with the environment, ii. solution of the equations and applicatioins to concrete cases', *Ultramicroscoopy*, vol. 48, pp. 133–164, 1993.

[99] P. Hirsch, A. Howie, R. Nicholson, D. Pashley, and M. Whelan, *Electron microscopy of thin crystals*. Krieger Publishing Co, New York, 1977.

[100] R. Loane, P. Xu, and J. Silcox, 'Thermal vibratioins in convergent-beam electron diffraction', *Acta Crystallogr.*, vol. 47, pp. 267–278, 1991.

[101] D. Muller, B. Edwards, E. Kirkland, and J. Silcox, 'Detailed calculations of thermal diffuse scattering', *Microsc. Microanal.*, vol. 3, pp. 1153–1154, 1997.

[102] Z. Wang, 'The frozen lattice a roach for incoherent phonon excitations in electron scattering, how accurate is it?', *Acta Crystallogr.*, vol. 54, pp. 468–480, 1998.

[103] Z. L. Wang, 'Thermal diffuse scattering in sub-angstrom quantitative electron microscopyphenomenon, effects and approaches', *Micron*, vol. 34, no. 3, pp. 141 –155, 2003, Zeitler Festschrift.

[104] A. Beyer, L. Duschek, J. Belz, J. O. Oelerich, K. Jandieri, and K. Volz, 'Influence of surface relaxation of strained layers on atomic resolution adf imaging', *Ultramicroscopy*, vol. 181, pp. 8–16, 2017, ISSN: 0304-3991.

[105] F. Lelarge, O. Dehaese, E. Kapon, and C. Priester, 'Strain relaxation at cleaved surfaces studied by atomic force microscopy', *Appl. Phys. A Mater. Sci. Process.*, vol. 69, pp. 347–351, 1999.

[106] F. Lelarge, C. Priester, C. Constantin, A. Rudra, K. Leifer, and E. Kapon, 'Strain mapping of v-groove ingaas/gaas strained quantum wires using cross-sectional atomic force microscopy', *Appl. Surf. Sci.*, vol. 166, pp. 290–294, 2000.

[107] J. Belz, A. Beyer, T. Torunski, W. Stolz, and K. Volz, 'Direct investigation of (sub-) surface preparation artifacts in gaas based materials by fib sectioning', *Ultramicroscopy*, vol. 163, pp. 19 –30, 2016, ISSN: 0304-3991.

[108] A. Rosenauer and M. Schowalter, 'Stemsim-a new software tool for simulation of stem haadf z-contrast imaging, in: Microscopy of semiconducting materials 2007', *Springer*, 2007.

[109] T. Grieb, K. Müller, R. Fritz, V. Grillo, M. Schowalter, K. Volz, and A. Rosenauer, 'Quantitative chemical evaluation of dilute ganas using adf stem: Avoiding surface strain induced artifacts', *Ultramicroscopy*, vol. 129, pp. 1 –9, 2013.

[110] A. beyer, R. Straubinger, J. Belz, and K. Volz, 'Local sample thickness determination via scanning transmission electron microscopy defocus series', *Journal of Microscopy*, vol. 262, no. 2, pp. 171–177, 2016.

[111] P. Galindo, J. Pizarro, S. Molinal, and K. Ishizuka, 'High resolution peak measurement and strain mapping using peak pairs analysis', *Microscopy and Analysis*, pp. 23–25, 2009.

[112] R. Peizel, L. Zepeda-Ruiz, W. Weinberg, and D. Maroudas, 'Effects of buffer layer thickness and film compositional grading on strain relaxation kinetics in inas/gaas(111)a heteroepitaxy', vol. 463, pp. 634–640, 2000.

[113] D. Dunstan, 'Strain and strain relaxation in semiconductors', *J. Mat. Sci.: Materials in Electronics*, vol. 8, pp. 337–375, 1997.

[114] S. Maccagnano-Zacher, K. Mkhoyan, E. Kirkland, and J. Silcox, 'Effects of tilt on high-resolution adf-stem imaging', *Ultramicroscopy*, vol. 108, no. 8, pp. 718 –726, 2008.

[115] J. Griffiths, F. Oehler, F. Tang, S. Zhang, W. Fu, T. Zhu, S. Findlay, C. Zheng, J. Etheridge, T. L. Martin, P. Bagot, M. Moody, D. Sutherland, P. Dawson, M. Kappers, C. Humphreys, and R. Oliver, *J. Appl. Phy.*, vol. 119, p. 175 703, 2016.

[116] F. Aurenhammer, *ACM Comput. Surv*, vol. 23, p. 345, 1991.

Acknowledgement

In the end I would like to make use of the opportunity to express my deep appreciation to the following people. Without your help and support this thesis could never be finished.

First I would like to express my great gratitude to my advisor Prof. Kerstin Volz for accepting me as a Ph.D. student in this group. During the past four years, her interesting conversations, her warmly discussions and the questions incented me to widen my research from various perspectives. I would also like to present my sincere thanks to Prof. Wolfgang Stolz for the encouragement and support on my way to scientic research.

I would also like to give my sincere thank to Prof. Martin Koch for his kindness to be the second referee of my doctoral thesis. I also want to deeply thank Prof. Heinz Jänsch and PD Dr. Ralf Tonner to be a member of the board of examiners.

I also want to thank Dr. Andreas Beyer for supervising my work, teaching me both experimental and progamming skills, as well as the creative and helpful ideas.

I would also like to thank Dr. Katharina Gries, Dr. Jan Oliver Oelerich, Dr. Kakhaber Jandieri, Jürgen Belz, Lennart Duschek, Rocio Felix, Andrea Ott, Pirmin Kükelhan, Shalini Gupta, Rainer Straubinger, Nikolei Knaub, Tatjana Wegele, Dominic Duffy for their kind support and help in both studies and lives. You have not only teached me how to carry out scientic research, but also brought a lot of fun to my life.

I also want to thank the secretaries Elke Vaupel, Marina Koch and Isabelle Kimmel for their considerate work and kindness.

Also, I would like to thank my big familiy (the whole WZMW group) for the wonderful time and memories of the summer party, the chrismas party and also the chinese party.

I am also grateful to all my chinese friends. They support and help me in my everyday life to make me better focus on my studies.

Last but not the least, I would like to thank my parents and my younger sister for their encouragement and support.

Wissenschaftlicher Werdegang

Personal Information

Date/Place of Birth **27.09.1985, Runan, China**.

Citizenship **Chinese**.

Education

09/2013–11/2017 **Philipps-Universität Marburg, Germany**, *Ph.D. in Physics*, Title: Quantitative evaluation of the interfaces in III-V semiconductors with scanning transmission electron microscopy.

10/2009–10/2012 **Rheinisch-Westfaelische Technische Hochschule Aachen, Germany**, *M.Sc. in Metallurgical Engineering*, Title: Deformation and annealing of Mg alloys with and without rare earth elements.

09/2005–06/2009 **University of Science and Technology Beijing, China**, *B.Sc. in Physics Materials*, Title: Effects of doping surfactant on magnetic properties of magnetic recording materials.

06/2005 **Runan No.1 High school, China**.

Publications and Posters

Publications

2017 **Han Han, Andreas Beyer, Jürgen Belz, Alexander König, Wolfgang Stolz, Kerstin Volz**, *Quantitative atomic resolution at interfaces: Subtraction of the background in STEM images with the example of (Ga,In)P/GaAs structures*, Journal of Applied Physics **121**, 025301.

2016 **P. Springer, S. Gies, P. Hens, C. Fuchs, H. Han, J. Hader, J.V. Moloney, W. Stolz, K. Volz, S.W. koch, W. Heimbrodt**, *Charge transfer luminescence in (GaIn)As/GaAs/Ga(NAs) double quantum well*, Journal of Luminescence **175**, 255-259.

2015 **H. Han, A. Beyer, K. Jandieri, K.I. Gries, L. Duschek, W. Stolz, K. Volz**, *Quantitative characterization of the interface roughness of (GaIn)As quantum wells by high relution STEM*, Micron **79**, 1-7.

Posters

2016 **Han Han, Andreas Beyer, Jürgen Belz, Alexander König, Wolfgang Stolz, Kerstin Volz**, *Correlation of interface morphology and composition in GaInP/GaAs with growth conditions*, The 16^{th} European Microscopy congress, Lyon, France.

2015 **Han Han, Andreas Beyer, Katharina I. Gries, Wolfgang Stolz, Kerstin Volz**, *Quantitative characterization of composition and interface roughness of (GaIn)As quantum wells*, Microscopy of Semiconducting Materials, (MSM-XIX), Cambridge, UK.

2014 **Han Han, Andreas Beyer, Katharina I. Gries, Wolfgang Stolz, Kerstin Volz**, *Characterization of the interface structure of (GaIn)As and Ga(NAs) grown on GaAs*, The 18^{th} International Microscopy Congress, Prague, Czech Republic.